https://lib.uliege.be https://matheo.uliege.be

Computational and Experimental Micromechanical Analysis of Proximal Tibia of Aging Rats

Auteur : Ska, Margaux
Promoteur(s) : Ruffoni, Davide
Faculté : Faculté des Sciences appliquées
Diplôme : Master en ingénieur civil biomédical, à finalité spécialisée
Année académique : 2023-2024
URI/URL : http://hdl.handle.net/2268.2/20870

Avertissement à l'attention des usagers :

Tous les documents placés en accès ouvert sur le site le site MatheO sont protégés par le droit d'auteur. Conformément aux principes énoncés par la "Budapest Open Access Initiative"(BOAI, 2002), l'utilisateur du site peut lire, télécharger, copier, transmettre, imprimer, chercher ou faire un lien vers le texte intégral de ces documents, les disséquer pour les indexer, s'en servir de données pour un logiciel, ou s'en servir à toute autre fin légale (ou prévue par la réglementation relative au droit d'auteur). Toute utilisation du document à des fins commerciales est strictement interdite.

Par ailleurs, l'utilisateur s'engage à respecter les droits moraux de l'auteur, principalement le droit à l'intégrité de l'oeuvre et le droit de paternité et ce dans toute utilisation que l'utilisateur entreprend. Ainsi, à titre d'exemple, lorsqu'il reproduira un document par extrait ou dans son intégralité, l'utilisateur citera de manière complète les sources telles que mentionnées ci-dessus. Toute utilisation non explicitement autorisée ci-avant (telle que par exemple, la modification du document ou son résumé) nécessite l'autorisation préalable et expresse des auteurs ou de leurs ayants droit.

COMPUTATIONAL AND EXPERIMENTAL MICROMECHANICAL ANALYSIS OF PROXIMAL TIBIA OF AGING RATS

Master thesis conducted by

Margaux SKA

with the aim of obtaining the degree of Master in Biomedical Engineering

Under the supervision of

Davide RUFFONI

Laura MÜLLER

UNIVERSITY OF LIÈGE
FACULTY OF APPLIED SCIENCES

Academic year 2023-2024

Abstract

The bone-cartilage interface plays an important biomechanical role by transmitting forces across the joint. This highly complex region undergoes notable structural and mechanical changes with aging, closely associated with the development of diseases such as osteoarthritis and incomplete growth plate fusion. Despite its significant clinical relevance, there is a lack of comprehensive data on how aging impacts the microarchitecture and biomechanical properties of subchondral bone. Consequently, studying the structure-mechanics relationship as well as the impact of aging on this one compared to the metaphyseal bone part is important.

This thesis investigates how age-related alterations in bone microstructure and stiffness influence the mechanical transfer in the proximal rat tibiae under load application. To this end, a computational study using micro-structural finite element analysis (micro-FE) was conducted alongside experimental analyses.

A first analysis of the impact of bone stiffness on bone mechanics demonstrates a clear impact on its overall mechanical behavior, though to a lesser extent in the subchondral region compared to the metaphyseal region. This variation in behavior between the two regions underscores the importance of examining specific sub-regions of the bone individually, rather than treating the bone as a homogeneous entity, to capture its different mechanical responses.

Further analysis of microstructural influence, in relation to aging, highlighted the importance of bone bridges in facilitating the transmission of mechanical forces throughout the bone, rather than forcing them to concentrate in the subchondral region when few bone bridges are present, as in young bones. Additionally, a significant degree of inter-sample variability was observed in the mechanical behavior of young bones, a phenomenon notably absent in older bones.

The impact of the presence or absence of a growth plate had a more pronounced effect on the mechanical behavior of young bones compared to older ones, given the higher amount of bone bridges connecting the subchondral to the metaphyseal regions in older samples. Simulating a pathological growth plate in young bones, characterized by a high value of Young's modulus, revealed deformation patterns that closely resembled those in old bones, suggesting that such changes might mimic age-related alterations in bone mechanics.

Although the computational analysis provided valuable insights into the redistribution of strains within the bone structure, it did not enable the assessment of failure loads. To address this limitation, experimental processes were developed to specifically determine failure loads in both old and young samples.

Overall, this study provides valuable insights into the relationship between bone microstructure and its underlying mechanical behavior as it ages, in the proximal tibia. It demonstrated how specific bone structures influence the mechanical properties in the subchondral trabecular, subchondral cortical, metaphyseal trabecular, and metaphyseal cortical bone regions, enhancing our understanding of how mechanical forces affect bone during the aging process and associated pathologies.

Résumé

L'interface os-cartilage dans les articulations joue un rôle biomécanique important en transmettant les forces à travers l'articulation. Cette région très complexe subit des changements structurels et mécaniques notables avec le vieillissement, étroitement associés au développement de maladies telles que l'arthrose et la fusion incomplète de la plaque de croissance. Malgré son importance clinique, très peu de données concernant l'impact du vieillissement sur la microarchitecture et les propriétés biomécaniques de l'os sous-chondral sont recensées. Par conséquent, il est important d'étudier la relation structure-comportement mécanique ainsi que l'impact du vieillissement sur l'os sous-chondral par rapport à d'autres sites osseux.

Cette thèse étudie comment les altérations de la microstructure osseuse liées à l'âge influencent le transfert mécanique dans le tibia proximal du rat sous l'application d'une charge. À cette fin, une étude computationnelle utilisant l'analyse micro-structurale par éléments finis (micro-FE) a été menée parallèlement à des analyses expérimentales.

L'analyse des propriétés mécaniques de l'os a démontré un impact clair sur son comportement mécanique global, bien que dans une moindre mesure dans la région sous-chondrale par rapport à la région métaphysaire. Cette variation de comportement entre les deux régions souligne l'importance d'examiner individuellement des sous-régions spécifiques de l'os, plutôt que de traiter l'os comme une entité homogène, afin de saisir ses différentes réponses mécaniques.

Une analyse plus poussée de l'influence de la microstructure, en relation avec le vieillissement, a mis en évidence l'importance des ponts osseux reliant la partie sous-chondrale à la région métaphysaire afin de faciliter la transmission des forces mécaniques dans l'ensemble de l'os, plutôt que de les forcer à se concentrer dans la région sous-chondrale lorsque peu de ponts sont présents, comme dans les os jeunes. En outre, un degré significatif de variabilité inter-échantillons a été observé dans le comportement mécanique des os jeunes, un phénomène notablement absent dans les os plus âgés.

L'impact de la présence ou de l'absence d'une plaque de croissance a eu un effet plus prononcé sur le comportement mécanique des os jeunes que sur celui des os plus âgés, étant donné la plus grande quantité de ponts reliant les régions sous-chondrales aux régions métaphysaires dans les échantillons plus âgés. La simulation d'une plaque de croissance pathologique, caractérisée par un module de Young plus élevé dans des échantillons jeunes, a révélé des modèles de déformation qui ressemblaient étroitement à ceux des os âgés, ce qui suggère que de tels changements pourraient imiter les altérations de la mécanique osseuse liées à l'âge.

Bien que l'analyse computationnelle ait fourni des indications précieuses sur la redistribution des contraintes dans la structure osseuse, elle n'a pas permis d'évaluer les charges de rupture. Pour remédier à cette limitation, des processus expérimentaux ont été mis au point afin de

déterminer spécifiquement les charges de rupture dans les échantillons jeunes et vieux.

Dans l'ensemble, cette étude fournit des informations précieuses concernant la relation entre la microstructure osseuse et son comportement mécanique sous-jacent au cours du vieillissement, en particulier au niveau de l'interface os-cartilage. Elle a démontré comment des structures osseuses spécifiques influencent les propriétés mécaniques dans les régions trabéculaire sous-chondrale, corticale sous-chondrale, trabéculaire métaphysaire et corticale métaphysaire, améliorant ainsi notre compréhension de la manière dont les forces mécaniques affectent l'os au cours du processus de vieillissement et des pathologies qui en découlent.

Acknowledgments

The conclusion of this master's thesis marks my initial and profoundly enriching experience, immersing myself in the research field for the first time. This experience has equipped me with valuable skills in critical analysis and problem-solving. I am deeply grateful to those whose encouragement and expertise were essential in the achievement of this work. Their invaluable support has been a continual source of motivation and strength throughout this endeavor, and I would like to express my heartfelt gratitude to them.

First of all, I would like to express my deep gratitude to my supervisor, Professor Davide Ruffoni, for his invaluable time, guidance and advice. His inclusion of me in his laboratory has been instrumental in the development of the work I present today. His unwavering enthusiasm for my research has continually motivated me to give my best. I would also like to thank him for his constant support in projects beyond my master's thesis.

I would also like to extend my gratitude to all the members of my jury for dedicating their time to read my thesis, attend my oral defense, and demonstrate a strong interest in my research.

Secondly, I wanted to personally express my profound gratitude to Laura Müller for giving me the opportunity to tackle this project. I particularly wanted to thank her for always being there for me, during moments of uncertainty and in times of success. Her expertise and deep understanding of her subject helped me enormously in carrying out this project. Her mentorship throughout the project, while allowing me to work on my own, was invaluable. I am incredibly grateful for everything she has done for me.

I would also like to extend my thanks to the entire MBBM laboratory for their help, guidance, and kindness.

I would also like to thank all the people who contributed to the achievement of this project. First of all, I would like to thank Piyush Uniyal for his exceptional assistance in understanding and utilizing the ParoSol software; his help was invaluable. I would also like to thank the CECI team, especially David Colignon and Orian Louant, for their readiness to help whenever I had questions. Finally, I would like to thank Quentin Grossman for taking the time to help me with conducting my compression tests.

On a more personal note, I want to express my heartfelt gratitude to all those close to me who have been unconditionally supportive in the achievement of this project. My family has been my pillar of support throughout these 5 years. I would like to thank my parents for always believing in me and allowing me to pursue these wonderful studies. I would also like to thank my friends, especially Puhia and Lena, with whom I have collaborated on numerous projects, forming a successful teamwork. Their support and enthusiasm have played a crucial role in making these 5 years of study truly rewarding and fulfilling for me.

Contents

List of acronyms

3D	Three Dimensional
CAD	Computed-Aided Design
CHU	University Hospital Center
CPU	Central Processing Unit
CT	Computed Tomography
DNA	DeoxyriboNucleic Acid
EFF	Effective Strain
FEA	Finite Element Analysis
FWHM	Full Width at Half-Maximum
KUL	Catholic University of Leuven
OA	Osteoarthritis
PBS	Phosphate Buffered Saline
PDF	Probability Density Function
ROI	Region Of Interest
SED	Strain Energy Density

Introduction

The tibia is one of the largest bones in the human body, playing an important role in weight-bearing and motion [1]. As a key component of the lower limbs, it connects the knee to the ankle and is stabilized mainly by soft tissues [2]. This bone undergoes continuous modeling and remodeling processes to adapt to the mechanical forces applied to it, accentuating the importance of its structural integrity in maintaining mobility. Consequently, an in-depth study of the tibia from a mechanical perspective is crucial for understanding its role in human movement and stability.

Bone is composed of a complex hierarchical system, giving it remarkable adaptability across various levels, in response to factors such as aging, certain pathologies, or physical activities [1]. Macroscopically, two types of bone are observed, i.e. trabecular and cancellous bone, both contributing distinct mechanical properties to the overall bone structure [3]. This hierarchical organization extends down to numerous hierarchical levels, making it an intriguing subject for study at lower scales. Advances in technology, such as micro-Computed Tomography (micro-CT), enable the detailed examination of bone at the nanoscopic scale. Micro-CT allows for the acquisition of high-resolution 3D images of bone, with a resolution of up to 10 μm, which can be used for μ-Finite Element simulations, providing deeper insights into bone mechanics.

Despite the joint's abilities to self-remodeling, certain pathologies, such as osteoarthritis or growth plate fusion, can significantly impact its mechanical behavior. Osteoarthritis, which affects over 500 million people globally [4], induces to various joint alterations, including articular cartilage degeneration, synovitis, and architectural changes [5, 6, 7]. The affected region comprises several layers, namely articular cartilage, epiphysis, growth plate, and metaphyseal bone, each of which contributes to the overall mechanical bone's behavior. An in-depth study of these separate and interconnected structures is, therefore, a pivotal element in understanding the resulting behaviors influenced by mechanical properties and aging. Given that there is currently no treatment to halt the progression of this disease, gaining a deeper understanding of this region is essential.

This study focuses on the three most important parts of the knee joint: the subchondral bone, the growth plate, and the metaphyseal bone. Its primary aim is to understand the impact of these structures on the resulting bone mechanics, as a function of age and the intrinsic mechanical properties of the bone. By employing both computational simulations and experimental processes, this work seeks to provide a comprehensive understanding of how aging and microstructural changes influence bone mechanics.

This study is divided into four main chapters. The first chapter focuses on establishing the key concepts necessary for understanding this thesis. To begin with, an in-depth description of bone and cartilage is given, detailing their composition, microstructure, and mechanical properties.

Additionally, it explains the bone-cartilage interface, which is central to this study. The chapter also presents two diseases affecting the knee joint to illustrate their impact on the region under study. Finally, the choice of using rats as animal models was explained, and the main aim of this master thesis was presented.

The second chapter details all the steps performed during the μ-finite element simulations and the experimental processes. In the computational part, it describes sample selection and preparation, image processing, and all the elements chosen for the simulations. The experimental part covers sample selection and preparation, as well as the entire process of positioning the bone in the machine and the loading conditions applied.

The third chapter presents the computational and experimental results. Firstly, bone mechanics are studied following changes in mechanical properties. Secondly, by stabilizing these properties, the impact of microstructure on bone mechanics is isolated. The chapter also explores the introduction of the growth plate, considering its mechanical properties and its impact on bone aging. Finally, it compares the computational results with experimental findings.

The fourth and final chapter discusses the results obtained in this study in relation to previous researches. It highlights the main limitations of this study and suggests directions for further explorations.

Chapter 1

Background

The main aim of this chapter is to introduce a fundamental overview essential for a comprehension of the core concepts addressed in this master thesis. Firstly, the musculoskeletal system will be presented in detail, with a particular emphasis on bone and cartilage. Their composition, structure and mechanical properties will be exposed. Subsequently, some crucial areas for the understanding of the present work will be highlighted, with a specific focus on the osteochondral junction and on the growth plate. An in-depth analysis of the osteoarthritis and growth plate injuries will be explored to grasp the implications of aging and alterations in mechanical properties. The discussion will then shift towards the use of animals in biomedical research, with particular emphasis on rats, chosen as the primary animal model in this study. Finally, the last section of this chapter will focus on the main aims of this master thesis.

1.1 The musculoskeletal system

To provide motion and support, give shape to the organisms, protect internal organs, and ensure biological functions such as hematopoiesis and mineral storage, the human body needs the musculoskeletal system. This system comprises various types of tissues. This report will exclusively concentrate on the two most important ones regarding this study, i.e. bone and cartilage [1].

1.1.1 Bone

Bone is a very intricate hierarchical system which has high adaptability at multiple hierarchical levels in response to various factors such as aging, diseases, or physical activity. Several types of bone exist and are characterized by unique biomechanical functions. The first type is long bones, including the tibia, femur, and humerus, which are designed to resist bending and buckling forces. On the other hand, short bones, including tarsals and carpels found in the feet and hands, are made to deform and accommodate for compression. This function is facilitated by a primary composition of spongy bone. Then, flat bones, including the sternum, ribs, and cranial bones, are found around vital organs to protect them or, when enough space is needed, to attach muscles. Finally, irregular bones, including vertebrae or sacrum, exhibit complex shapes to protect vital organs [8]. The present report will focus exclusively on long bones.

Long bones are characterized by two main components, i.e. the diaphysis and the epiphysis, depicted in Figure 1.1. The diaphysis is the medial part of the bone. It is a hollow shaft, mainly composed of dense cortical bone. The medullary cavity is the central hollow part of the diaphyseal region that contains bone marrow. On the other hand, the epiphysis is the end parts of a long bone. In between these two, the metaphysis part is located below the growth plate. This growth plate allows the formation of new bone during childhood development. This plate is made up of cartilage. Both epiphysis and diaphysis are made up of trabecular bone, a porous type of bone made up of trabeculae, surrounded by a thin layer of dense cortical bone [8]. The extremities of long bones are covered by articular cartilage reducing friction by ensuring a lubrication effect [9].

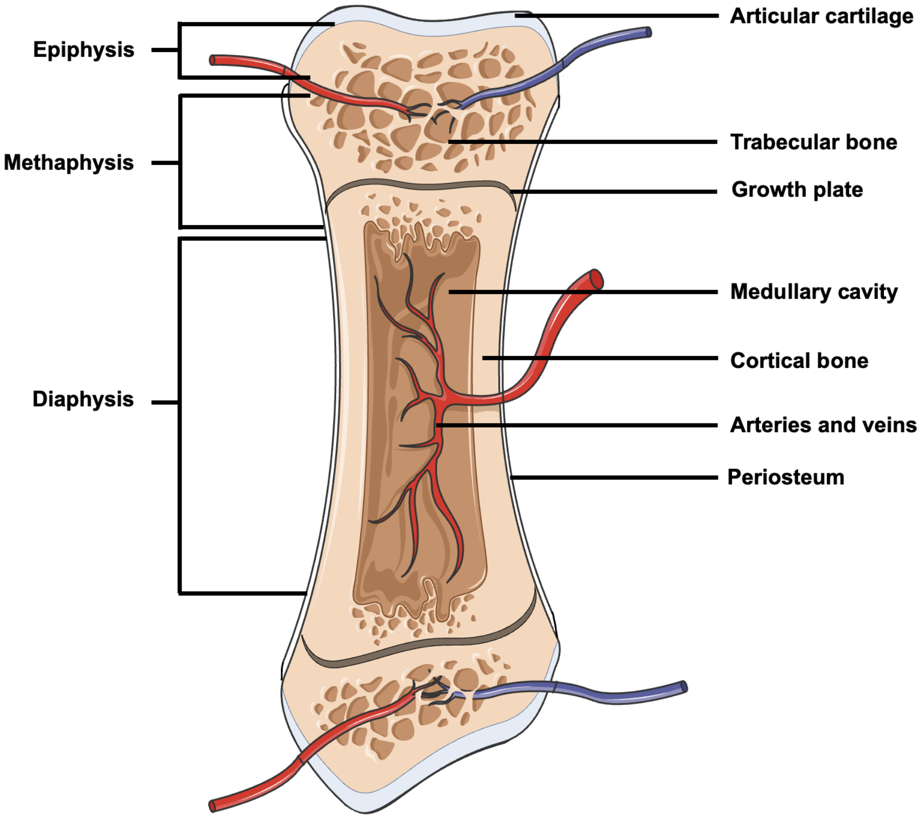

Figure 1.1: Illustration of the general structure of long bones. Adapted from [10] and [11].

1.1.1.1 Bone Composition

Bone is a composite material which is characterized by a two-phase structure. One phase is a stiff mineral component, referred to as the inorganic phase, which is embedded within another tensile polymeric phase, known as the organic phase [12]. In terms of weight percentage, bone is composed of 60% inorganic phase, 30% organic phase, and 10% water [13].

The organic phase is principally composed of type I collagen, constituting 90% of its weight. This type of collagen will mainly influence the mineralization process and, subsequently, the bone strength. In addition, smaller quantities of type III and IV collagen are present, contributing to the formation of type I collagen and helping in the extracellular matrix organization [14]. Finally, non-collagenous proteins such as osteocalcin, osteonectin, and osteopontin are also present. They play an important role in mediating interactions between organic and inorganic phases [13], as well as in bone formation/resorption, contributing to the dynamic nature of bone tissue [14].

The inorganic phase is composed of hydroxyapatite, which is a form of calcium phosphate ($Ca_{10}(PO_4)_6(OH)_2$). Nevertheless, pure hydroxyapatite is seldom found in nature due to the rich environment in which bone is formed. Various substitutions generally occur, involving ions such as potassium, magnesium, strontium, or sodium replacing Ca^{2+}; carbonate replacing PO^{4-}; and chloride, or fluoride ions replacing the OH^- ions [13]. These substitutions can alter the hardness and brittleness of bone, affecting its mechanical properties [14].

1.1.1.2 Bone Remodeling and Bone Mineralization

Bone is a living tissue since it is composed of living cells. Those cells ensure the formation and maintenance of the bone matrix through processes known as bone remodeling and bone mineralization.

In the process of bone remodeling, three primary types of cells play pivotal roles, i.e. osteoblasts, osteoclasts, and osteocytes. Osteoblasts are responsible for bone formation by synthesizing and depositing new bone matrix where it is required. On the contrary, osteoclasts are involved in bone resorption, meaning that they dissolve bone where no longer needed. Osteoclasts are unique cells that are multi-nucleated and capable of attaching to bone surfaces. Those two types of cells work together during the bone remodeling process by forming a cellular unit called Bone Multicellular Units (BMUs) [14]. The last type of cells involved in bone remodeling is the osteocytes. The osteocytes are osteoblasts, trapped within the bone matrix during the growth phase. These osteocytes act as information transmitters to surrounding cells, detecting mechanical forces exerted on bone. Acting together, they form a highly interconnected network, called canaliculi, used to exchange information and monitor strains by notifying changes in the local microenvironment [15].

These osteocytes and lacunocanalicular networks serve a dual purpose: firstly, to transport nutrients, and secondly, to connect osteocytes for communication. The presence of fluid within the canaliculi enables osteocytes to sense the mechanical strain, which makes bone highly responsive to any external stimuli [2] [38].

A distinction can be made between bone modeling and bone remodeling. Bone modeling is the process in which bone is removed from one site and formed at another site, leading to changes in bone shape. On the contrary, in the bone remodeling process, old bone is replaced with newly formed bone at the same site, resulting in a regeneration process. The process of bone remodeling can be decomposed into five main steps which are illustrated in Figure 1.2. The first step consists of the detection of the remodeling signal from osteocytes that triggers the resorption by osteoclasts. During resorption, signals generated by osteocytes are sent to osteoblasts to recruit osteoclast precursors. After that, a reversal phase occurs during which almost all osteoclasts disappear and are replaced by mononuclear cells which will prepare the bone surface for further osteoblasts arrival. Then, during the formation phase, osteoclasts are replaced by osteoblasts. This phase places the bone matrix where it is needed until all of the old bone is replaced by new bone tissue. Finally, a last signal is sent to induce the terminal differentiation of the osteoblast. At this stage, the bone surface is covered by lining cells, marking the achievement of the remodeling process [16, 17]. This remodeling process plays a crucial role in maintaining calcium homeostasis, adapting to mechanical stresses, and repairing microdamage.

Two weeks after the new bone deposition, a process which is called mineralization takes place. This process involves the gradual increase of mineral content in the newly formed bone matrix.

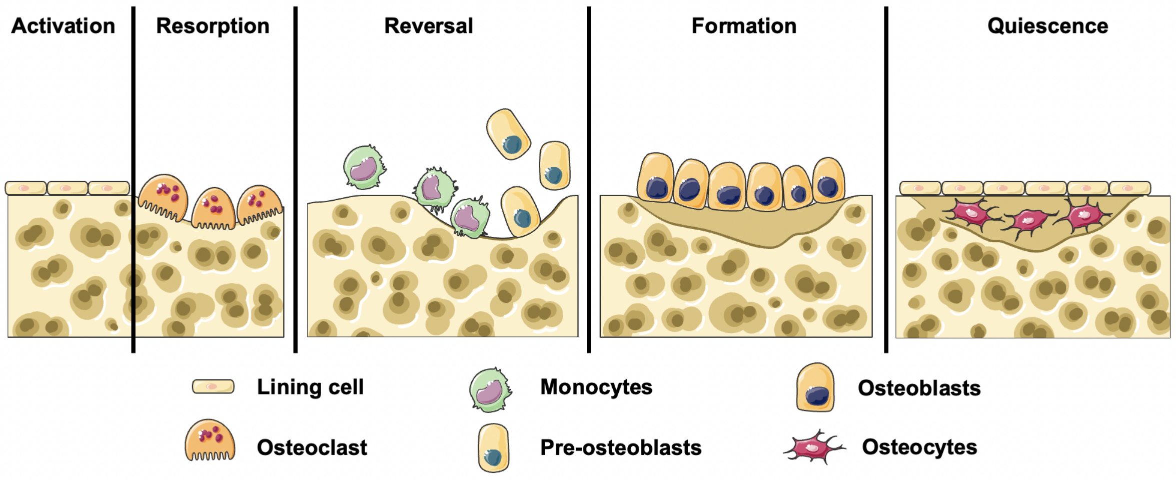

Figure 1.2: Illustration of the five main steps involved in the bone remodeling process. Adapted from [16] and [11].

By this calcium and phosphate intake, the stiffness of bone increases. Mineralization is characterized by an initial rapid phase, during which up to 80% of calcium and phosphate content are added to the bone matrix. This initial phase lasts two to three weeks. Then, the mineralization process keeps on at a slower rate [18]. This process induces a variation in mineralization level at different sites in bone. Indeed, new bones are much less calcified than older ones [19].

1.1.1.3 Hierarchical Structure of Bone

Bone is a unique material that combines high stiffness with high toughness. This combination is achieved through a hierarchical structure, with different levels of organization adapted to specific local needs and functional requirements. It exists five hierarchical levels in bones which are the macroscopic level (higher than 500 μm), the microscopic level (from 10 to 500 μm), the sub-microscopic level (from 1 to 10 μm), the nanoscopic level (from few hundreds of nm to 1 μm) and finally the sub-nanoscopic level (under hundreds of nm). Those levels and their associated structures are depicted in Figure 1.3.

Macroscopic level

At the macroscopic level, bone can be categorized into two types: cancellous (or trabecular) bone and cortical bone [3]. These two types differ in porosity, density, and structural organization. Despite those distinctions, both types of bone are made up of the same material, namely lamellar bone. As illustrated in Figure 1.1, cortical bone forms the dense outer layer, while the trabecular bone is located at the ends of long bones [14].

Cancellous bone consists of irregular trabeculae forming an interconnecting mesh-work separated by the bone marrow [20]. This type of bone is much more metabolically active because it undergoes more frequent remodeling. This impacts its mechanical properties. Indeed, the frequent remodeling contributes to a generally lower mineralization compared to cortical bone, as there is less time for mineral deposition. Those properties will be described in-depth in Section 1.1.1.4.

On the other hand, cortical bone is composed of regular, cylindrical lamellae that strengthen the tissue by forming structures known as osteons. This type of bone is characterized by a dense

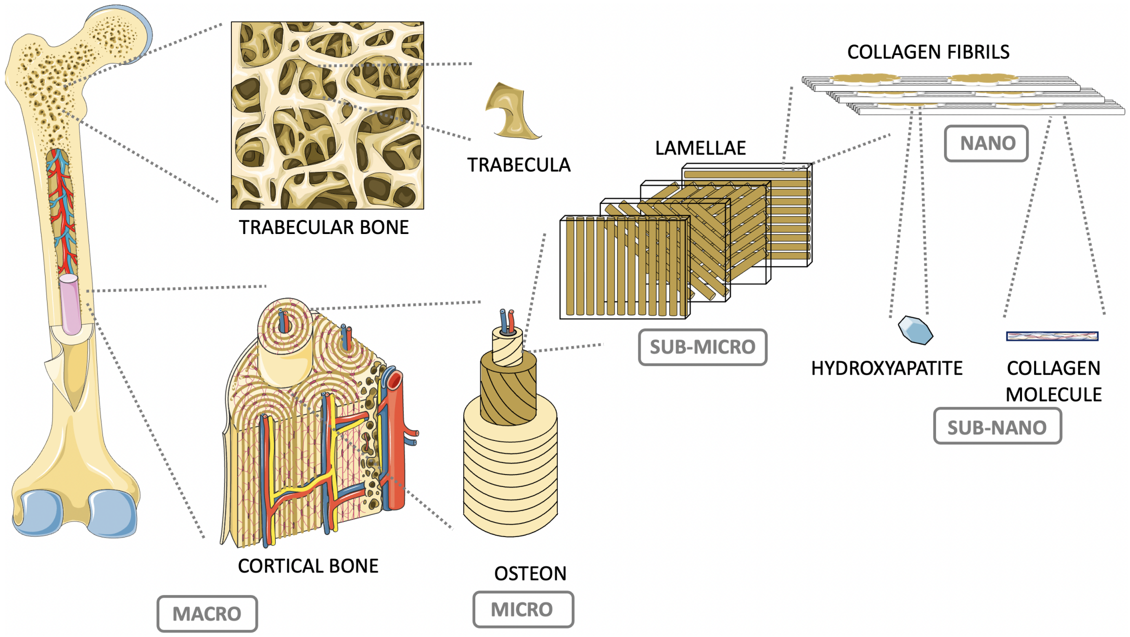

Figure 1.3: Illustration of the hierarchical structure of bone. Adapted from [3] and [11].

and compact structure. It has a porosity ranging from 20 to 30% compared to 40 to 95% for trabecular bone. Consequently, bone remodeling is less important in cortical bone since free surfaces are less prominent [13].

Microscopic level

At the microscopic level, from 10 to 500 μm, some key structural elements of bone can be distinguished, including Haversian canals, osteons, and single trabeculae [3].

The key structural element of cortical bone is the osteon. Osteons are cylindrical structures oriented parallel to the long axis of the bone, as illustrated in Figure 1.4. Each osteon is composed of 10 to 15 concentric layers of mineralized collagen fibers [17]. Haversian canals, located at the center of the osteon, contain blood vessels, nerves, and bone cells. Their primary function is to protect them from microcracks but also to bring nutrients and get rid of waste [3]. In addition to osteons, there are also layers of lamellae parallel to the cortical bone surface, as shown in Figure 1.5.

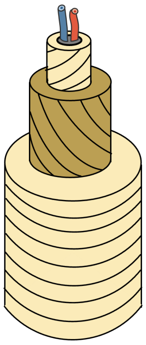

Figure 1.4: Illustration of the osteon structure in bone. Adapted from [3] and [11].

In the trabecular bone, the key structural element is trabeculae. They can be either plate-like or

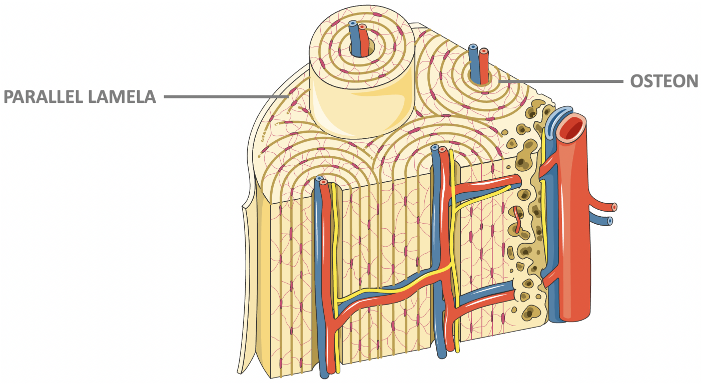

Figure 1.5: Illustration of the cortical bone organization. Adapted from [11].

rod-like structures as illustrated in Figure 1.6. Trabecular bone is characterized by an interconnected network of trabeculae, which creates a porous structure. There are two different types of structure for trabeculae, i.e. plate-like and rod-like. Plate-like trabeculae seem to exhibit a higher stiffness since they exhibit a flattened structure which can sustain higher stresses. On the other hand, rod-like trabeculae target a higher energy resorption and a higher deformability since they are more elongated and cylindrical [21]. Since there exist two different types of structures for trabeculae, it is difficult to obtain their proper mechanical properties. Those two types of trabeculae are important in adapting bone to meet specific mechanical requirements and respond effectively to various mechanical loading.

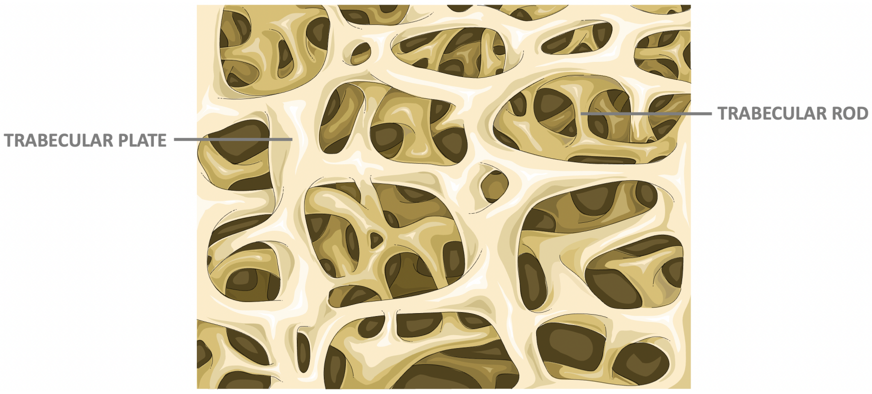

Figure 1.6: Illustration of the trabecular bone organization. Adapted from [11].

Sub-microscopic level

At the sub-microscopic level, ranging from 1 to 10 μm, lamellae are distinguished. At this point, cortical and trabecular bones cannot be differentiated anymore. Those are collagen fibers stacked into thin sheets. The collagen fibers are parallel within the same sheet but they are oriented at different angles from sheet to sheet as depicted in Figure 1.7. This type of structure is named as a **twisted plywood** structure. This twisted plywood model has been validated by *T. Yamamoto et Al.* [22] under the assumption that cellular control is present, meaning that bone cells control the fibrillar arrangement and ensure this organization within this lamellar structure. The thickness of the sheets is comprised of between 3 and 7 μm [3, 23].

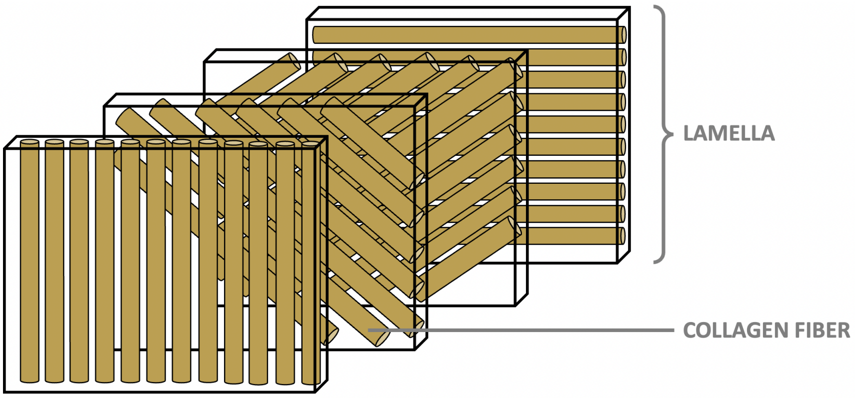

Figure 1.7: Illustration of the twisted plywood structure.

Nanoscopic level

At the nanoscopic level, ranging from hundreds nm to 1 μm, bone exhibits a composite structure made of collagen fibrils embedded in a matrix of minerals [3]. Those two components do not assemble in a random way. Collagen molecules are aligned parallel to each other and covered with mineral crystals. They are around 10 μm long and 100 nm in diameter [24], while the crystals are around a few nm in size. As well as being parallel to each other, the fibrils are also staggered along the axial direction. Collagen molecules are parallel but staggered along the axial direction, with an offset of about 67 nm between adjacent planes, as illustrated in Figure 1.8. This staggered arrangement allows for some shearing of collagen molecules, which helps prevent brittle failure. Due to the non-integer length of collagen molecules relative to the 67 nm stagger, gaps and overlaps occur in the structure. These gaps serve as nucleation sites for the formation of mineral particles, which are crucial for bone mineralization [25].

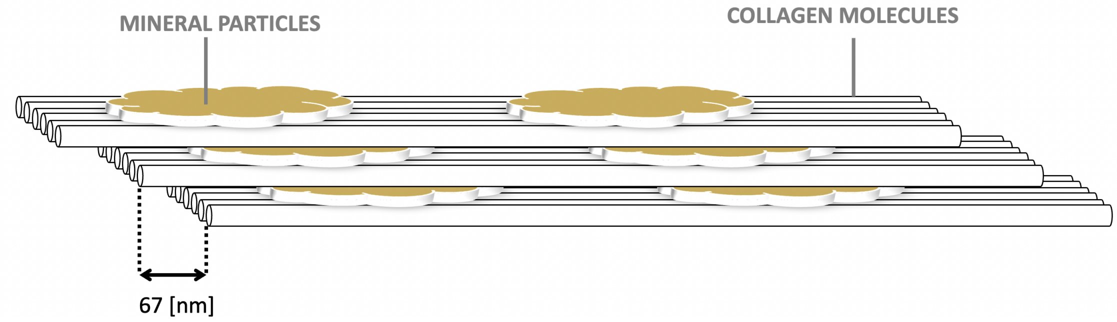

Figure 1.8: Illustration of the mineralized collagen fibril structure.

Sub-nanoscopic level

At the sub-nanoscopic level, at less than hundreds nm, collagen molecules, non-collagenous proteins, and bone mineral crystals can be distinguished [3]. Mineral crystals consist in hydroxyapatite which is a form of calcium phosphate.

Type I collagen fibers exhibit a highly hierarchical organization. Indeed, they present several distinct levels of structures as depicted in Figure 1.9. At the primary level, collagen is formed by three peptidic chains of five to six amino acids in the sequence Gly-X-Y where Gly denotes glycine, X designates proline, and Y designates hydroxyproline. Due to the steric repulsion of proline residues, these amino acids adopt a α-helix conformation. Some peptidic bonds are formed to maintain this α-helix in place. In type I collagen, it is composed of two α_1 chains and one α_2 chain. These chains are differentiated by their amino acid sequence. Thanks to this arrangement, the helix is stiff but flexible. This helix arrangement is called tropocollagen molecules and has a typical length of about 300 nm. Those molecules then self-assemble in a staggered fashion to form collagen fibrils. Those fibrils are never alone since they are always arranged in a bundle of fibrils to form collagen fibers [26].

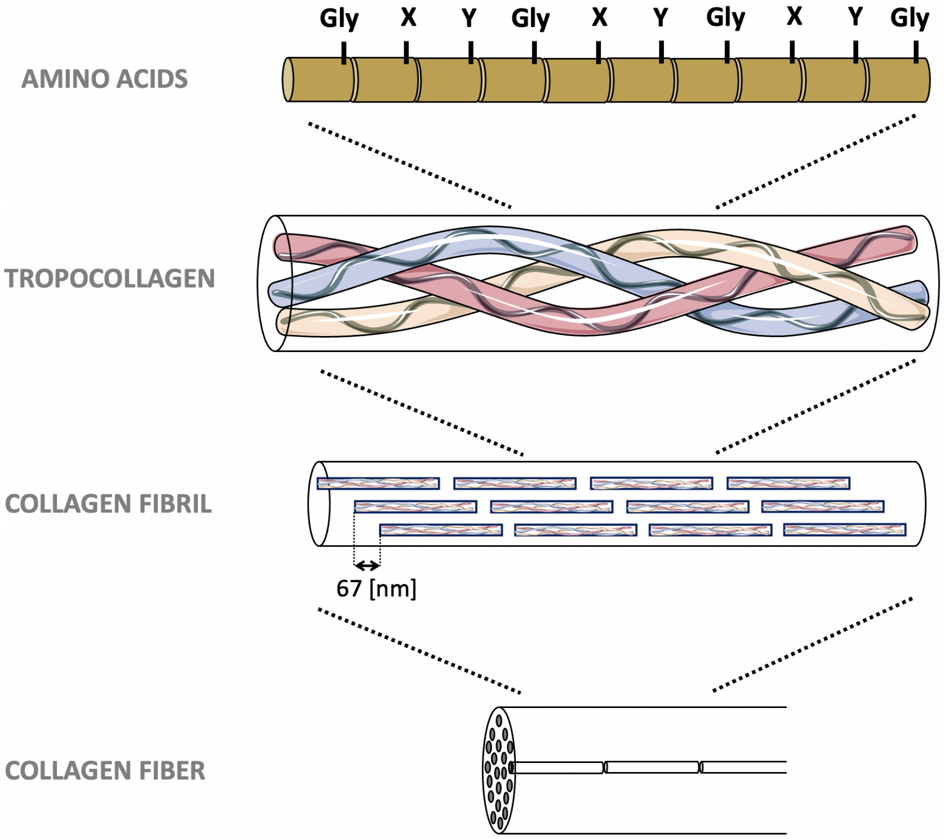

Figure 1.9: Illustration of the hierarchical structure of collagen fibers. Adapted from [27] and [11].

1.1.1.4 Mechanical Properties of Bone

Bone is defined by its hierarchical structure and composition. As stated before, bone is defined by a hierarchical structure. At the macroscopic level, two types of bone are present, i.e. trabecular and cortical bone. While a similar composition (collagen molecules reinforced by hydroxyapatite), they present different macroscopic structures leading to different macroscopic mechanical properties [15].

Cortical Bone

Cortical bone is made of longitudinal osteons and oriented lamellae, which contribute to its highly anisotropic properties. That implies that, along the main axis of the bone, properties are higher compared to the transverse direction. In the plane perpendicular to the main axis, properties are isotropic, rendering this material transversely isotropic [13]. Moreover, its mechanical properties in compression are greater compared to tension. This is advantageous since bone is generally subjected to compressive loads along its main axis. This underlines the "optimization" of biological materials to perform their functions effectively [15]. Cortical bone is also inhomogeneous since its properties vary in space. For instance, the human cortical bone has a longitudinal Young's modulus comprised between 10 and 22 GPa while its longitudinal compressive stress is comprised of between 170 and 210 MPa [13, 14].

Concerning its stress-strain diagram, it exhibits two distinct types of curves depending on whether it is subjected to tension or compression, as well as whether it is loaded in the longitudinal or in the transverse direction as depicted in Figure 1.10. In all cases, cortical bone exhibits a sigmoidal curve characterized by a linear elastic phase, a yield point, and a plastic region. Young's moduli exhibit similar values for both compression and tension, as well as for longitudinal and transverse directions. However, there are also some differences. The ultimate stress is higher in compression compared to tension, indicating a higher strength in compression. Additionally, in the longitudinal loading, the ultimate stress is higher in compression. On the other hand, ultimate strain is lower in compression. On the contrary, for the transverse loading, ultimate stress and ultimate strain are both higher in compression [13]. Those differences highlight the anisotropic nature of cortical bone.

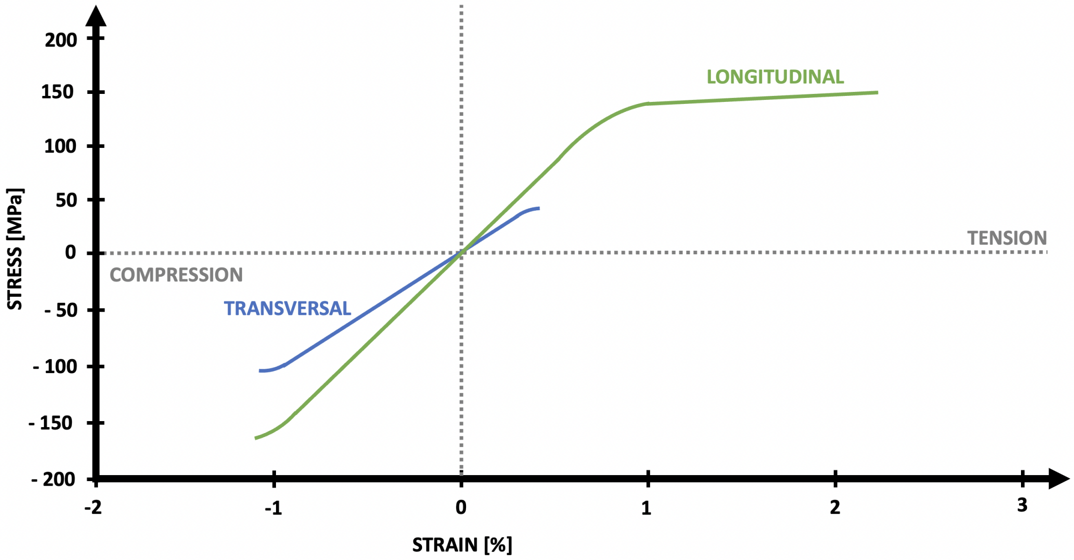

Figure 1.10: Stress-strain curve of cortical bone in compression and in tension, depending on the axis of loading.

This high anisotropy in cortical bone can be attributed to the mechanism of crack propagation within this type of bone tissue. During longitudinal loading, cracks have a tendency to propagate in the transversal direction with respect to the main axis of the bone, as seen in Figure 1.11. When cracks encounter osteon oriented in the transversal direction (longitudinal loading), they are deflected. The path followed by the cracks is tortuous which leads to a rough surface. Consequently, those deflections enable a lot of energy dissipation. On the other hand, for the longitudinal propagation (transversal loading), cracks propagate in between osteons since they are oriented in the same direction as the crack propagation, as seen in Figure 1.12. The propagation is much more straightforward which gives a relatively smooth crack surface compared to longitudinal loading [13]. In this case, only few energy can be dissipated.

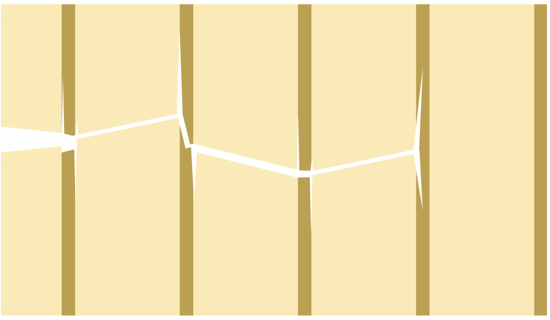

Figure 1.11: Illustration of the crack propagation in longitudinal loading of the cortical bone.

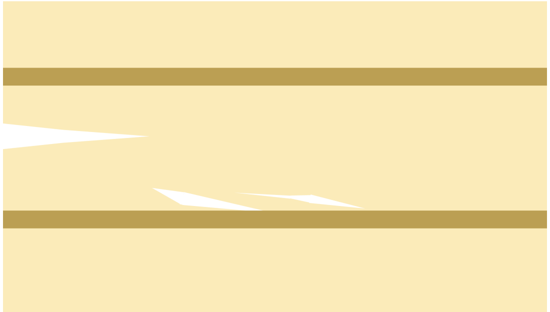

Figure 1.12: Illustration of the crack propagation in transversal loading of the cortical bone.

Trabecular Bone

Trabecular bone is highly heterogeneous, with its properties particularly dependent on the amount of tissue, the composition of the matrix, and the structure of the trabeculae. Relative density and architecture of trabecular bone can vary considerably based on factors like age, disease state, and anatomical site. Due to those variabilities, establishing a unique value for the stiffness and strength of this type of bone is impossible. This emphasizes the importance of personalized assessment of mechanical properties of trabecular bone [15, 14].

Its stress-strain diagram in compression typically exhibits three main phases, as depicted in Figure 1.13. The initial phase is the linear elastic one. In this phase, strain increases linearly with stress. This phase ends when there is a collapsing of trabecular rods and plates. The second phase is the plateau region where strain increases without any change in stress. This is possible thanks to a form of failure of the trabeculae which allows energy absorption without complete destruction of the structure. Finally, there is a densification region where strain increases with stress but not linearly this time. This indicates an irreversible damage of the material due to the contact between trabeculae resulting in densification of the tissue. The obtained type of curve significantly depends on the apparent density of the trabecular bone as can be seen in Figure 1.13. As the apparent density decreases, the length of the plateau region expands, permitting a large increase in the strain. On the other hand, while increasing the apparent density, the slope of the linear elastic region rises, giving a higher value of Young's modulus.

In tension, the trabecular bone exhibits different mechanical behavior, as highlighted in Figure 1.14. Indeed, in tension loading, the stress-strain curve exhibits a linear elastic phase followed by a complete fracture of the material. Unlike compression loading, the plateau and densification phases are no longer present. Instead, the material reaches its ultimate tensile strength at which the material fractures.

1.1.2 Cartilage

It exists three different types of cartilage. The first type is the articular cartilage which covers joint surfaces. Fibrocartilage is the second type which is present in the menisci, at the interface between bone and tendon/ligament, and in the annulus fibrosis of intervertebral disks. The third type is the elastic cartilage which composes outer ear, nose tip, and larynx. In the present work, a unique focus on articular cartilage (or hyaline) is made. The primary functions of articular cartilage are to minimize friction, achieving the lowest possible coefficient of friction, and to

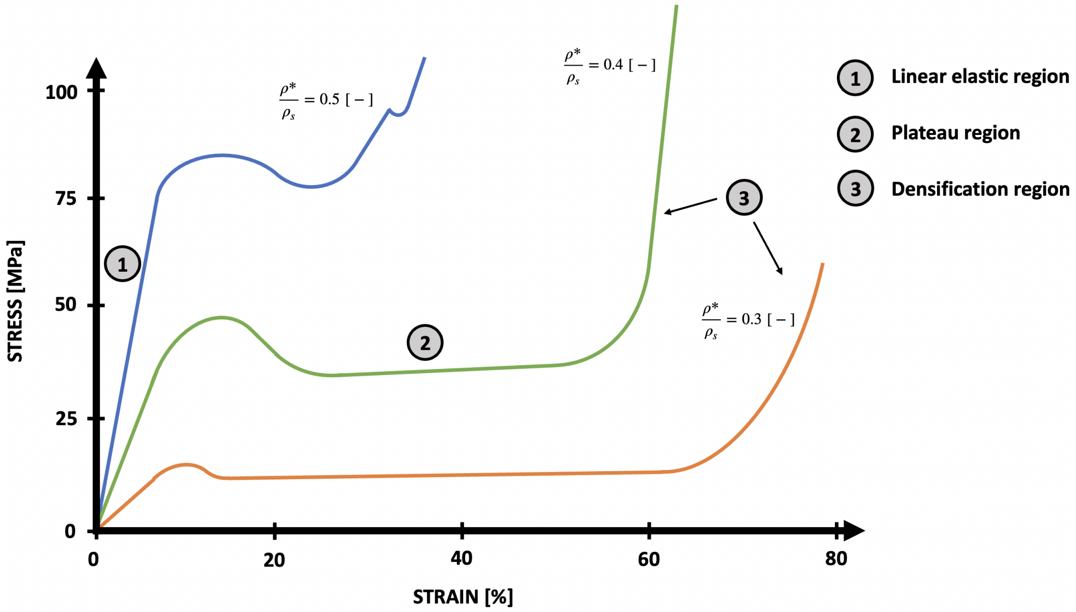

Figure 1.13: Stress-strain curve of trabecular bone in compression for three different apparent moduli.

transmit high forces between bones. It redistributes contact stresses across larger surfaces, enhancing the efficient transmission of forces to the underlying bone [28] [29].

1.1.2.1 Cartilage Composition

The cartilage cells are called chondrocytes which are embedded within an extracellular matrix. The main components of this matrix are water (70-90% of wet weight), type II collagen (10-20% of wet weight), and proteoglycans (4-7% of wet weight). In smaller amounts, non-collagenous proteins and glycoproteins are present to maintain its mechanical properties by conserving water into the extracellular matrix. Compared to bone, cartilage is not an innervated tissue so the only way to bring nutrients and remove the waste products is through the synovial fluid. [13].

Proteoglycans are macromolecules composed of a long protein core and polysaccharides side chains. Those sugar side chains are of two types, i.e. keratan sulfate chains and chondroitin sulfate chains. Those proteoglycans are rarely found alone in cartilage. Indeed, they aggregate to form aggrecans. Typically, aggrecans are formed by 100 chondroitin sulfate chains and 50 keratan sulfate chains. Some of those macromolecules then assemble to form hyaluronate, as depicted in Figure 1.15. Those units are attached through a link protein to the hyaluronic acid backbone. From a dimensional point of view, this molecule is 1200 nm long and the side chains are 200-400 nm long. Because of those big dimensions and the presence of negative charges in the chains, aggrecans are immobilized within the collagen network [13].

On the other side, water, present in large quantities (80% of its wet weight), has a huge contribution to the mechanical behavior of cartilage. Indeed, its main functions are the distribution of nutrients to chondrocytes as well as ensuring lubrication. The motion of water within the extracellular matrix is enabled thanks to the pressure gradient across the tissue or compression. Nevertheless, this flow is counteracted with a high frictional resistance. Those two mechanisms allow cartilage to resist high loads [28].

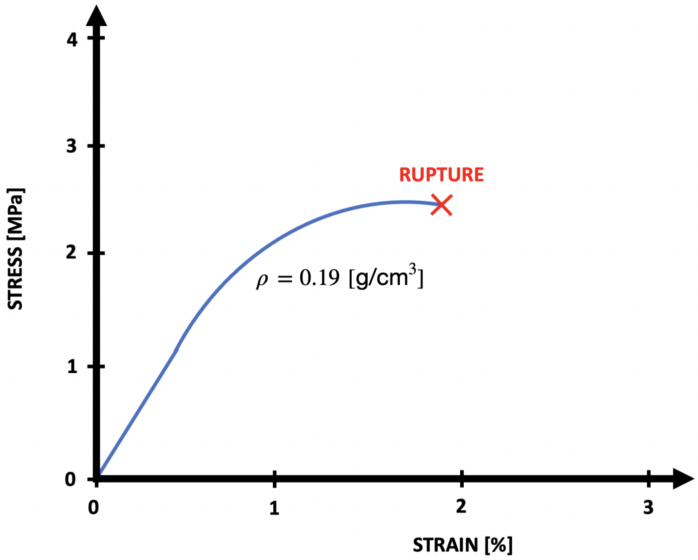

Figure 1.14: Stress-strain curve of trabecular bone in tension.

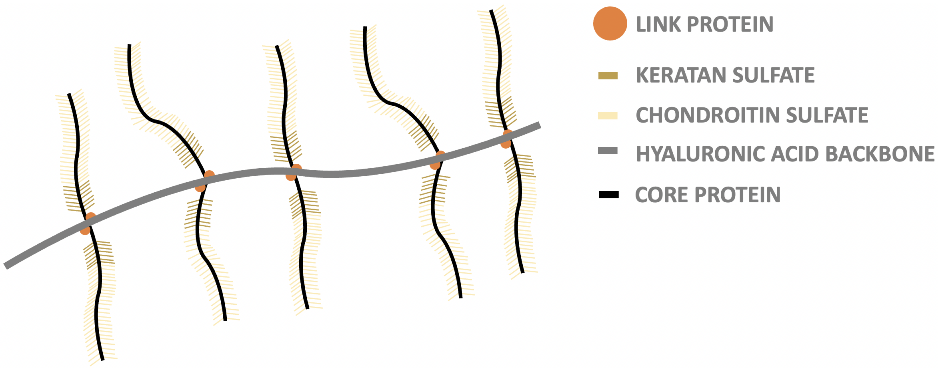

Figure 1.15: Illustration of the hyaluronate organization.

Collagen is also present in large quantities in the extracellular matrix (60% of dry weight of cartilage). Type II cartilage forms fibers which are interlaced within aggrecans. This type of collagen represents 95% of the collagen present in the extracellular matrix. The others 5% are there to form and stabilize fibers of type II collagen. Thanks to the structure of collagen, shearing and tensile properties of articular cartilage are greatly improved. Thanks to those properties, the matrix can be stabilized [28].

Finally, chondrocytes play a huge role in the development, maintenance, and repair of this extracellular matrix by synthesizing collagen and proteoglycans. The amount, shape, and size of chondrocytes vary depending on the region in the articular cartilage, as explained earlier in Section 1.1.2.2. They respond while simulated by stimuli such as growth factors, mechanical loads, piezoelectric forces, or hydrostatic pressures. Nevertheless, one of the main drawbacks of those cells is their limitation in replication. This explains why cartilage has a slow healing process after injury [28].

1.1.2.2 Cartilage Structure

Articular cartilage has a thickness of 2 to 4 mm. Within this thickness, several zones can be highlighted, as depicted in Figures 1.16 and 1.17.

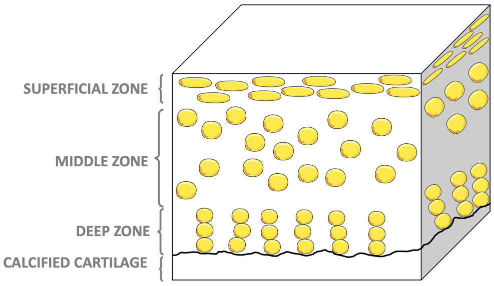

Figure 1.16: Illustration of the cell organization in the articular cartilage.

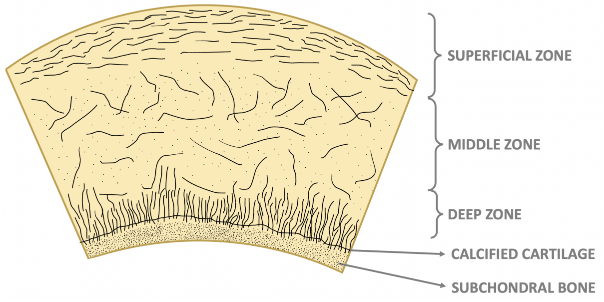

Figure 1.17: Illustration of the collagen organization in the articular cartilage.

The first layer is the superficial layer or superficial zone. It occupies 10 to 20% of the cross-section of the articular cartilage. In this region, there are very thin collagen fibers oriented more or less parallel to the surface to ensure a smooth surface. This orientation also enables compliance for the lubrication of the joint-to-joint contact. This allows the protection of the deeper layers from shear stresses. It is the region where the collagen content is the highest but where the proteoglycan content is the lowest. Finally, elongated chondrocytes are also present in between the collagen fibrils [13, 30].

Below this superficial zone, there is the middle zone which represents 40 to 60% of the cross-section of the articular cartilage. In this zone, relatively large collagen fibers oriented randomly are present. This random organization allows isotropic properties. In this part of the cartilage, chondrocytes are rounder and homogeneously dispersed between collagen fibers. This enables the first resistance to compressive stresses [13, 30].

Below the middle zone, there is the deep zone which represents 30% of the cross-section of the articular cartilage. It includes large collagen fibers oriented perpendicularly to the bone surface. This zone contains the highest amount of proteoglycan and the lowest water content. Moreover, chondrocytes are present in column form and are arranged in between collagen fibers. This zone enables great resistance to compressive forces thanks to the perpendicular orientation of the collagen fibrils [13, 30].

Finally, the last cartilage zone is the calcified cartilage which enables the anchoring of the collagen fibrils of the cartilage in the bone. Between calcified and uncalcified cartilage, there is a line which is named as the tide mark [13, 28, 30].

1.1.2.3 Mechanical Properties of Cartilage

Articular cartilage transmits and distributes evenly the force between bones within a joint. It also ensures a free movement of the bone with minimal friction by ensuring the smoothest surface possible. This friction is largely reduced thanks to lubrication by the synovial fluid, located between the opposing layers of cartilage [15, 28]. The load-bearing capability of cartilage is due to a combination of fluid pressurization and the solid matrix. Another important component that comes into play in the mechanical behavior of cartilage is the flow-independent behavior of the matrix composed of collagen and proteoglycans. The flow is highly restricted by intrinsic properties of cartilage. Finally, swelling in the cartilage tissue, driven by the ionic phase, contributes to the resistance of the fluid flow around the extracellular matrix. This swelling behavior is also controlled by intrinsic properties of the cartilage matrix [13].

The upper part of cartilage, known as the superficial zone, is relatively impermeable to fluid flow which ensures good fluid retention in the matrix of collagen, particularly during compression. This impermeability enables cartilage to withstand more than 90% of the load that is supported by the fluid in the cartilage, during compression [15, 31].

The compressive behavior of cartilage can be assessed through confined compression creep tests. As illustrated in Figure 1.18, a rigid cylinder encloses a cartilage-bone plug. Since the cylinder is totally rigid, deformation occurs solely in the loading direction, allowing for a uniaxial strain test to be imposed. The fluid can swell only from the top during compression tests thanks to a porous filter that imposes constant stress. As the test progresses, creep occurs as the fluid flows out of the plug. When the flow of the fluid stops, a steady state is reached. At this point, the equilibrium compressive modulus can be determined, related to the steady-state response in a creep test. Figure 1.19 highlights the viscoelastic property of the cartilage. Indeed, a time delay can be observed between the application of the load and the transient response. Then, cartilage will reach a steady state equilibrium which is governed by the intrinsic equilibrium modulus of the solid matrix of articular cartilage. The stress-strain curve in compression is linear up to 20% strain. The Young's modulus of articular cartilage, which is directly derived from the initial linear region of the stress-strain curve, varies from 0.3 to 1.3 MPa [13].

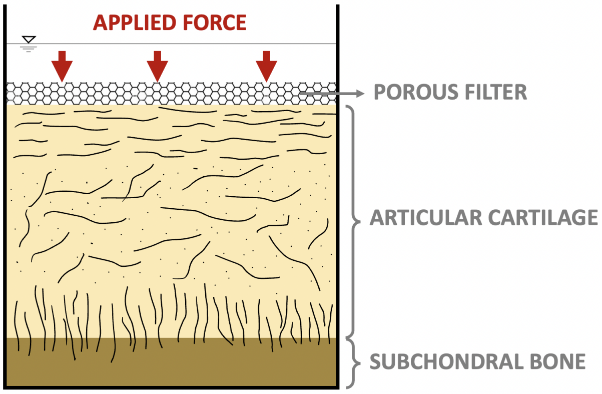

Figure 1.18: Illustration of the setup to perform a compressive test of articular cartilage.

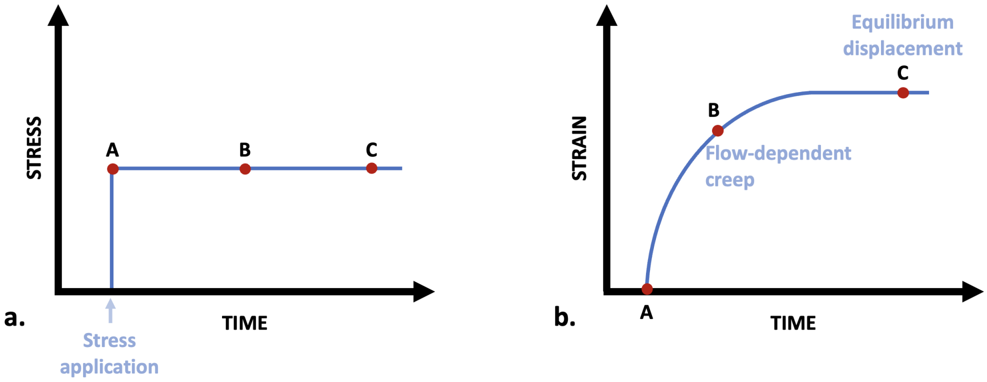

Figure 1.19: Graph of the **a.** stress versus time and of the **b.** strain versus time of articular cartilage during a compressive test.

Since cartilage becomes stiffer with strain, the compressive properties of articular cartilage cannot be described by a single value of Young's modulus. Instead, compressive properties are given by the aggregate modulus, i.e. the stress at equilibrium over the strain at equilibrium. This gives some information about the intrinsic compression properties, as it is primarily dependent on the properties of the cartilage matrix. The aggregate modulus is influenced by several factors, such as the content of proteoglycans in the extracellular matrix. An increase in proteoglycan content leads to an increase in the aggregate modulus. This can be attributed to the fact that when adding more proteoglycans, a lot of charges are added which makes the system stiffer. Indeed, during compression, these charges come into closer proximity, resulting in higher repulsive forces and overall increased stiffness of the cartilage matrix. Collagen also contributes to the compressive behavior of cartilage. On the one hand, it constrains the proteoglycan's movements since those big molecules are embedded in the collagen network. On the other hand, collagen is pre-stressed in tension due to the osmotic pressure generated by negatively charged proteoglycans [13].

Articular cartilage is highly anisotropic, meaning that the mechanical behavior in tension differs from that under compression. In Figure 1.20, the stress-strain curve of an articular cartilage subjected to tensile loading at a low constant rate is depicted. Three main phases can be highlighted, i.e. the toe phase, the linear region, and the failure at the end. During the toe phase, there is a small increase in stress compared to the increase in strain. This type of behavior is associated with the alignment of collagen fibers in the extracellular matrix. Then, there is the linear phase when the stress increases linearly with strain. The Young's modulus can be calculated in this phase and it typically varies between 40 and 400 MPa. This considerable variation in Young's modulus can be attributed to the discrepancy in-depth, the orientation of the cartilage, and the strain rate. At lower test speeds, a more accurate equilibrium modulus can be found whereas at higher rates, the tensile modulus tends to increase with this rate of loading [13].

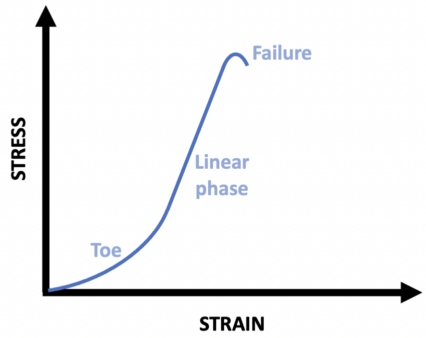

Figure 1.20: Stress-strain curve of the articular cartilage subjected to tensile loading at a low constant rate.

1.2 Bone-cartilage interface

The junction between bone and cartilage, known as the osteochondral junction, plays a crucial role in ensuring tissue integrity between these two distinct materials. Indeed, as stated in previous sections, those two materials differ from a structural and mechanical point of view. This area encompasses several layers, including the deepest layer of the non-calcified cartilage, the tidemark, the calcified cartilage, the cement line and the subchondral bone plate [32, 33].

As illustrated in Figure 1.21, the tidemark is a thin line of approximately 10 μm width, delineating the boundary between calcified and uncalcified cartilage. The presence of prolongations in the uncalcified cartilage causes the tidemark to follow irregular contours. It dives into the calcified cartilage until meeting the underlying bone or marrow area. This line is currently involved in mineralization and force transfer between bone and cartilage [32]. The formation of the tidemark occurs after puberty [5].

The other important demarcation line is located between cartilage and bone, named as the cement line. This osteochondral junction is stabilized during bone maturation. This allows to establish the transition between cartilage and subchondral areas of the joint [34]. Similarly to the tidemark, this cement line does not follow a straight path, reflecting the particular structural organization within the osteochondral junction.

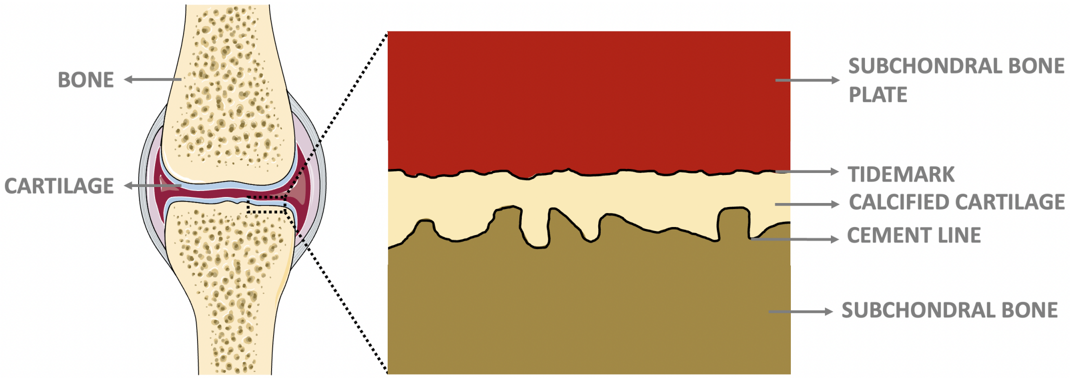

Figure 1.21: Illustration of the different layers present in the osteochondral area. Adapted from [11].

From a dimensional perspective, the average thickness of the calcified cartilage is approximately $104.6\ \mu$m for humans [35]. This thickness tends to decrease with aging, due to repeated load applications, which induces an increase in the load on the surface of the joint. The tidemark thickness is about $9\ \mu$m in regions subjected to load and 4 mm in non-loading regions [5]. With aging, the thickness of this line typically increases. The mean thickness of the subchondral bone is approximately $216\ \mu$m. In this type of tissue, aging and sex parameters do not significantly influence this parameter [5]. The mean thickness of the articular cartilage in the knee joint is roughly 2.34 mm. However, several factors such as aging, sex, and disease could negatively impact the cartilage thickness [36]. Finally, the thickness of the cement line has been established to be about $1\ \mu$m [37]. It is thus in a very thin region that the transition between cartilage and bone occurs.

The bone-cartilage interface region is also responsible for tissue mineralization, directing cells to the appropriate chondrocytes [38]. Within the calcified cartilage, chondrocytes are embedded in the extracellular matrix, contributing to the remarkable stiffness of the anchor cartilage [38]. The osteochondral junction facilitates the gradual transition of loads from the cartilage to the subchondral bone, moderating the stress concentration caused by the significant difference in stiffness between these tissues. On the other hand, the wavy contour and the presence of collagen fibers in this area help to reduce shear forces and resist crack propagation. In adult joints, fractures typically occur at the tidemark line [39].

1.3 Growth Plate

Another important long bone area is the growth plate. This unique region enables the longitudinal growth of the bone. This area consists of a thin sheet of hyaline cartilage and is located between the epiphysis and the metaphysis of the bone [33].

This region is composed of three primary zones which are the reserve zone, the proliferative zone, and the hypertrophic zone as illustrated in Figure 1.22. From a cellular perspective, each zone contains chondrocytes surrounded by a thin sheet of pericellular matrix. This pericellular matrix contains proteoglycans which enables the diffusion of large molecules. This matrix also contains type VI collagen. Its main role seems to be a mechano-transducer and a transition zone between cells and matrix [40]. In the reserve zone, chondrocytes are flattened, with those closer to the proliferative zone being flatter than those near the epiphyseal bone which are rounder. In the proliferative zone, chondrocytes are organized in a column manner since chondrocytes, moving from the reserve zone, are aligned with the longitudinal chondrons. Near the reserve zone, chondrocytes that are flatter are named as mother cells. In the hypertrophic zone, chondrocytes grow until reach up to five times greater diameter which induces an increase in the cell-to-matrix ratio in this region.

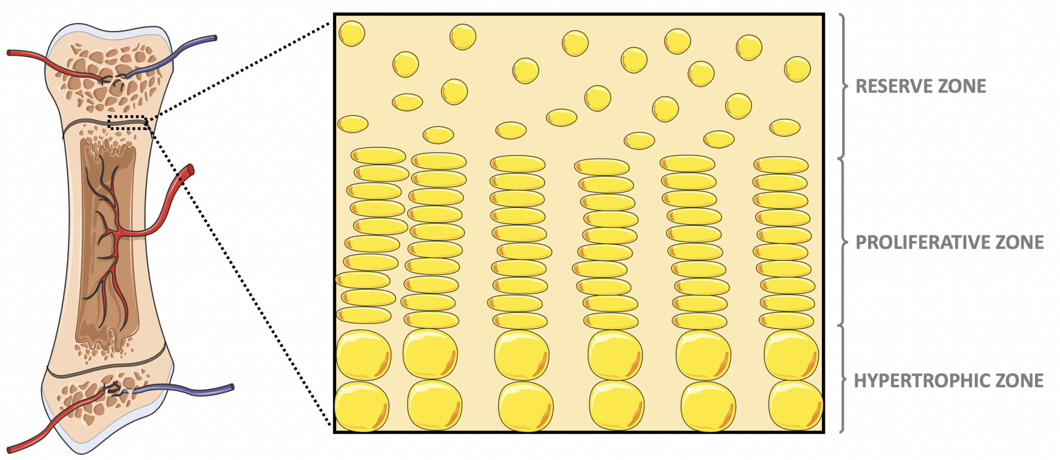

Figure 1.22: Illustration of the cellular structure of the growth plate. Adapted from [41] and [11].

As mentioned earlier, the first zone of the growth plate is the reserve zone. It contains chondrocytes which are positioned irregularly within the extracellular matrix. Although its role is quite unclear but several potential roles have been highlighted. The first one is the storage site for nutrients, for later needs thanks to its higher lipid concentration within the chondrocytes vacuoles. Its second hypothetical role is to secrete morphogens that contribute to the alignment of chondrocytes into columns called chondrons. These chondrons are the basic anatomical and functional units of cartilage. Those units are clustered around nutrient arteries that originate in the subchondral bone plate and terminate in the proliferative zone of a cluster of chondrons. Finally, its last role is to prevent hypertrophy of proliferative cells by releasing hypertrophy-inhibiting morphogens [33].

The second zone of the growth plate is named as the proliferative zone. Failure generally occurs between this zone and the reserve zone with chondron clusters ripped off in the reserve zone. Nevertheless, in the metaphysis, chondrons remain intact, suggesting a robust connection between different chondrons. Its primary functions are matrix production and cell proliferation which collectively enhance the longitudinal bone growth, in conjunction with the hypertrophic zone [33].

The final region of the growth plate is named as the hypertrophic zone. This zone is formed through the final differentiation of the proliferative cells. Its main contribution is dedicated to endochondral ossification, by preparing the matrix for calcification by incorporating calcium phosphate minerals into the extracellular matrix [33].

The structural integrity and attachment between bone and cartilage are achieved by the mammillary processes of the growth plate. These are undulations observed at the tissue interface that evolve during bone growth. Mammillary processes on the metaphyseal side are ensured by endochondral ossification, while on the epiphyseal side, undulations mimic the pattern observed on the metaphyseal side [33].

1.4 Clinical Relevance

1.4.1 Osteoarthritis

Worldwide, more than 500 million people are affected by osteoarthritis (OA), making it the most common joint disease [4]. This number continues to rise over the years due to obesity, aging, and surgical joint treatments [6]. Its main symptoms include pain, loss of function, and disability, accompanied by joint changes such as articular cartilage degeneration, synotivis, and architectural changes in subchondral bone [5, 6, 7]. Some studies have demonstrated that osteoarthritis impacts the entire joint including its cartilage, synovium, subchondral bone, and associated muscles [42, 43]. Figure 1.23 illustrates the effect of the osteoarthritis on the joint. The degradative processes of this disease can lead to a complete destruction of the articular cartilage as well as other joint tissues [44, 45].

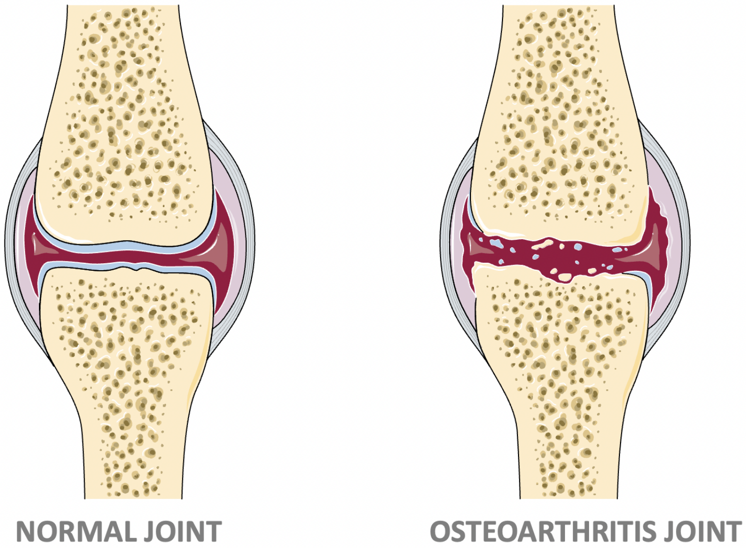

Figure 1.23: Illustration of structural changes in the joint due to osteoarthritis. Adapted from [11].

The advancement of osteoarthritis disease leads to an increase in the thickness of the calcified cartilage. In the last stages of osteoarthritis, this thickness decreases, which reflects the active remodeling action of this disease. Additionally, the chondrocyte density decreases, which is attributed to factors such as apoptosis, autophagy, and chronic inflammation [5]. Ultimately, these changes lead to the breakdown of cartilage in advanced osteoarthritis [6].

Under ordinary physiological conditions, the subchondral bone maintains a well-established balance between bone formation by osteoblasts and bone degradation by osteoclasts. However, osteoarthritis will disrupt this equilibrium, inducing structural changes in the subchondral bone. In the subchondral bone plate, significant morphological changes occur during the progression of the disease. More specifically, bone loss is observed in the first stages, followed by an expansion of the trabecular thickness. This results in an increase in thickness and porosity, accompanied by a reduction of the mineralization and of the trabecular integrity. Moreover, the subchondral bone is resorbed, the remodeling rate is increased, and the thickness of the subchondral bone is decreased. In the last stages, cancellous bone collapses and the resorption of bone is decreased while bone formation is increased. Microcracks are present in the young joint subchondral bone whereas their prevalence in the old joint is more concentrated near the tidemark [5].

In the first stages of osteoarthritis, subchondral bone marrow lesions could be observed. The screening of these types of lesions could be helpful in diagnosing earlier this disease. Another important pathological feature to diagnose osteoarthritis is the subchondral bone remodeling, which disrupts the osteochondral unit integrity and increases the interaction between cartilage and subchondral bone [6]. Detecting these lesions and changes in bone can help in the early diagnosis of osteoarthritis, potentially allowing for interventions to prevent further progression of the disease.

So far, no treatment is available to cure this disease, neither to stop the structural deterioration of cartilage and bone nor to reverse the existing damages. The only way to alleviate the patient's pain is to give medication or, when the disease has progressed too far, a total replacement of the joint. A better understanding of the joint changes due to this disease is therefore essential to find a suitable treatment and avoid total joint replacement.

1.4.2 Growth plate fusion

The growth plate ossification process is achieved through endochondral ossification, i.e. when the cartilage is gradually replaced by bone. The formation of cartilage within the growth plate, named as chondrogenesis, is regulated by numerous molecular signals acting both systemically and locally where it is needed. As the bone matures, the growth plate undergoes ossification, guided by the formation of struts that connect the bony parts on either side of the growth plate. Once these bridges are established, bone development ceases completely. Estrogen plays a crucial role in this process, facilitating the closure of the growth plates during puberty. This type of fusion, while observed in humans, does not occur in rats.

When estrogen is deficient, the growth plate does not undergo ossification, allowing growth to continue. This type of deficiency is mainly associated with two main genetic mutations, i.e. in the estrogen-receptor gene and in the CYP19 gene [46, 47, 48]. Additionally, certain types of chronic disease, including inflammation, uremia, and protein deficiency, can also involve imbalances in growth plate chondrogenesis [49].

Recently, there has been a notable increase in growth plate injuries, largely due to the higher participation of young people in sports and complex physical activities [50]. The growth plate is particularly susceptible to injury because it remains relatively weak until it ossifies completely during puberty [51]. These injuries can lead to microtrauma and, in severe cases, affect the normal growth process [52, 53, 54].

When the growth plate sustains physical injuries, the process of ossification by bridge formation is also present. However, a deep understanding of the formation process is still challenging due to the limitations of visualization methods of the growth plate. Investigating the morphology of the growth plate can provide valuable insights into the stresses induced in it, thus predicting the likelihood of bone fusion [55].

1.5 Animal Models

Animal utilization in medical science provides a huge advancement in medical knowledge and treatment alternatives for both human and animal diseases [56]. Nowadays, animal models used in the biomedical area are mainly rats and mice [57]. These models have led to significant progress in the comprehension of physiological and pathophysiological processes, as well as in testing potential treatment alternatives. They offer various similarities regarding to humans in terms of physiology, pathology, and anatomy, making them valuable tools to learn about disease mechanisms.

The choice of rat models has its limitations. Since rats are bipeds, they have different hopping and walking patterns compared to humans. Consequently, they don't have exactly the same biomechanics as humans [58]. Moreover, cartilage loading in the knee joint in rats and in humans is disparate since their biomechanics are remarkably different [59]. However, those limitations are overcome in this work since the rat walking pattern is considered, not the human one. Moreover, the anatomy of the knee joint in humans is much more complex and thicker to support heavier loads. This could influence the interpretability of findings from rats to human studies, especially in orthopaedic areas where joint behavior is crucial. More general drawbacks of animal models are the variability in the way animals are selected for randomization, the selection of some disease outcomes which could be irrelevant to the human clinical condition, and discrepancies in duration before the determination of disease outcomes which should not correspond to disease latency in humans [57]. These limitations emphasize the importance of animal model selection depending on the specific biomedical application.

Nevertheless, considering rats as animal models is also a very good choice for several reasons. Rats models are usually selected in medical research for several motives, including their ease of breeding and handling, minimal care requirements, cost-effectiveness, and genetic similarities to humans. Their small size also enables the use of extremely precise machines, which would be impossible to use on humans. In orthopaedic researches, rats offer advantages such as having softer tissues around their bones, making it easier to replicate risk factors of non-unions, which are relevant to human pathology. Additionally, their bones are subjected to different fracture patterns [58]. Rats exhibit similar genetic pathways involved in osteoarthritis, allowing a natural disease without inducing it artificially [60]. Moreover, since the rats are all bred in the same way, their lifestyle is the same, facilitating more reproducible results. Rats are considered as old at 13 months old, facilitating rapid experimental comparisons between adult (3 months old) and old specimens. For all the above reasons, rat models are widespread used in medical researches.

1.6 Main aims of the master thesis

The main aim of the present thesis is to conduct an in-depth analysis of the aging impact on the microstructure-related mechanics of the proximal tibia and to correlate these changes in microstructure with those observed in the distal tibia. This principal objective can be delineated into two main segments.

The first segment involves investigating the mechanics of the proximal tibia through finite element simulations aimed at replicating the application of a force on the upper part of the tibia. To accurately replicate the natural application of force, the force application surfaces were designed as ellipses, as to faithfully mirroring the contact surface between the tibia and the femur. By comparing old and young tibia samples, this study aims to elucidate the aging impact on the mechanics of bone, specifically examining the extent to which aging affects the load transfer between cartilage and bone. This analysis is expected to investigate the impact of the presence or absence of the growth plate, using different values of Young's modulus, on the mechanical behavior of the proximal tibia. Additionally, a segmentation between the subchondral and metaphyseal parts, while distinguishing the cortical bone from the trabecular bone, seeks to provide insights into the impact of the type of bone and its associated geometry on mechanical behavior. This segmentation aims to elucidate the contribution of each part of the studied bone to the overall mechanical behavior of the tibia.

The second main segment aims to analyze the mechanics of the bone as a whole by applying a quasi-static compression test to lower limb and tibia samples from both young and old rats. One of the main aims is therefore to compare the results obtained through finite element analysis with experimental tests carried out in the laboratory. Although the latter only provide an overview of the bone mechanics, they serve as a crucial validation for the computational μ-finite element simulations.

In conclusion, the research question that this present thesis attempts to answer is how aging impacts the mechanics of the proximal tibia in rats, examining these effects at both microscopic and macroscopic scales.

Chapter 2

Materials and Methods

This chapter will introduce all the steps involved in the materials and methods part of the present work. The primary objective of this master thesis is to characterize the relationship between the microstructure and micromechanical behavior of proximal tibia in aging rats. The existing study encompasses both experimental and computational parts, each with distinct methodologies and procedures.

In the computational part, meticulous attention was given to sample selection and preparation to guarantee consistent and reproducible micro-CT images. Detailed parameters used by the micro-CT were specified. After the image acquisition, a whole series of image processing steps was undertaken to ensure consistent alignment across all samples. In addition, segmentation between metaphyseal and epiphysial parts was carried out to delineate the two regions of interest within our model. A segmentation of the growth plate connecting both regions was also conducted by Laura Müller. The finite element analysis was then described step by step, starting from the selection of relevant images to the visualization of results.

In the experimental part, the selection and preparation of the samples is described step by step. The positioning and alignment of the samples in the compressor have been meticulously described to ensure greater reproducibility of results. Finally, the loading conditions are thoroughly elucidated.

Finally, this chapter explains the statistical analyses carried out in this work to ensure the significance of the obtained results.

In conclusion, this chapter will provide a comprehensive overview of the materials and methods employed in the present study, which is crucial for the latter comparison between microstructure and micromechanical behavior of the proximal tibia in aging rats.

2.1 Computational Part

2.1.1 Sample Selection

For the computational segment, a total of 12 samples were collected from 3-month-old (n = 6) and 13-month-old (n = 6) Wistar rats. Those specimens were collected at the CHU (Hospital University Center) of Liege. Additional information about their birth date, dissection date, and mass are provided in Table 2.1. Rats used in the computational part were only designated for this matter and had not undergone other prior experiences. Ethical approval for all experiments was obtained from an ethics committee.

Sample Name	Sex	Birth Date	Dissection Date	Age in month	Mass in grams
1D	Male	20/09/2021	22/12/2021	3	490
2D	Male	20/09/2021	22/12/2021	3	410
11D	Male	15/02/2022	18/05/2022	3	470
12D	Male	15/02/2022	18/05/2022	3	470
14D	Male	02/03/2022	08/06/2022	3	445
15D	Male	02/03/2022	08/06/2022	3	498
1VD	Male	10/11/2020	22/12/2021	13	780
2VD	Male	10/11/2020	22/12/2021	13	600
4VD	Male	24/04/2021	18/05/2022	13	625
7VD	Male	24/04/2021	08/06/2022	13	640
8VD	Male	17/04/2021	07/09/2022	16	605
11VD	Male	20/09/2021	09/02/2023	16	810

Table 2.1: Characteristics on the different samples used in the computational part where 'D' refers to the right leg and 'V' denotes old samples.

2.1.2 Sample Preparation

For the computational part, the dissection process was conducted by Juliette Maroquin and Laura Müller. Only the right tibia samples were extracted. The entire rat's lower limb was removed immediately after euthanasia, ensuring careful removal of the femoral head from its cavity, taking care not to damage it. Subsequently, lower limbs were immersed in a solution composed of 70% ethanol. The next day, the surrounding soft tissues were removed and the femur and tibia of the lower limb were separated. To guarantee complete preservation of bone properties and prevent microcracks, extracted samples were immersed in a 70% ethanol solution at ambient temperature. These steps are illustrated in Figure 2.1.

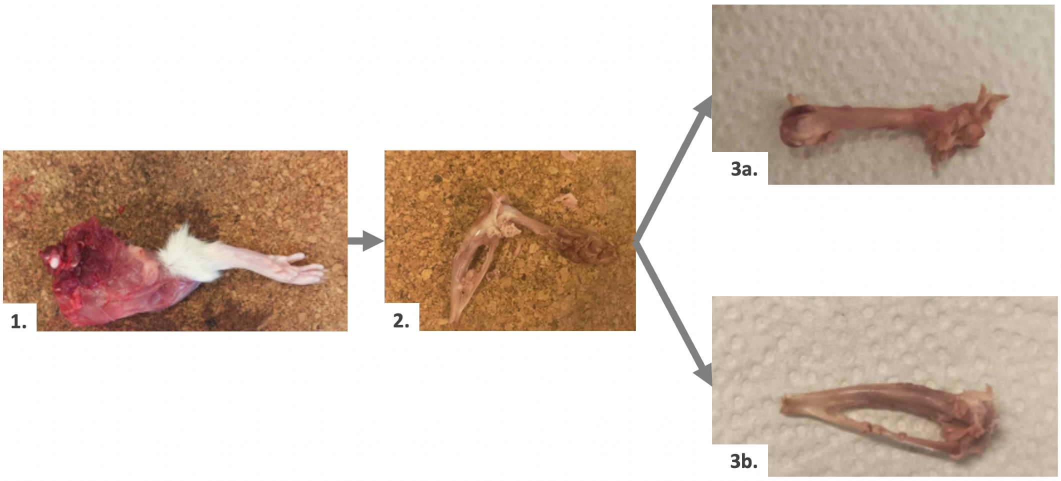

Figure 2.1: Illustration of the sample preparation process of the experimental part. (1) Extracted right leg of the rat. (2) Right leg without soft tissues. (3a) Femur without soft tissues. (3b) Tibia without soft tissues. Adapted from [61].

2.1.3 Image Processing

After dissection, all the samples were scanned using a micro-Computed Tomography (micro-CT) scanner. The scanning process takes place in the Catholic University of Leuven (KUL) with the Skyscan 1272 micro-CT scanner, manufactured by Bruker company (Belgium). Parameter settings were kept consistent across all samples. To enhance the distinction between the sample and its environment, surrounding air was removed during scanning [62]. The scanning was conducted at a voltage of 90 kV and a current of 110 μA, utilizing aluminium and copper filters with thicknesses of 0.5 mm and 0.038 mm, respectively. Throughout the scanning process, all the samples were rotated through 180° in 0.4° increments, resulting in 450 projections. The exposure time was imposed to 1470 ms, with each frame averaged four times. Thanks to all those imposed parameters, a scan resolution of 10 μm could be achieved.

Following those acquisitions, several image-processing steps had to be carried out to facilitate the comparison of all 3D bone reconstructions. To this end, the samples were aligned in the same way, using a reference sample as a template, i.e. the 1D sample. This reference bone was aligned based on the principal axis of the metaphyseal region of the bone. To enable the comparison between the metaphyseal part and the subchondral part of the bone, masks were created to delineate and segment them.

2.1.3.1 Micro-CT Scanner Parameters

2.1.3.2 Pre-Processing

To remove the unwanted noise, while maintaining a clear contrast between bone and background, a Gaussian blur filter (applied in 3D space, with a square kernel and a radius of 1.2 pixels) was applied to the stack of images, using the CTAn software (v1.19.4.0, Skyscan). Then, a binarization has been made using the automatic Otsu's method in 3D space. This image thresholding method relies on the minimization of the intra-class intensity variance [63].

The following step is based on removing the fibula. Indeed, when scanned, the lower limbs of rats encompass the tibia and fibula, which is the bone directly linked to the tibia and located laterally behind it. If no connection between both bones was recorded, an automatic segmentation, using the despeckle function of CTAn software, was performed to remove the fibular areas. Conversely, if there is a mineralized connection between the bones was observed, the segmentation step was performed manually to extract exclusively the tibia area.

2.1.3.3 Bone Alignment

The subsequent step involves the alignment of a first reference bone, which will serve as a basis for the other sample's alignment. To this end, the last 300 slices of the distal part of the bone were kept to align this section of the sample with its principal axis of inertia using the BoneJ module (v.1.4.3) on the ImageJ software (v.1.52a). This part corresponds to the diaphysis area, which could be considered as a cylinder. Using this axis, a rotation matrix was generated and saved in Avizo software (v.9.2.0, ThermoFisher Scientific) to rotate the whole bone.

Subsequent bones could be aligned with the first in the Avizo software. Finally, the distal part of the sample was cut perpendicularly to the longitudinal axis, ensuring that only 1106 slices per bone remained. This main step ensured a constant orientation with samples of the same length for further analysis.

2.1.3.4 Metaphysis and Epiphysis Segmentation

The aim of this study is to compare several bone regions to compare their microstructures and mechanics. To achieve this, masks must be made to delimit the zones of interest. In this work, the focus is on the delimitation of the metaphyseal and epiphyseal parts of the bone, as well as the growth plate.

Initially, the CTAn segmentation tool was used to delimit the epiphysis part from the metaphysis part of the bone. This segmentation was carried out manually, following the growth plate in the bone's sagittal plane. To mitigate potential errors arising from manual segmentation, a 3D dilation (round, 1 pixel) was imposed on all regions of interest. This step is clearly illustrated in Figure 2.2.

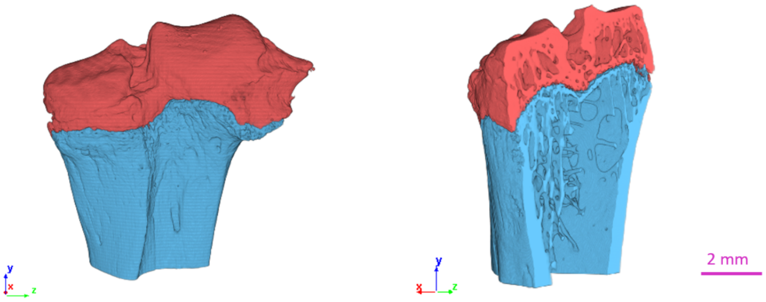

Figure 2.2: Illustration of the segmentation process between subchondral (depicted in red) and metaphysis (depicted in blue) on the 11VD sample. Scale bar = 2 mm [61].

All the aforementioned steps were conducted by Laura Müller and Juliette Maroquin, with the aim of studying microstructural changes in bone. The results obtained from their work will be used for comparison with my own findings.

2.1.4 Finite Element Analysis

The main purpose of the computational part is to extract essential characteristics of bone under consistent loading conditions, by analyzing their distribution within the studied bone. In pursuit of this objective, distinct bone parts were extracted to determine their respective contributions to the overall mechanics of bone. As previously stated, long bone is made up of two distinct types of bone, i.e. trabecular bone and cortical bone, each displaying unique structural properties. Moreover, those long bones also encompass distinct regions, including the metaphyseal and the epiphyseal areas. This study will focus on these anatomical segments of the bone while investigating the impact of bone types within each. This work will therefore ensure a comparative evaluation of the distribution of strains in the trabecular bone in the metaphyseal part, cortical bone in the metaphyseal part, trabecular bone in the subchondral part, and finally cortical bone in the subchondral part. Those four areas are depicted in Figure 2.3. The impact of the presence or absence of a growth plate between the subchondral and metaphyseal parts was also studied. To achieve this, a mask was created to perfectly fill the area between the subchondral bone and the metaphyseal bone, ensuring that the growth plate formed a non-porous entity between them. An illustration of this mask is depicted in Figure 2.4. All the above-mentioned steps are illustrated in Figure 2.5.

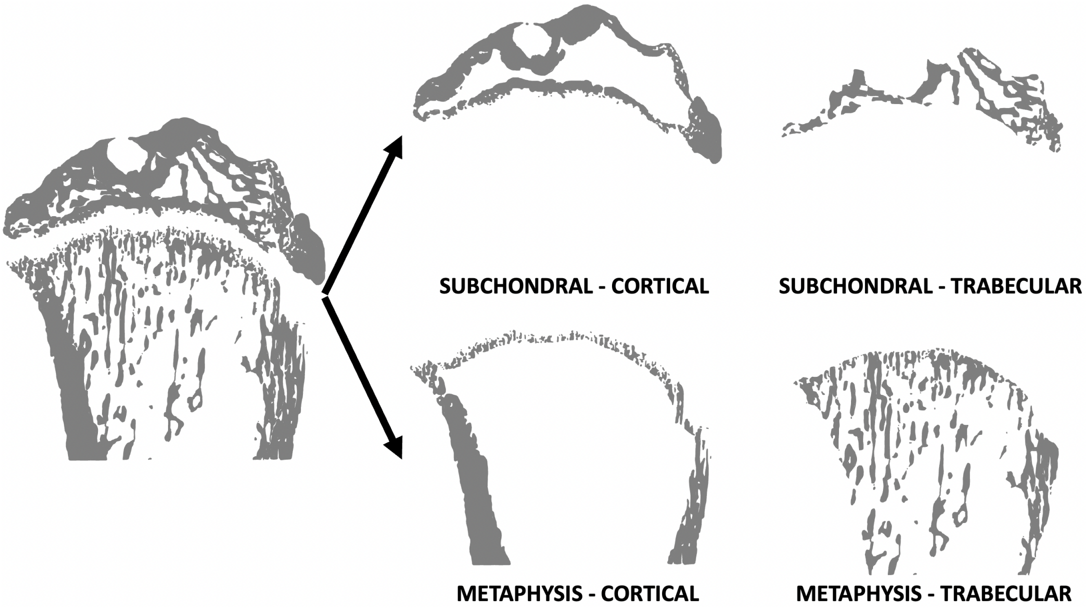

Figure 2.3: Illustration of the four different studied areas of the bone, i.e. the subchondral and the metaphyseal part of the bone with a distinction between cortical and trabecular bone.

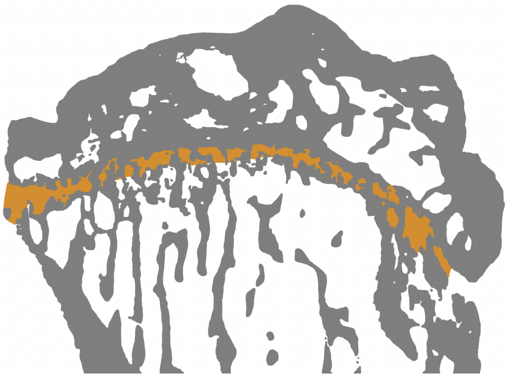

Figure 2.4: Illustration of the mask of the bone in grey and of the growth plate in orange.

Figure 2.6 illustrates the overall procedures involved within the Finite Element Analysis (FEA) part, showing the software used at each stage. The subsequent sections explain these steps in greater detail.

2.1.4.1 Image Selection

The first step of the finite element analysis involved the selection of images of interest using *ImageJ* software. In this software, the images, primarily in the sagittal plane, were initially resliced from the top to procure a transversal cut of the bone. Subsequently, to limit the analysis to the medullary cavity, the image dataset was cut to 600 slices. This reduction was achieved by first identifying the upper part of the bone and retaining the following 600 slices. Given the scan resolution of 10 μm, this corresponds to an effective height of 6 mm. After this selection process, the images were subjected to a median filter, named as ‘Despeckle’, which substituted each pixel with its median value in its 3 x 3 neighborhood. This filter removed all extraneous noise present in the bone, particularly the trabeculae that had been cut and were therefore not connected to the bone due to image selection.

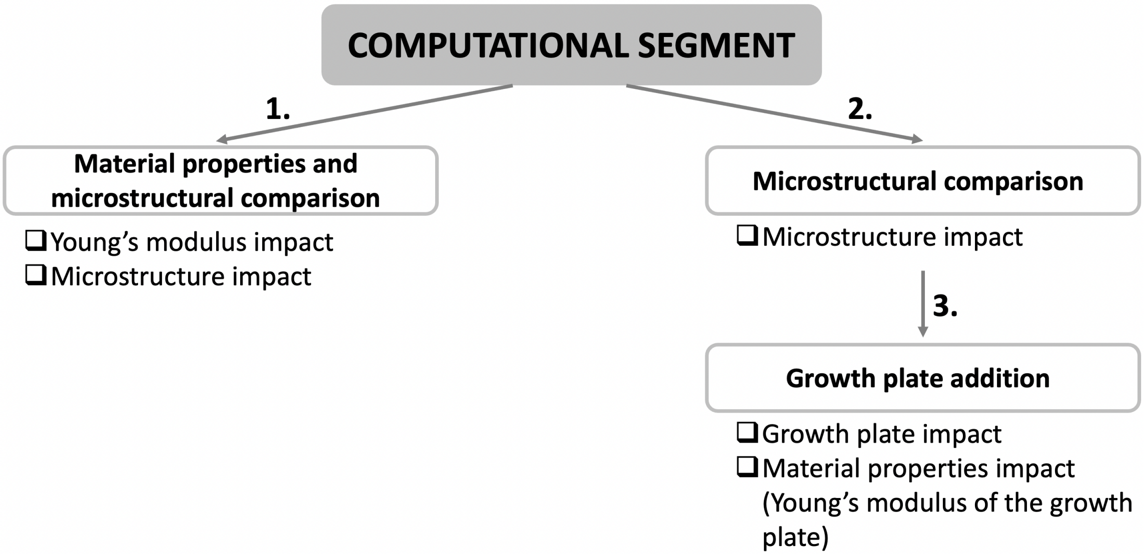

Figure 2.5: Illustration of all the steps performed in the computational part.

2.1.4.2 Masks extraction

The subsequent step was to create the masks used in the comparison of the distinct parts of the bone. A mask shows only the desired part of the bone, i.e. the subchondral or metaphyseal part with trabecular or cortical bone. Only this part will therefore be illustrated in this mask, as shown in Figure 2.3. *Materialise Mimics* 24.0 first reconstructs a 3D model from the stack of '.bmp' images obtained in the previous step.

Initially, the resolution was set to 10 μm, corresponding to the resolution of the micro-CT. Subsequently, a new mask was created using the predefined threshold named as 'Bone (CT)'. This type of threshold is the most appropriate to apply for bone, so as not to lose any information or bone parts. This thresholding method is used to impose the range of pixel values that will be included when the mask is created, i.e. from 226 to 1634 for this thresholding method. For all masks created, the option 'Keep largest' was selected to retain only the adjacent voxels within the newly defined region of interest (ROI). This choice was made because image processing had been carried out beforehand. The subsequent step was to calculate the three-dimensional object from the mask that had just been formed. This step is crucial to perform the transformation from 2D to 3D models. Optimum quality settings were chosen to ensure the most accurate results achievable. This technique will also apply some optimization to the calculated part, i.e. triangle reduction and smoothing. Finally, a *Python* script was executed on *Mimics* to export the mask as a matrix ('.mat' file) that could be read by the *Matlab R2019b* software for further analysis [64].

Once the mask has been saved in matrix format, it is imported into the *Matlab R2019b* software. It is in this program that the mesh, material properties, and boundary conditions are defined.

2.1.4.3 Mesh and material assignment

To avoid an overly complex model, the entire bone was imposed as being a homogeneous, elastic, and isotropic material in *Matlab R2019b*. To this end, a Young's modulus was assigned to the entire bone, as well as a Poisson's ratio of 0.3. The Young's modulus (E) was computed

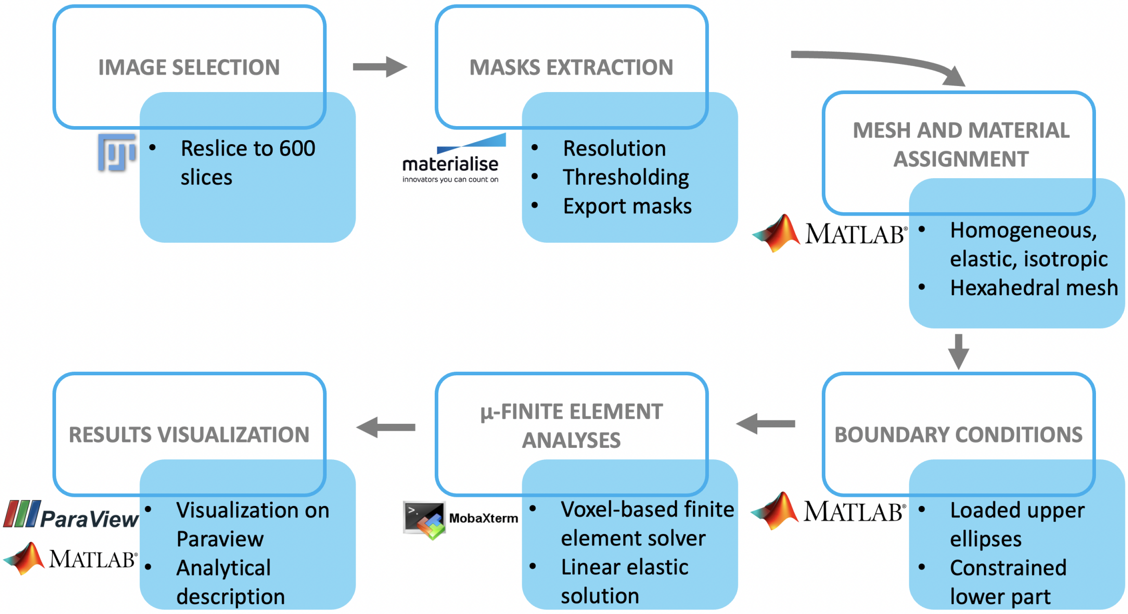

Figure 2.6: Illustration of the different steps involved in the finite element analysis.

using nanoindentation, carried out by Laura Müller, on both old and young bones. A total of 100 indents were created in both sample types, organized in a 10×10 grid. A Berkovitch tip of 50 nm radius was used for the indentation process. Each indentation was carried out with a controlled penetration depth of 150 nm, and a lateral spacing of 1.5 μm to ensure independent measurements. Using this technique, a statistically significant difference in Young's modulus values for old and young bones has been found, i.e. 25.5325 GPa for young bones and 29.5559 GPa for old bones (refer to the nanoindentation grids in Appendix A), making mandatory the assignment of different Young's moduli to these age groups. This difference corresponds to a 14% variation between the two, which is not negligible.

An in-depth analysis of the four studied areas was conducted using two different Young's modulus values. This analysis allowed for a comprehensive assessment of the bone's material properties in relation to its age and microstructure. However, assigning two different Young's moduli as a function of bone age does not distinguish the contributions of bone microstructure from those of material properties. To isolate the influence of bone microstructure alone, a constant value of Young's modulus of 25.5325 GPa was also assigned to old bone. This approach allows the contribution of a single parameter to be isolated.

Regarding the Young's modulus of the growth plate, values of 5, 50 and 500 MPa were assigned to assess the impact of Young's modulus value on the micromechanical behavior of the bone. The values 5 and 50 MPa were chosen to represent the lower and upper limits of the physiological Young's modulus of the growth plate, as measured in previous experiments [65, 66, 67, 68, 69, 70]. The value of 500 MPa was selected to simulate a pathological condition characterized by growth plate degeneration and mineralization. In this scenario, the growth plate closes, leading to a significant increase in Young's modulus. While this condition is not observed in rats, it is prevalent in humans with certain bone diseases.

The mesh was defined using a custom function implemented in *Matlab R2019b* as illustrated in Figure 2.6. This function defines hexahedral meshing elements with each face length measuring 10 μm, corresponding to the resolution of the micro-CT. The *Matlab* script converts each voxel from the micro-CT into an eight-noded hexahedral element, maintaining the exact geometry of bone during simulation. This type of mesh is of paramount importance to avoid losing the bone's shape, as it is invaluable for comparing its microstructure. As a result, the size of the mesh remains uniform across all bones studied, with only the number of elements varying between 69 208 152 and 89 210 904, depending on the size of the bone present in the mask. An illustration of the mesh structure is depicted in Figure 2.7. This code has been provided by the KUL university and adapted to my case by myself.

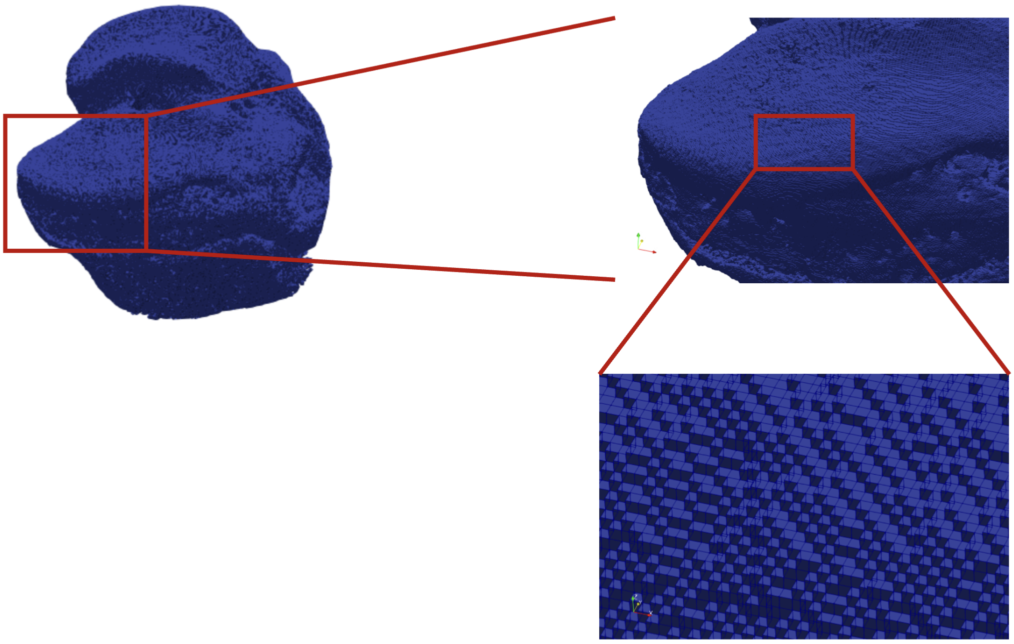

Figure 2.7: Illustration of the mesh in the 11D sample at three different levels.

Given the direct relationship between the mesh and the resolution of the micro-CT, a mesh sensitivity analysis does not need to be performed. In addition, several studies have shown that if the number of elements present to represent the mean trabecular thickness is at least 4, the numerical convergence of this kind of model is ensured [71, 72]. The thickness of the trabeculae of young bones ranges between 70 to 90 μm and is around 120 μm for old bone [61]. Since the resolution of the micro-CT is 10 μm, there are indeed on average more than 4 elements per trabecula, ensuring the numerical convergence of the models.

2.1.4.4 Boundary conditions

The determination of the boundary conditions involved the definition of the contact surface between the tibia and the femur in *Matlab*. Drawing on various articles that have examined this contact surface between the femur and the tibia [73, 74, 75, 76, 77, 78, 79], it appears that the geometry closest to represent this contact surface is an ellipse, more specifically two ellipses (one for each plateau). The area of each ellipse was kept constant, with only the center of the ellipse adjusted depending on the studied bone. The characteristics of these ellipses are detailed in Table 2.2. These two ellipses were therefore located at the internal centre of each plateau, as depicted in Figure 2.8.

A constant force of 40 N was applied in the z-direction to these two ellipses. This force magnitude was chosen to exert a force that is approximately 10 times greater than the total weight

	Medial plateau	Lateral plateau
Half-small axis	98	150
Half-big axis	112	175

Table 2.2: Characteristics of the two ellipses constructed, mimicking the contact surface between the tibia and the femur.

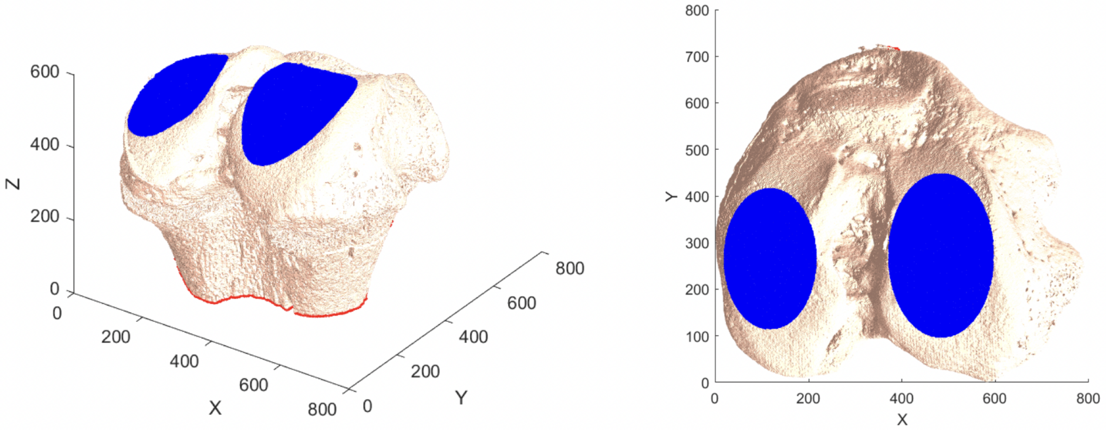

Figure 2.8: Illustration of the position of the two ellipses on each tibial plate for the bone referred to as 14D with the three axes in pixels. The two plateaus are depicted in blue and the constrained plate is depicted in red.

of the rat. Several previous studies have applied similar forces to the rat tibia to observe deformations and reactions in the studied bone [74, 80, 81, 82]. However, since the solver employed in this study solves the system under linear elastic assumptions, the specific value of the force applied does not cause major changes in the behavior of the bone mechanics. Only a multiplication factor is needed to scale the force accordingly.

A rigid displacement of elements of interest can be applied under the initial conditions, to obtain a total force of 40 N. Therefore, the displacement required to obtain a total force of 40 N on the two plates had to be calculated. The box plot representing the total displacement required for each bone to obtain this constant force is shown in Figure 2.9, varying from one bone to the other as their microstructure and material properties change. All the individual values can be visualized in Appendix B.1. At the opposing end, the bottom surface was fully constrained in all directions (x, y and z) to prevent any undesirable displacement at this end. This condition was chosen to mimic as closely as possible the experimental conditions described in the following sections.

The applied displacement for the young bones to achieve a final applied force of 40 N is higher due to their lower Young's modulus (see Appendix B.1). Also, the influence of the mechanical structure on the resulting force explains the higher displacement.

Figure 2.10 depicts the applied displacement while adding a layer of growth plate between the metaphyseal and subchondral regions of the bone, varying the Young's modulus of the growth plate. Generally, the applied displacement decreases as the Young's modulus of the growth plate increases. This phenomenon derives from the increased stiffness of the overall tissue while adding a growth plate, necessitating a smaller displacement to achieve a force of 40 N. Notably, this reduction is more pronounced in the young bone sample compared to the old bone

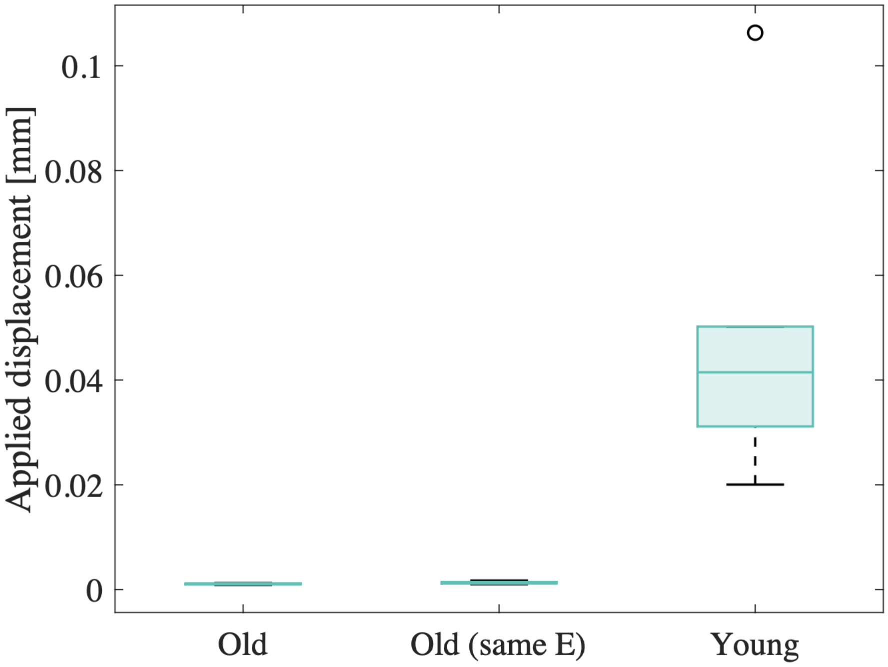

Figure 2.9: Imposed displacements to ensure a constant 40 N total force on the two plateaus.

sample. All the individual values can be found in Appendix B.2.

Following these procedures, a '.h5' file is created, containing all the information required for the simulation. This file format was chosen due to its hierarchical data storage capability and its ability to handle extensive data volumes, which is very important in our case because of the large number of elements to keep the exact same geometry of the bone.

The process of determining boundary conditions spans between 7 and 17 hours in total.

2.1.4.5 μ-Finite Element Analyses

By applying an external constant load to the chosen boundary conditions, some stresses and strains are induced inside the studied bones. Several crucial factors influence the amplitudes and directions of these internal forces and deformations, including the loading conditions, the internal architecture of the bone, and the imposed material properties. To illustrate the transmission of forces from the applied load to the interior of the bone, the boundary-value problem was formulated. This boundary-value problem is formed by a set of partial differential equations that perfectly describe the internal force distributions inside the bone following the application of an external load [83, 84, 85].

This elastic problem considers a three-dimensional body composed of a volume, V, delineated by a surface, S, within a chosen coordinate system x_i composed of three main axes ($i = 1, 2, 3$). The applied external forces are represented by f_P for point loads, f_S for surface loads, and f_V for volume loads.

By applying constant load at the boundary conditions, the bone will deform. This deformation is illustrated by the strain tensor ϵ,

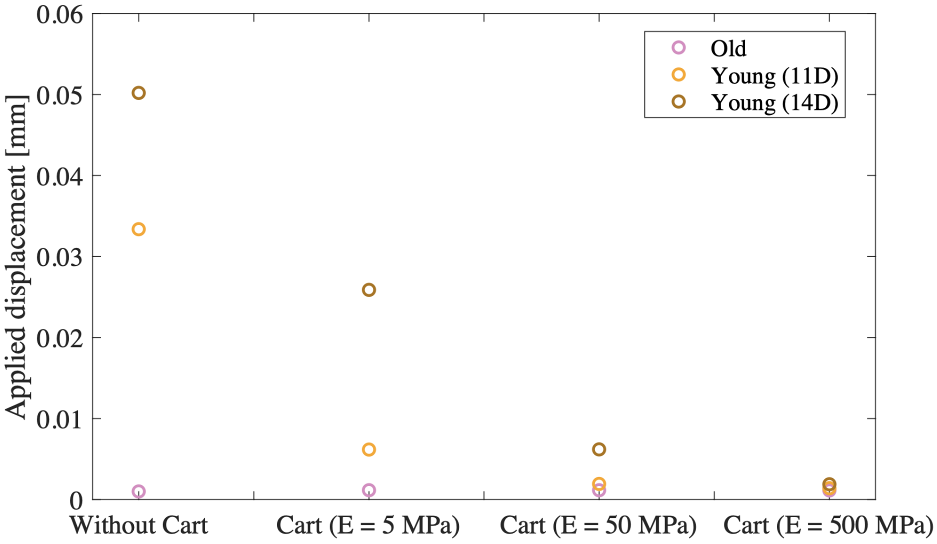

Figure 2.10: Imposed displacement to ensure a constant 40 N total force while adding a growth plate while varying its Young's modulus between 5 and 500 MPa.

$$\epsilon_{ij} = \frac{1}{2}\left[\frac{\partial u_i}{\partial x_j} + \frac{\partial u_j}{\partial x_i}\right], \tag{2.1.1}$$

which is obtained thanks to the differentiation of the displacement vector $u(x)$. This equation is valid only under the small strain assumption. On one hand, the strain tensor elements for $i = j$ constitute the deformation along the three principal coordinate directions. On the other hand, the strain tensor elements for $i \neq j$ represent the angular variations between two surfaces relative to the coordinate system orientation.

Similarly, the stress-strain relationship,

$$\sigma_{ij} = C_{ijkl}\epsilon_{lk}, \tag{2.1.2}$$

could be established under the linear elastic behavior of the bone assumption, where σ_{ij} represents the stress tensor and C_{ijkl} is the elasticity tensor. The stress tensor elements for $i = j$ constitute the force normalized by the corresponding area along the three principal directions of the coordinate system and perpendicular to an infinitesimal area. On the other hand, the stress tensor elements for $i \neq j$ illustrate the force normalized by the corresponding area along the three main axes of the coordinate system and parallel to an infinitesimal area.

Under an isotropic material behavior assumption, two independent material properties are needed to establish the material mechanical behavior. Under this assumption, the stiffness matrix, C,

$$C = \frac{E}{(1+\nu)(1-2\nu)} \begin{bmatrix} 1-\nu & \nu & \nu & 0 & 0 & 0 \\ \nu & 1-\nu & \nu & 0 & 0 & 0 \\ \nu & \nu & 1-\nu & 0 & 0 & 0 \\ 0 & 0 & 0 & \frac{1}{2}-\nu & 0 & 0 \\ 0 & 0 & 0 & 0 & \frac{1}{2}-\nu & 0 \\ 0 & 0 & 0 & 0 & 0 & \frac{1}{2}-\nu \end{bmatrix}, \tag{2.1.3}$$

is formed, where E stands for the Young's modulus of the bone and ν, its Poisson's ratio.

The relationship between the stress and strain tensors can only be solved under two constraints. The first constraint,

$$\frac{\partial \sigma_{ij}}{\partial x_j} = 0 \text{ in } V, \tag{2.1.4}$$

is the condition of equilibrium of the stress tensor which assumes that the volume loads (f_V) are null.

The second constraint that must be satisfied,

$$\frac{\partial^2 \epsilon_{ij}}{\partial x_k \partial x_l} + \frac{\partial^2 \epsilon_{kl}}{\partial x_i \partial x_j} - \frac{\partial^2 \epsilon_{ik}}{\partial x_j \partial x_l} - \frac{\partial^2 \epsilon_{jl}}{\partial x_i \partial x_k} = 0 \; i,j,k,l = 1,2,3 \;, \tag{2.1.5}$$

is the compatibility relation which ensures the existence of a continuous displacement field.

The stress-strain relationship equation can be combined with these two constraint equations to obtain the final displacement field inside the three-dimensional bone,

$$(\lambda + \mu)\frac{\partial}{\partial x_i}\left(\frac{\partial u_k}{\partial x_k}\right) + \mu \frac{\partial^2 u_i}{\partial x_j^2} = 0, \tag{2.1.6}$$

where $\lambda = \frac{E\nu}{(1+\nu)(1-2\nu)}$ and $\mu = \frac{E}{2(1+\nu)}$ are the Lamè coefficients.

Due to the complex bone geometry, loading conditions, and imposed material properties, analytical solutions are impracticable, leading to the usage of numerical resolutions. Boundary value problems are mostly solved by Finite Element Analysis (FEA). This technique employs the potential energy method or the principle of virtual work instead of directly discretizing the displacement field equation.

The potential energy method affirms that a mechanical system is in equilibrium when the total potential energy, Π, given by

$$\Pi = \frac{1}{2}\int_V \sigma \epsilon dV - \int_V u f_s dS - \sum_P u f_p, \tag{2.1.7}$$

is minimized. This total potential energy is acquired by summing the internal total strain energy of the system and the external forces work, W.

The finite element method leads to a discretization of the model into smaller, simple elements; in this case, hexahedral elements, connected with nodes located at each corner of the elements.

The discretization begins with the substitution of the continuum displacement vector, u, by the nodal displacements, U_N. The element displacements and strains,

$$U_M = S_M U_N, \tag{2.1.8}$$

$$\epsilon_M = B_M U_N, \tag{2.1.9}$$

can be found thanks to the nodal displacement and by bringing in the shape-function matrix S_M and the strain-displacement matrix B_M.

The relationship between the element strain ϵ_M and the element stress σ_M,

$$\sigma_M = D_M \epsilon_M, \tag{2.1.10}$$

is defined thanks to the introduction of a constitutive matrix D_M, which encompasses the element constitutive properties.

The nodal forces could be determined by transforming the element forces. Those nodal forces must satisfy the equilibrium equation which dictates that the boundary stresses and the loads applied on each element should be equal to the nodal forces. The total potential energy,

$$\Pi = \frac{1}{2} U^T K U - U^T F, \tag{2.1.11}$$

is expressed as a function of the global force vector F, the global displacement vector U, and the global stiffness matrix K.

To ensure the minimization of this expression, the condition

$$\frac{\partial \Pi}{\partial U_i} = \begin{bmatrix} \frac{\partial \Pi}{\partial U_1} \\ ... \\ \frac{\partial \Pi}{\partial U_1 N} \end{bmatrix} = 0, \ i = 1, ..., N, \tag{2.1.12}$$

is imposed, leading to the final system of N equations [83],

$$KU = F, \tag{2.1.13}$$

which entirely dictates the behavior of the induced internal forces within the bone.

In the present work, the *ParOSol* software was employed as a μ-finite element solver. This software enables the equation resolution by applying the aforementioned equations. Nevertheless, this software operates as a black box, meaning that only inputs and outputs can be viewed, without revealing intermediate resolutions.

2.1.4.5.1 Solver features

Due to the high number of elements involved in the simulations, they require the computational power of supercomputers to be executed efficiently. To ensure the convergence of our results, several parameters need to be defined. Firstly, the task is configured to use a single node, meaning that the computational process will be performed on a single machine, named as a node. Next, the number of tasks that will be executed is set to 36, which means that the main task will be divided into 36 sub-tasks. Next, the maximum memory that each task can use per computing unit (CPU) is set to $7,000$ MB. Finally, a level equal to 3 is defined to use a maximum of three multi-grid levels. A tolerance of 10^{-7} is imposed to achieve a relative residual of 10^{-7} [86].

Since all these operations require a large amount of memory, the system was solved using ParOSol on the *NIC5* cluster of the University of Liège.

The process of μ-finite element resolution spans between 15 minutes and 1 hour.

2.1.4.5.2 Output Exportation

The solver takes a '.h5' file as input and writes the results obtained to the same input file. ParOSol organizes the mesh and the solution in two different groups within the file.

On one hand, the *Mesh* group contains information regarding the coordinates of the vertices, the eight indices of each element, and the Young's modulus associated with each element [87].

On the other hand, the results obtained concerning the displacement at each node, the force at each node, the strain energy density at each element centre, the Von Mises stress at each element center, and the effective strain at each element center is stored in the *Solution* group [87].

2.1.4.6 Results visualization

In this study, the principal parameter which will be analyzed is the effective strain (EFF), since it is one of the most important properties for characterizing the mechanical behavior of bone. Indeed, it characterizes the way the studied species are deformed. The effective strain can be coupled to the strain energy density, U, via

$$\epsilon_{eff} = \sqrt{\frac{2U}{E}}, \tag{2.1.14}$$

where E represents the Young's modulus of the tissue [88].

Other properties such as strain energy density and Von Mises stresses obtained from the *Solution* group were not analyzed because they directly derive from this property, implying that their behavior will be similar to that of the effective strain.

Another significant property directly derived from the deformation measured in each element is the principal strain. This parameter indicates the maximum and minimum values of deformation that the sample can experience when subjected to an applied force. Understanding this property is fundamental for analyzing how the tissue stretches or compresses under loading conditions. Furthermore, evaluating this variable allows for predictions of material failure.

To calculate this principal strain, the deformation matrix,

$$\epsilon_{ij} \begin{bmatrix} \epsilon_{xx} & \epsilon_{xy} & \epsilon_{xz} \\ \epsilon_{xx} & \epsilon_{xy} & \epsilon_{xz} \\ \epsilon_{zx} & \epsilon_{zy} & \epsilon_{zz} \end{bmatrix}, \tag{2.1.15}$$

is first linearized,

$$\epsilon' \begin{bmatrix} \epsilon_1 & 0 & 0 \\ 0 & \epsilon_2 & 0 \\ 0 & 0 & \epsilon_3 \end{bmatrix}, \tag{2.1.16}$$

to obtain all the principal element strains on its diagonal, where ϵ_1, ϵ_2, and ϵ_3 are the principal strains of the element.

To determine the minimum and maximum principal element strains, one should examine the minimum and maximum values of this diagonal. If the value is negative, the element is under compression, whereas if the value is positive, the element is under tension [89, 90, 91].

Finally, the last important parameter analyzed was the apparent stiffness of each plateau,

$$S = \frac{F}{d}, \tag{2.1.17}$$

where F stands for the applied force in N and d in mm for the applied displacement. Apparent stiffness, measured in N/mm, indicates the extent to which a component can resist deformation when a force is applied. The greater the apparent stiffness, the higher the studied object's ability to withstand a large force without being significantly deformed. This property is very important, as it will allow to establish the impact of aging on the evolution of bone apparent stiffness. Moreover, a thorough understanding of the apparent stiffness of each plate is an important factor in the placement of a prosthesis implanted in bone, and particularly for its stability [92]. There is a significant distinction between the apparent stiffness calculated in this study, which derives directly from the bone's geometry and material properties, and Young's modulus, which is an intrinsic property of the material itself and remains unaffected by the bone's geometry.

The final solution can be visualized using a solver called *ParaView* as illustrated in Figure 2.6. This open-source visualization application provides a clear representation of the results directly on the bone being studied. This tool can be used to visualize the entire distribution of effective strains in the bone. Moreover, it can be used to virtually cut the bone to visualize the distribution of these effective strains within the bone. This type of visualization is particularly insightful for identifying the locations of strain concentration, which cannot be provided by a single histogram.

To analyse the results more analytically, *Matlab* scripts were implemented to generate histograms representing the distribution of effective strain in the different parts of the bone studied. These histograms are used to study the frequency distribution of the effective strains. All these curves are normalized to obtain an area under the curve worth 1, making it easier to compare the different samples and also the different parts of the studied bone. Given the large number of curves, certain parameters were studied to facilitate the reading of the distribution and easily compare the results. These parameters include the width, which gives indications regarding how heterogeneous the strain distribution is within the bone, and the average of the obtained results.

The width of the distribution is determined using the full width at half-maximum (FWHM) method, as shown in Figure 2.11. This metric measures the width of the distribution at half of its peak height.

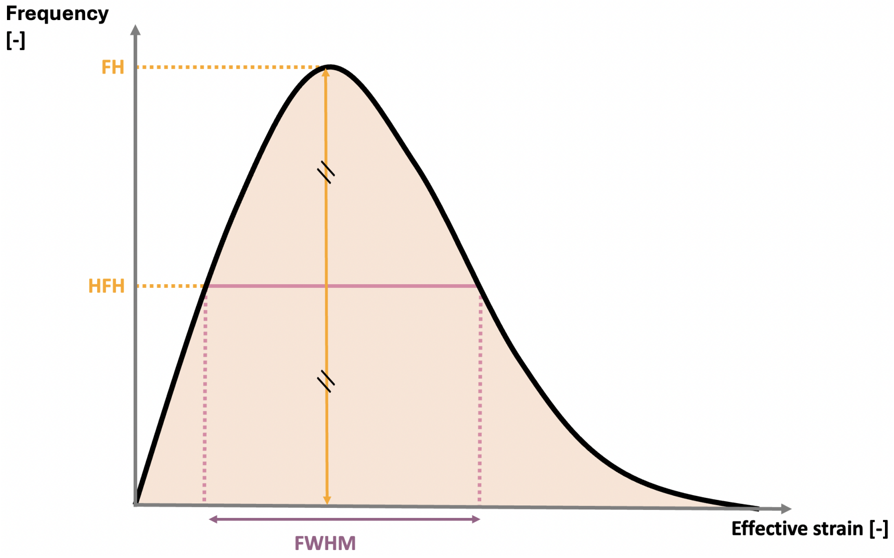

Figure 2.11: Illustration of the Full Width at Half-Maximum on a random distribution.

2.2 Experimental Part

2.2.1 Sample Selection

In the experimental part, a total of 14 samples were collected from 1-month-old Wistar-Kyoto rats (n = 4), 2-month-old Lewis rats (n = 3), and 3-month-old Lewis rats (n = 7). These two specimens were not chosen directly, but they are very similar. Those specimens were collected at the CHU of Liege (Hospital University Center). Additional information about their birth date, dissection date, and mass are provided in Tables 2.3. It is important to note that the rats used for the experimental part had already been employed in previous experiments, including no genetic variation. The Wistar-Kyoto rats had undergone tracheal ablation, while the Lewis rats had experienced brain death for approximately 6 consecutive hours. Ethical approval for all experiments was obtained from an ethics committee.

2.2.2 Sample Preparation

For the experimental part, a meticulous protocol has been developed for resin-coating rat lower limbs. Since these rats had undergone other experiments beforehand, leg extraction was not carried out directly after euthanasia. Nevertheless, it was consistently carried out on the same day or the rats were preserved in the freezer to prevent the degradation of mechanical properties of the tissues.

The lower limbs of rats were extracted in their entirety, ensuring careful removal of the femoral head from its cavity, taking care not to damage it. The samples were then immersed in a

Sample Name	Sex	Birth Date	Dissection Date	Age in month	Mass in grams
20D	M	10/11/2023	19/02/2024	3	305
20G	M	10/11/2023	19/02/2024	3	305
21D	M	15/11/2023	19/02/2024	3	310
21G	M	15/11/2023	19/02/2024	3	310
22D	M	22/12/2023	25/03/2024	3	316
22G	M	22/12/2023	25/03/2024	3	316
23D	M	22/12/2023	25/03/2024	3	305
1YD	M	15/03/2024	15/04/2024	1	300
1YG	M	15/03/2024	15/04/2024	1	300
2YD	M	20/03/2024	15/04/2024	1	299
2YG	M	20/03/2024	15/04/2024	1	299
24D	M	30/02/2024	30/04/2024	2	305
25D	M	01/03/2024	01/05/2024	2	302
26D	M	02/03/2024	01/05/2024	2	307

Table 2.3: Characteristics of the different samples used in the experimental part where ’D’ refers to the right leg, ’G’ refers to the left leg, ’Y’ denotes young samples, and ’M’ refers to males.

solution of PBS (Phosphate-Buffered Saline) to maintain a constant pH, osmolarity, and ion concentration mimicking those present in the original body. Samples were then embedded in the resin on the same day.

In this experimental section, two types of experiments were conducted. The first involved the extraction of the entire leg to account for the mechanics of the knee in situ. The second focused only on the compression of the tibia itself to isolate and analyze its mechanical behavior, thereby aligning with the computational experiments performed in the present work. These two types of experiments are shown in Figure 2.12.

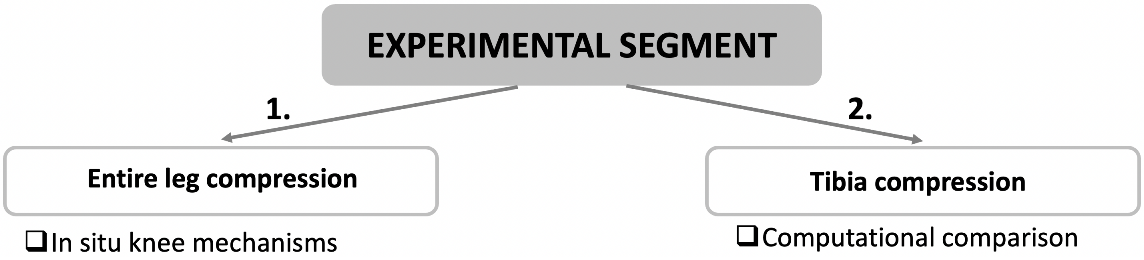

Figure 2.12: Illustration of all the steps performed in the experimental part.

To prevent movement of bone fixed in resin-fixed through soft tissue, it had to be removed from the lower part of the leg, right up to the patellar tendon. Moreover, the soft tissues in the upper part of the leg were trimmed to refine the part of the leg close to the femur. This was done to avoid excessive artifacts due to the presence of abundant soft tissue and to make the handling easier. Once the bones were cleaned, they were embedded in resin. The resin used is *Technovit® 4071*. It was specifically chosen for its fast curing time, excellent grinding properties, and ease of processing. After mixing 8 g of powder with 5 g of liquid solution, the preparation is poured into a 10 mL falcon tube. The rat tibia is then inserted into the tube, down to the patellar tendon, and manually immobilized in the most reproducible and upright position possible for approximately 5 minutes. The final step was to cut the tube so that the total height of the sample did not exceed 4 cm. While this protocol was developed for this present work, it was also intended to establish a protocol applicable to another project, using machines unable to accommodate samples with a size greater than 4 cm. Finally, while awaiting the compression tests, the embedded samples were transferred back to a PBS solution and stored in the fridge to preserve the mechanical properties of the analyzed tissues. The resume of those steps is highlighted in Figure 2.13.

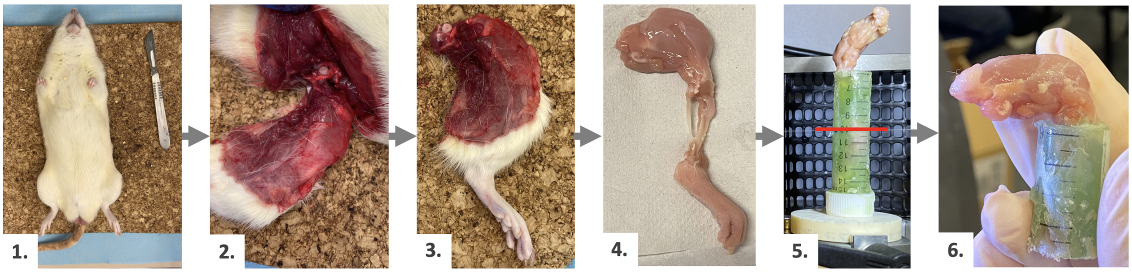

Figure 2.13: Illustration of the different steps involved in the resin embedding process of the experimental part. (1) Euthanized rat. (2,3) Extracted lower limb of rat. (4) Soft tissues around tibia removed. (5) Sample embedded in resin, with the red line highlighting location of the place to cut. (6) Final embedded sample.

For three samples, only the tibia was kept in its entirety. This was done to replicate as closely as possible the conditions simulated in the computational section. Similarly as before, the tibia was carefully extracted, taking care to remove all soft tissues. Subsequently, the extracted samples were embedded in resin within a 10 mL falcon tube, to orient the samples in a consistent and reproducible way. Finally, the resin was trimmed to a height of approximately 4 cm. All those steps are illustrated in Figure 2.14.

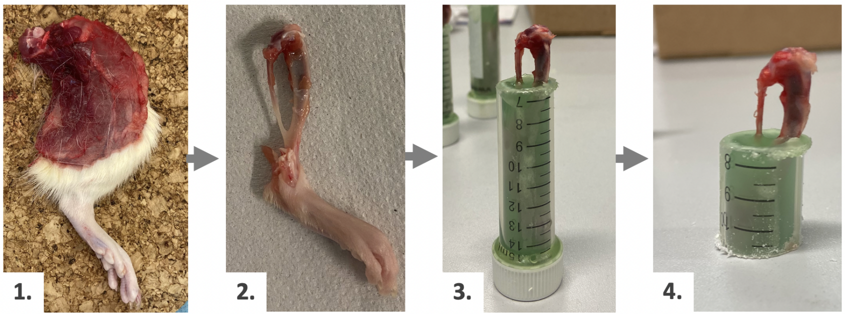

Figure 2.14: Illustration of the different steps involved in the resin embedding process of the experimental part during the tibia extraction. (1) Extracted lower limb of rat. (2) Extraction of the tibia and foot of the rat without soft tissues. (4) Sample embedded in resin. (6) Cut embedded sample.

To achieve optimal reproducibility, all samples were embedded in resin using the same method. Regarding the depth of embedding, when the entire leg was retained for testing, the sample was immersed only up to the level of the patellar tendon. This approach was taken to avoid constraining the natural motion of the knee, allowing for a more accurate knee mechanics representation.

The embedding of the tibia alone was immersed to a slightly lesser extent, reaching only halfway down the tibia. This solution was selected to maximize the amount of tissue outside the resin, and therefore capture the mechanics of the bone more accurately.

For samples where the entire leg was retained, the tibia was embedded in the resin in such a way that the tibial plates were parallel to the surface compressing the sample. A check was automatically performed afterwards to ensure this alignment with the surface of the compressor. Additionally, a cup was designed and 3D printed with Verowhite resin to constrain the leg at knee level in the natural position of the rat. This position is illustrated in Figure 2.15 where the position of the bones in the rat's lower limbs is represented. Unlike humans, the tibia and femur are not aligned, but they have a certain angle (θ) in the resting position. This natural angle was reproduced in the experiments. To constrain the bone in a position as realistically as possible, a cup was created with an oval hollow to allow the bone to settle into it (see Figure 2.16). Moreover, an extension of this oval allowed the femur to rest in a less constraining position, closer to reality. This cup was designed using *IronCAD* software and printed using the 3D printer *Objet260 Connex2* from *Stratasys*.

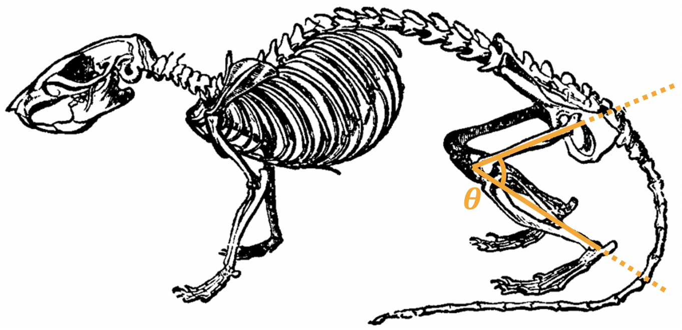

Figure 2.15: Illustration of the bone rat position in resting state [93].

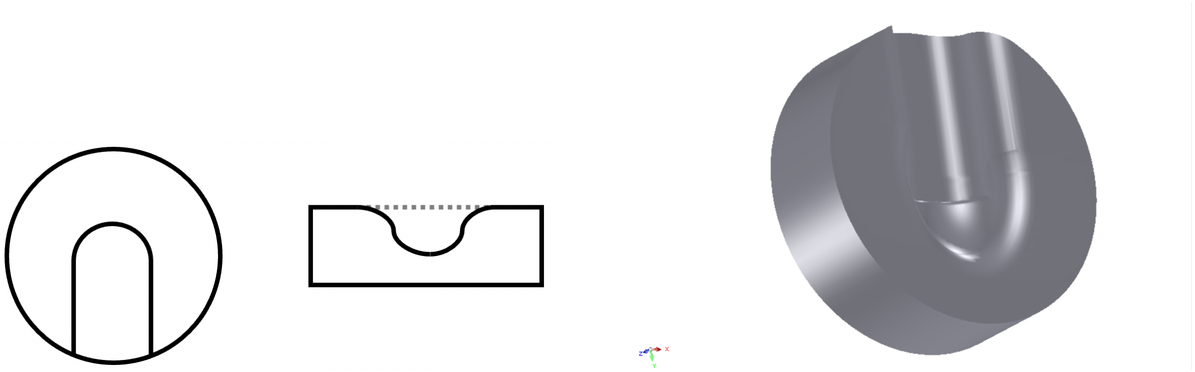

(a) Top (left) and front (right) view

(b) Real cup

Figure 2.16: Illustration of the (a) scheme of the upper cup in the top (left) and front (right) view and (b) of the real upper cup made up to maintain the lower limb in the resting position.

For the resin setting of the tibia alone, a particular precaution concerning the parallelism between the plates and the contact surface of the compressor was carried out. This attention was taken to approximate the conditions imposed by the finite element method, which applies a vertical downward force on the sample. During compression, if the plates are not perfectly aligned, a shearing phenomenon appears, which could lead to distorted results. By ensuring a perfect alignment, such discrepancies are minimized and the accuracy of the experimental outcomes is optimized.

2.2.3 Loaded conditions

For the loading conditions, a constant displacement rate of 1 mm/min was imposed on the test samples, allowing a quasi-static compression test. For the compression of the entire leg, prior to the start of the test, the top of the cup was securely bonded to the top plate of the compressor and the bottom of the resin tube was similarly attached to the bottom plate of the compressor. The compressor used in this study is the *MTS Criterion*™ *Model* 43, capable of exerting forces of up to 600 kN. It features a machine-induced vibration reduction system and offers rapid force application capabilities. For the tibia alone, only the bottom of the resin tube was glued to the compressor while the upper part of the tibia remained in the open air.

In our study, the maximum force applied to the whole leg specimens was approximately 1000 N for the entire leg and approximately 200 N for the tibia alone. This compression system was used with two parallel plates that compressed the specimen thanks to the movement of the upper plate while the lower plate remained static. A representation of the compression system for the entire leg compression is provided in Figure 2.17.

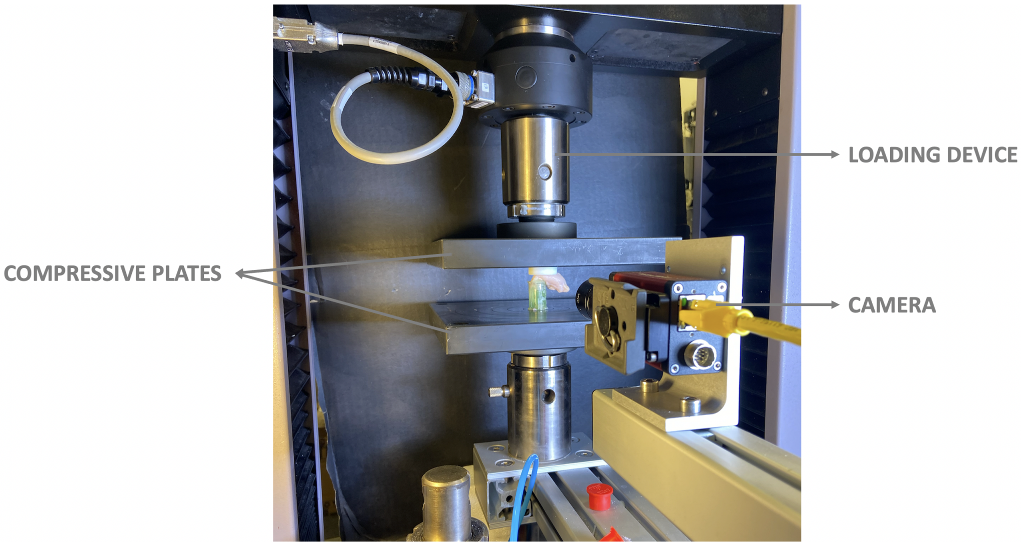

Figure 2.17: Illustration of the compression setup.

The compression process was also recorded using a *NIKON AF Micro-NIKKOR 60mm f2.8 D* camera. This camera has excellent resolution to capture the detailed changes undergone by the sample during compression. Throughout the tests, two images per second were taken, facilitating the further analysis of the bone's response to the applied load.

2.3 Statistical analyses

For the computational aspect of this study, a total of 12 samples were used without the addition of the growth plate, comprising 6 old and 6 young specimens. While adding the growth plate, only 3 samples were analyzed, i.e. 1 old and 2 young bones. On the other hand, for the experimental part, a total of 14 samples (4 of 1-month-old, 3 of 2-month-old, and 7 of 3-month-old) were collected. Inter-group comparisons were made between old and young samples. Intra-group comparisons were also performed within the studied areas, namely the metaphyseal and the subchondral part of the bone. Furthermore, intra-group comparisons based on the type of bone, i.e. cortical or trabecular, were as well implemented to discern their impact on the micromechanical behavior of the proximal rat tibiae. To ensure that the obtained results were significantly different, statistical analyses were conducted. These analyses enabled the identification of important patterns and trends, facilitating the establishment of meaningful conclusions. To perform these statistical analyses, various functions of the *Matlab* software have been used.

The comparison between two independent groups can be established using the *Student's t* test which compares the means of both groups. This type of test will thus be used to make all the comparisons of this study. The first step of this test is to calculate the *t* value, which is the ratio between the mean difference and the standard error. Two main conditions should be fulfilled to apply this type of test. The first condition indicates that the studied groups should have a normal distribution, which can be checked using to the Kolmogorov-Smirnov test. The second main condition indicates that both groups should have equal variance [94]. However, *Matlab* software includes an adaptation of this function that does not require the variances to be equal between the two tested samples. This option will therefore be activated or deactivated, depending on whether the variances are equal or not. In *Matlab*, the used open source function is the TTEST2 function.

For the comparison of more than two groups, a switch in the comparison test is necessary. In this specific case, the one-way *ANOVA* test without repeated measurement should be conducted to compare the means of all the studied groups. This type of test will be used for the comparison of the addition of the growth plate with different Young's modulus values. The first step of this test is to calculate the *F* value, which is the ratio of the variability between the different groups and the variability of the observations within those groups. Similar to the previous test, the *ANOVA* test imposes to have a normal distribution for all the studied groups [94]. In *Matlab*, the used open source function is the ANOVA1 function.

For those types of tests, two main hypotheses need to be applied, i.e. the null hypothesis and the alternative hypothesis. The latter one assumes that the means are significantly different, whereas, for the null hypothesis, the assumption of no statistically significant difference between the means is emitted [94].

The result of the *Student's t* test is the *p-value* variable, which indicates the probability of a statistical model, under the null assumption, to obtain a value at least as extreme as the one observed. Generally, the imposed significance level is set to 0.05, meaning that if $P < 0.05$, the means of both groups are statistically different, rejecting the null hypothesis. Conversely, if $P > 0.05$, the means of both groups are considered as statistically equivalent [94]. Since the one-way *ANOVA* test is an extension of the *Student's t* test for more than two groups, its results are interpreted in the same way. If $P < 0.05$, the means of the studied groups are statistically different, leading to the rejection of the null hypothesis. Conversely, if $P > 0.05$, the means of the studied groups are considered as statistically equivalent [94].

Chapter 3

Results

The following chapter aims to clearly present the results obtained during the μ-finite element simulations as well as in the experimental part.

For the computational part, an in-depth study of the apparent stiffness of each plate was conducted. This was followed by a detailed analysis of the effective strain distribution, incorporating both qualitative and quantitative approaches. For the qualitative part, top views and cross-sectional slices of the bone were used to provide both global and detailed perspectives. For the quantitative part, an initial comparison was performed to assess the impact of varying bone Young's modulus values on the results obtained. After this comparison, the Young's modulus was held constant between young and old bones to isolate the effects of microstructure. The influence of microstructure on bone mechanics was first evaluated separately for old and young bones, and then compared between the two. Additionally, an analysis of the effective strain distribution was also carried out, focusing specifically on slices with and without struts, to determine the impact of these struts on bone mechanics. Another important parameter, the mean of the principal element strain, was also studied in-depth to understand in which way the elements present in the bone are deformed, i.e. in tension and in compression. To achieve a more realistic simulation, the growth plate was introduced between the subchondral and metaphyseal regions. The Young's modulus of this growth plate was changed to simulate both healthy and pathological conditions.

A color code has been carefully chosen to differentiate between young and old bones in the simulations. Young bones are represented by the color orange. For old bones, a distinction was made based on the attributed Young's modulus values, either 25.5325 MPa or 29.5559 MPa. Old bones with a Young's modulus of 29.5559 MPa were represented in blue, while old bones with a Young's modulus of 25.5325 MPa, were represented in purple. The latter are labeled in the graphs as 'Old - same E' to indicate that the imposed Young's modulus is identical to that of young bones.

For the experimental part, an initial analysis focused on compression tests conducted on the whole bone, examining the resulting "displacement-force" curve, was carried out. Subsequently, a more detailed study of the compression curves on the tibia alone was performed, allowing for a direct comparison between the experimentally obtained results and those derived from computational simulations.

In the experimental part, all the tested samples are young. Nevertheless, their age differs from one sample to the other. Once again, color code has been chosen to differentiate 1 and 2-

month-old samples from 3-month-old samples. The 1 and 2-month-old tested samples were represented in orange while the 3-month-old samples were represented in pink/purple.

3.1 Computational part

3.1.1 Plateau apparent stiffness

The first property to be examined is the apparent stiffness of each plateau. A comparison between the different simulations, specifically young bone vs old bone (considering both Young's moduli), will be carried out to assess the influence of aging on the plateau's apparent stiffness. Subsequently, a comparison between the two plateaus, medial and lateral, will be performed to determine if a significant difference exists between them.

Figure 3.1 depicts the two tibial plateaus. The lateral plateau is slightly larger than the medial plateau. This larger area definition of the lateral part was deliberately chosen to replicate in vivo conditions as closely as possible.

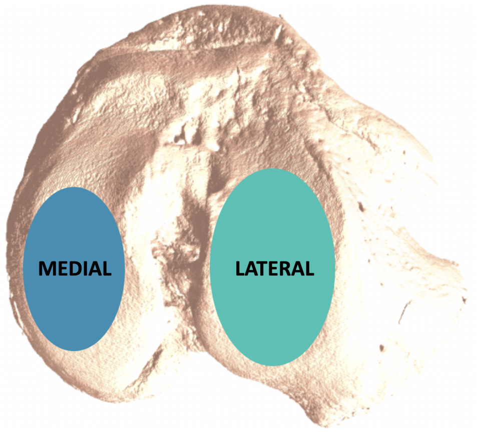

Figure 3.1: Illustration of the two plateaus, medial and lateral on an adult/old bone, top view.

Figure 3.2(a) shows the apparent stiffness of the medial plateau as a function of age and Young's modulus. In general, older bones exhibit greater medial plateau apparent stiffness compared to younger bones, regardless of Young's modulus. When the Young's modulus of older bones is reduced, the apparent stiffness of its medial plateau also decreases, which is expected since the bone itself is less stiff due to its material properties. Furthermore, the standard deviation in old bones is greater than in young bones, indicating a greater diversity of apparent stiffness with aging. Although the difference between old and young bones is smaller, it remains significant, as confirmed by a student t-test.

Figure 3.2(b) shows the apparent stiffness of the lateral plateau as a function of age and Young's modulus. The general behavior of apparent stiffness is similar to that of the medial plateau, with older bones demonstrating higher apparent stiffness and greater standard deviations than younger bones. However, in the lateral plateau, an outlier value was identified in a young bone sample, with an apparent stiffness value exceeding the threshold defined by

$$q_3 + w * (q_3 - q_1), \tag{3.1.1}$$

where q_3 represents the third quartile, q_1 represents the first quartile and w equals 2.7σ (where σ is the mean). This indicates that this outlier is significantly higher than typical apparent stiffness values for young bones. A student t-test was performed to determine the significance of the observed differences. The results indicate that the difference between young and old bones is significant regardless of their Young's modulus. However, the difference between old bones with a Young's modulus of 25.5325 GPa and those with a Young's modulus of 29.5559 GPa is not significant. This finding suggests that the lateral plateau is therefore less affected by the changes in Young's modulus than the medial plateau.

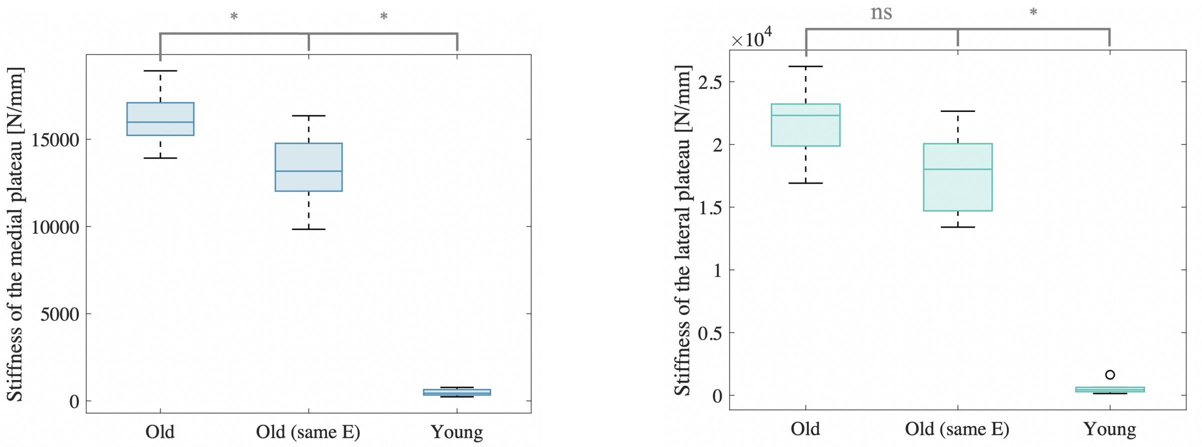

(a) (b)

Figure 3.2: Box plot illustrating the mean and the standard deviation of the apparent stiffness of (a) medial and (b) lateral plateau in N/mm for the young vs old bone, with the two Young's moduli, i.e. 25.5325 GPa and 29.5559 GPa. Outlier values are represented as 'o'. '*' means $p < 0.05$ and 'ns' stands for not significant.

To obtain a complete analysis of the apparent stiffness behavior of each plateau, a comparison between lateral and medial plateaus is necessary. Figure 3.3 presents the average apparent stiffness for each plateau, along with its standard deviation, as a function of specimen age and Young's modulus applied. Generally, the average apparent stiffness of the lateral plateau is greater than that of the medial plateau. For old bones, regardless of Young's modulus assignment, the difference in apparent stiffness between the medial and lateral plateau is significant. Conversely, for young bones, the difference in apparent stiffness between the two plateaus is not significant, indicating a more homogeneous apparent stiffness distribution in young bones between the two plateaus compared to old bones.

3.1.2 Effective strain distribution

To gain an in-depth understanding of the micromechanical behavior of the proximal tibia in aging rats, a qualitative analysis will first be conducted, followed by a more quantitative analysis to elucidate the internal bone dynamics when force is applied to the tibial plateaus.

As previously mentioned, the initial focus will be on studying the effective strain distribution. This property is directly derived from the strain energy density (SED). By examining the effective strain distribution, an analysis of the way the bone deforms when a force is applied at each plateau can be performed.

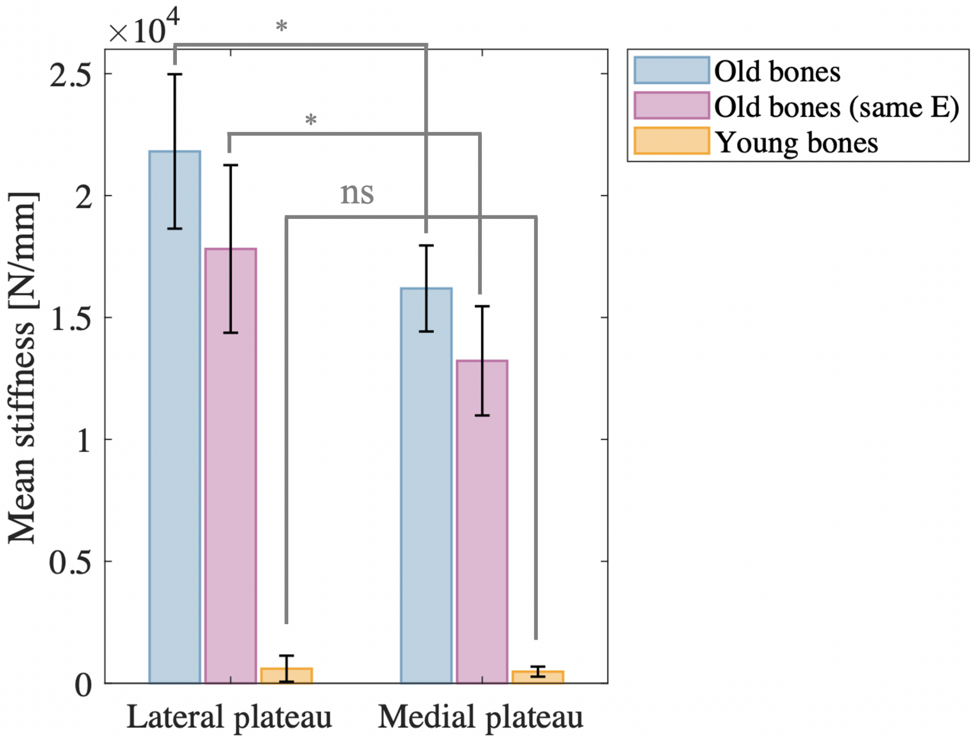

Figure 3.3: Bar plot illustrating the mean and standard deviation of the apparent stiffness for the medial and lateral plateau, in young and old bones, for two Young's moduli, i.e. 25.5325 GPa and 29.5559 GPa.
'*' means $p < 0.05$ and 'ns' stands for not significant.

3.1.2.1 Qualitative visualization

For each image, the color scale was restricted to display only the effective strain ranging from 0 to $5 * 10^{-4}$ [-]. This limitation was applied to correctly visualize bone behavior, while preserving essential information. This method will enable a consistent comparison between bones without distortion from varying color scales. All images depict the bone in its undistorted configuration.

Old bone

Figure 3.4 illustrates the distribution of effective strain (dimensionless) in the old bone labeled as 1VD with the Young's modulus of the old bone, i.e. 29.5559 GPa, using a color gradient. In this gradient, red indicates high strain ($5 * 10^{-4}$ [-]), while dark blue represents no strain.

In the image below, a concentration of deformation is observed along the ellipse contours, corresponding to the area where the forces were applied. This concentration of deformation diminishes as the distance from these contours increases. Additionally, a lighter zone, corresponding to an increase in deformation, can also be observed in the depression between the two ellipses.

For the frontal slices, five were made along the length of the bone, to capture important properties. Notably, struts are present to connect the metaphyseal and subchondral parts. Figure 3.5 shows that the effective strain increases within these struts, as indicated by the color transitioning towards red inside those structures. This concentration of deformation is also observed at the fixed end of the bone (at the bottom of the image). In the last slice (number 5), at the front of the bone, deformations seem to attenuate, indicating a lower effective strain in this area compared to the rest of the bone.

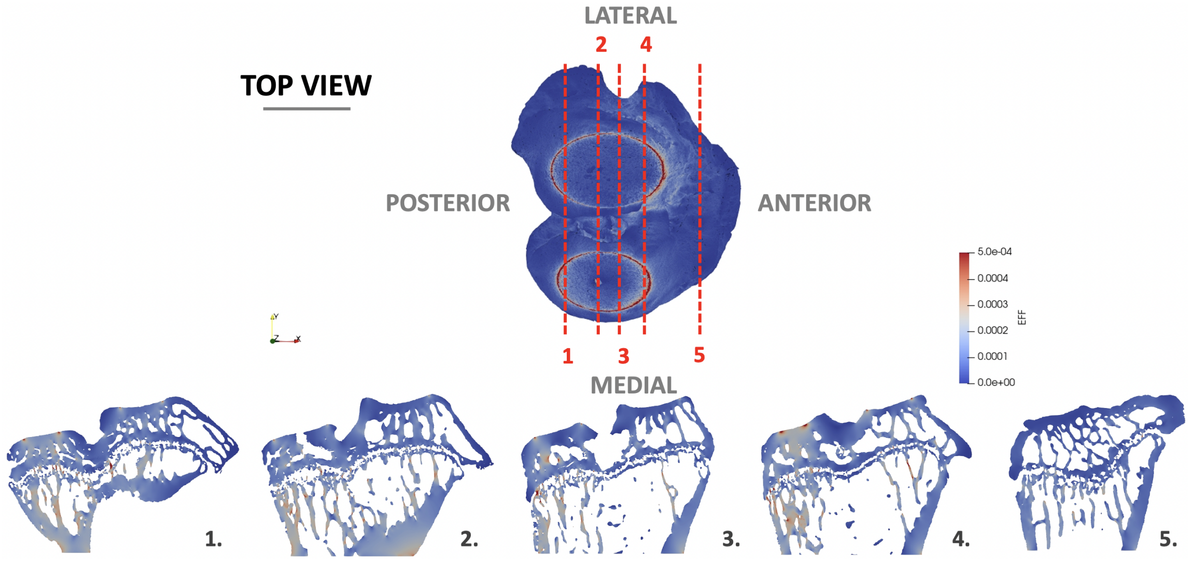

Figure 3.4: Illustration of the distribution of the effective strain throughout the entire old bone 1VD with the Young's modulus of the old bone, i.e. 29.5559 GPa, along with five cross-sectional frontal slices. Each slice is numbered for reference from 1 to 5.

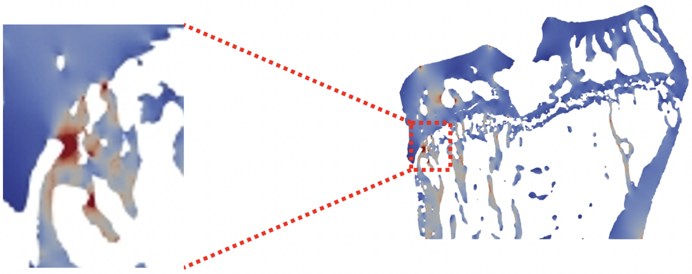

Figure 3.5: Illustration of the distribution of the effective strain throughout the slice labelled as 3. in the old bone 1VD with the Young's modulus of the old bone, i.e. 29.5559 GPa, with a zoom on strain concentration in struts.

To distinguish the effect of the contributions of microstructure versus material properties in the observed mechanical response, further study of the same bone but with the Young's modulus of young bone, i.e. 25.5325 GPa, is required. This is shown in Figure 3.6. When compared with the previous figure, no significant changes are visible to the naked eye. The distribution inside the bone is very similar, suggesting that the value imposed on Young's modulus value between old and young samples does not, at first glance, significantly influence the distribution of deformations within the bone.

Other old bone samples are not shown here, as the general distribution of effective strain in old bones is very similar across the different samples.

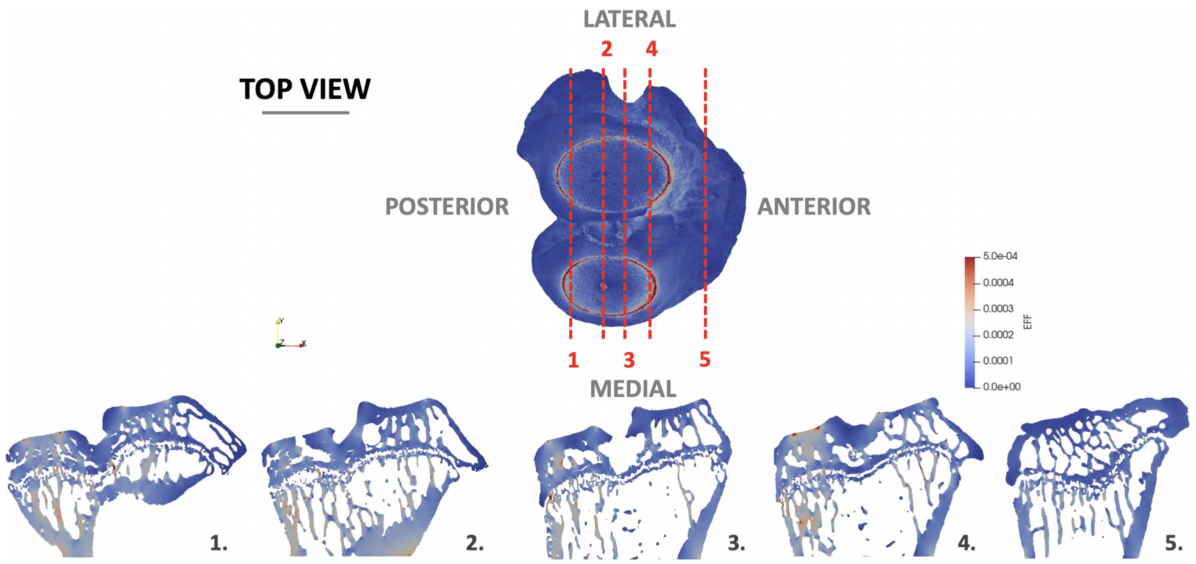

Figure 3.6: Illustration of the distribution of the effective strain throughout the entire old bone 1VD with the Young's modulus of the young bone, i.e. 25.5325 GPa, along with five cross-sectional frontal slices. Each slice is numbered for reference from 1 to 5.

Young bone

Greater variability was observed in the effective strain distribution of young bones (see Appendix C.3). To cover the full range of behaviors observed in these young samples, two bones with markedly different responses were selected, i.e. 11D and 14D.

Figure 3.7 illustrates the distribution of effective strains within the young bone referred as 11D. As in previous Figures, red indicates high effective strain regions, while blue indicates areas with no effective strain.

Thanks to the visualization of the top of the bone, a behavior quite different from that observed in old bones is evident. Indeed, in this young bone, there is a concentration of deformation in the front of the bone, as well as along the boundary conditions similarly to old bones. The region between the two ellipses where the force was applied is once again subjected to significant deformation, which appears to be greater compared to old bones.

In-depth analysis using cross-sectional visualizations of the interior of the bone reveals a previously unknown behavior. Specifically, for this young sample, a concentration of deformation is primarily located in the subchondral part of the bone, while in the metaphyseal part, there are minimal deformations. However, this pattern changes as the front of the bone is approached, where deformation extends into the metaphyseal part as well thanks to struts presence. The concentration of deformation at the front of the bone is also observed using cross-sectional frontal slices.

Figure 3.8 depicts the deformation distribution within the young bone labeled as 14D. Compared to the previous visualization, the deformation behavior shows distinct characteristics. Specifically, the presence of a pronounced concentration of deformation at the front of the bone is either absent or significantly reduced. However, the deformation along the contours of the ellipses where the force was applied is still noticeable, as well as in the depression between these two plateaus. Compared to older bone samples, deformations appear more pronounced.

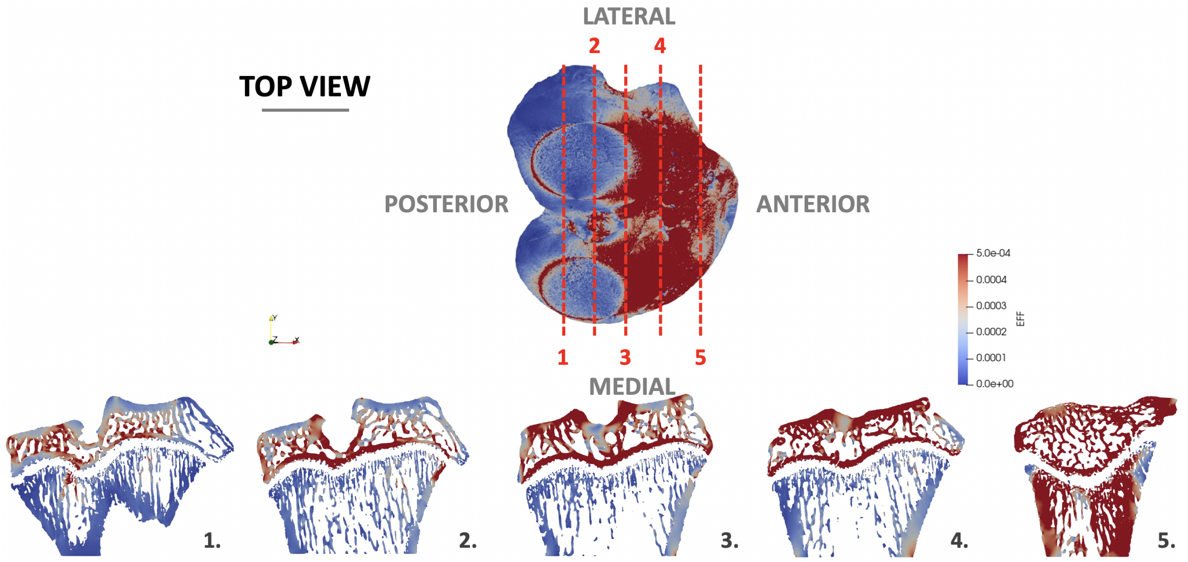

Figure 3.7: Illustration of the distribution of the effective strain throughout the entire young bone 11D, along with five cross-sectional frontal slices. Each slice is numbered for reference from 1 to 5.

With regard to force distributions within the bone, a set of five slices was once again used to capture the deformation characteristics within the bone. Similar to the young bone 11D, a limited number of struts are present to connect the subchondral to the metaphyseal part. Nevertheless, when these bridges were present, as illustrated in slices 1 and 2, deformation propagates effectively from one side of the bone to the other. Conversely, in areas without any presence of strut, deformation distribution in the metaphyseal part was significantly reduced.

A slight increase in deformation is also observed on the left at the opposite end of the bone, where it is constrained in three directions (x, y, and z).

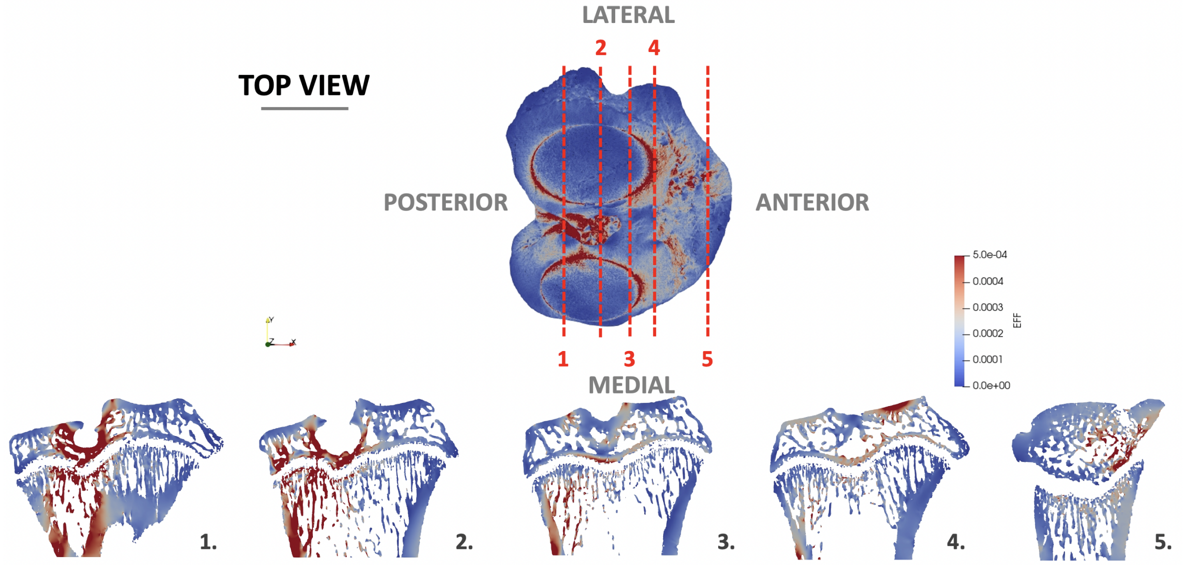

Figure 3.8: Illustration of the distribution of the effective strain throughout the entire young bone 14D, along with five cross-sectional slices. Each slice is numbered for reference from 1 to 5.

3.1.2.2 Quantitative visualization

To gain a more quantitative understanding of the distributions within the bone, several probability distributions were established. To facilitate future comparisons, each distribution was normalized to obtain an area under the curve equal to 1, i.e. a Probability Density Function (PDF) distribution. In each bone, four zones were delimited, i.e. the cortical subchondral part, the trabecular subchondral part, the cortical metaphyseal part, and the trabecular metaphyseal part. In each case, two colors were selected to distinguish the subchondral parts from the metaphyseal parts. In addition, to distinguish the cortical part from the trabecular part, the latter is shown as a dotted line.

For each distribution, two crucial parameters were analyzed, i.e. the mean and the width of the distribution, using full width at half-maximum.

Old bone - Material property analysis

The initial analysis focused on the impact of the material properties. For this purpose, a comparison was conducted between old bones with a Young's modulus of 25.5325 GPa and 29.5559 GPa. Old bones with a Young's modulus of 29.5559 GPa were represented using blue shades, while those with a Young's modulus of 25.5325 GPa (equivalent to the Young's modulus of young bones) were depicted in pink shades.

Figure 3.9 illustrates the different probability density functions in the four specified areas, i.e. cortical subchondral, trabecular subchondral, cortical metaphyseal, and trabecular metaphyseal.

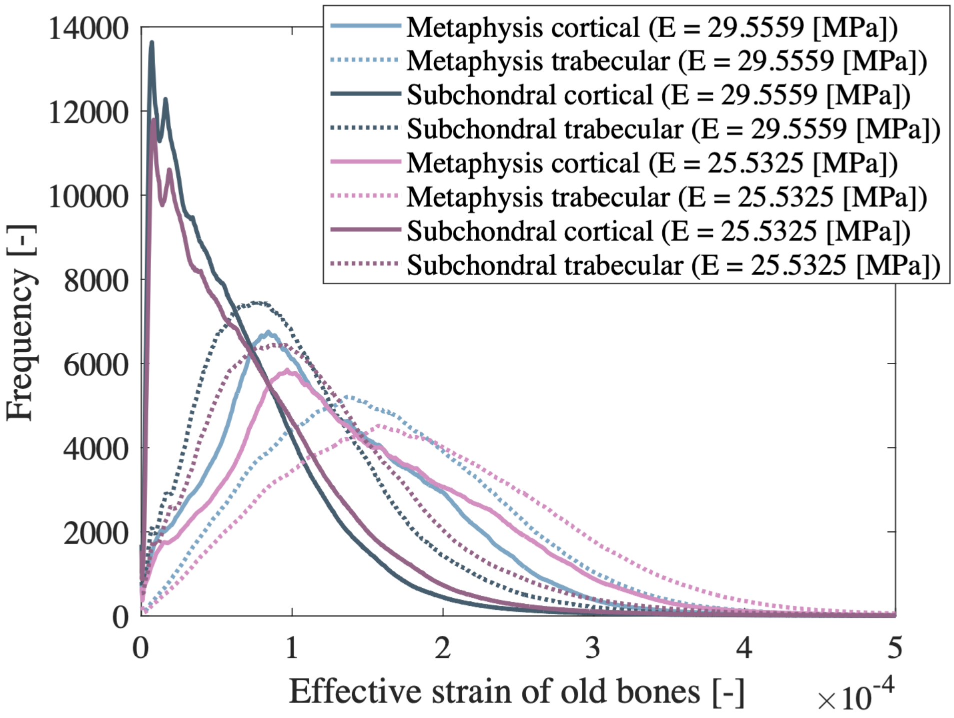

Figure 3.9: Illustration of the probability density function of the effective strain for old bone with different Young's modulus, i.e. 25.5325 GPa (Young's modulus of young samples) and 29.5559 GPa, in the four different delimited areas.

The overall appearance of simulations with different Young's moduli is consistent. Specifically, the shape of the probability density function (PDF) is similar across the two different simulations. However, a slight shift to the right, indicating greater deformations, can be observed as the Young's modulus decreases (for the Young's modulus of young bones).

To determine whether the differences between the curves are significant, a more detailed analysis of the mean and full width at half-maximum (FWHM) was carried out.

Figure 3.10 represents the mean of the effective strain distributions in old bones as a function of their Young's modulus. As previously announced, bones with a lower Young's modulus, equivalent to that of young bones, deform more, as indicated by higher average effective strain values. This difference is a bit more pronounced in the metaphyseal part (20.19 %) compared to the subchondral part (15.56 %).

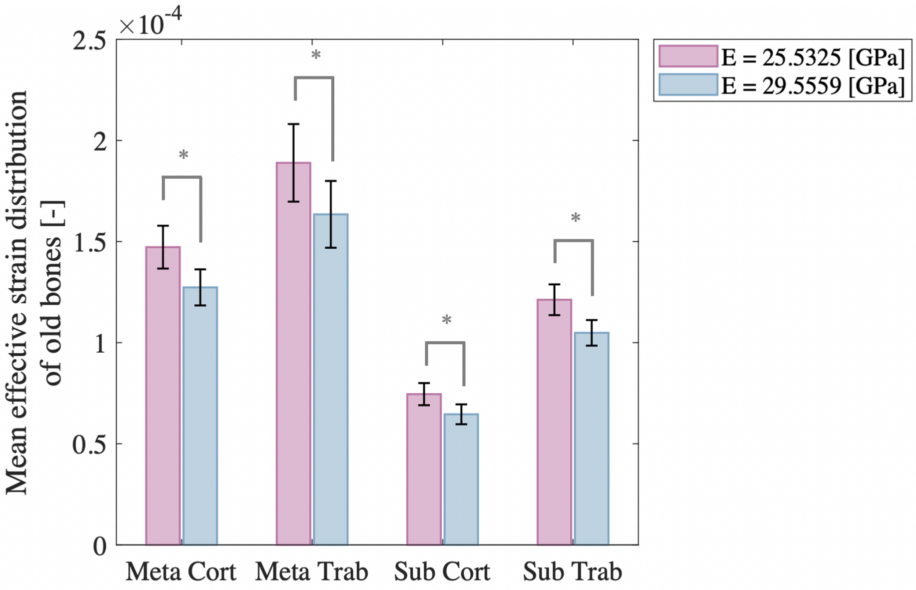

Figure 3.10: Bar plot illustrating the mean effective strain of the PDF distribution for old bone with different Young's modulus, i.e. 25.5325 GPa and 29.5559 GPa, in the four different delimited areas with their error bars. Meta Cort stands for the metaphyseal cortical area, Meta Trab stands for the metaphyseal trabecular area, Sub Cort stands for the subchondral cortical area, and Sub Trab stands for the subchondral trabecular area.
'*' means $p < 0.05$.

Figure 3.11 illustrates the Full Width at Half-Maximum (FWHM) of the effective strain distribution in old bones as a function of their Young's modulus. This parameter measures the level of dispersity within the studied distribution. Indeed, the greater the FWHM, the wider the distribution and therefore the more dispersed the observed values. As depicted in Figure 3.11, older bones with a lower Young's modulus have a higher FWHM, reflecting a greater dispersity of deformation. Conversely, imposing a stiffer tissue will reduce the dispersity of deformations, leading to more homogeneous deformation within the bone. This effect is particularly more pronounced in the metaphyseal part compared to the subchondral area. Indeed, the difference rates in the metaphyseal cortical and trabecular bones are respectively 23.74 % and 22.99 %, while in the subchondral region, those differences are 13.82 % and 12.94 % each. Nevertheless, a non-significant difference is observed in the metaphyseal trabecular part of the bone.

Through these in-depth analyses, significant differences between the two types of simulation with the two distinct Young's moduli were identified, which were not apparent to the naked eye at first sight.

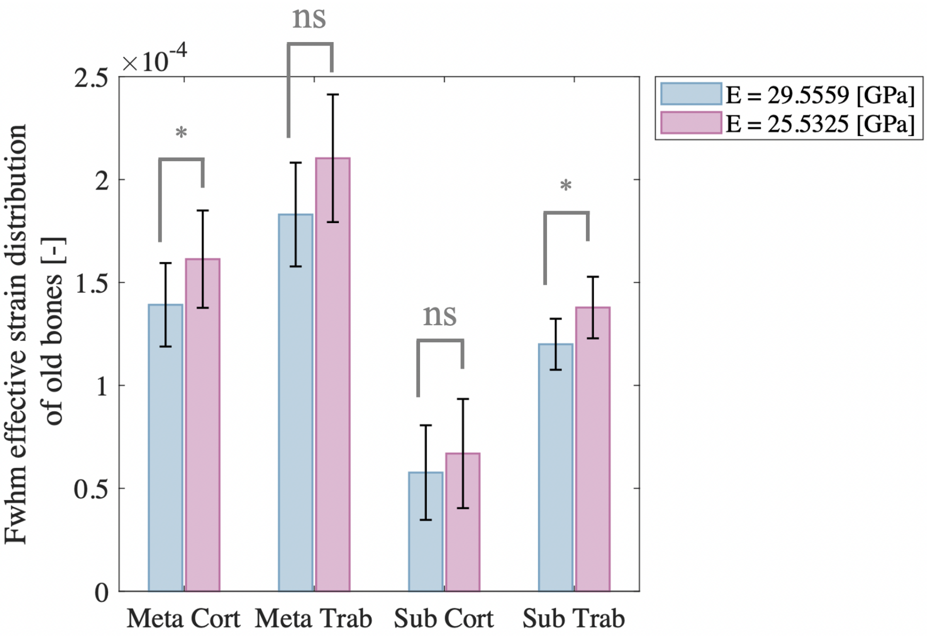

Figure 3.11: Bar plot illustrating the Full Width at Half-Maximum of the effective strain distribution for old bone with different Young's modulus, i.e. 25.5325 GPa and 29.5559 GPa, in the four different delimited areas with their error bars. Meta Cort stands for the metaphyseal cortical area, Meta Trab stands for the metaphyseal trabecular area, Sub Cort stands for the subchondral cortical area, and Sub Trab stands for the subchondral trabecular area. '*' means $p < 0.05$ and 'ns' stands for not significant.

Old bone - Microstructural influence analysis

To isolate the effects of changes induced by bone microstructure, an in-depth analysis will be conducted on old bone samples that have been assigned the same Young's modulus as young bones. This process ensures that any observed differences in the effective strain distributions can be solely attributed to variations of bone microstructure rather than applied material properties.

Figure 3.12 presents the probability density function (PDF) for old bones with the same Young's modulus as young bones. At first glance, the subchondral part exhibits less deformation compared to the metaphyseal part, as indicated by the effective strain distributions being skewed towards lower effective strain values. Moreover, the type of bone, whether cortical or trabecular, significantly impacts the behavior of the distributions. Generally, trabecular bone deforms more than cortical bone, as reflected by the distributions oriented towards higher values of effective strain.

To extract and highlight the most important information from the graph, the mean and FWHM were isolated for the four delimited regions. The mean values, along with their standard deviations, were plotted. In addition, the individual values for each bone sample were presented. These individual values were determined from the specific probability distributions for each bone, as detailed in Appendix C.1.

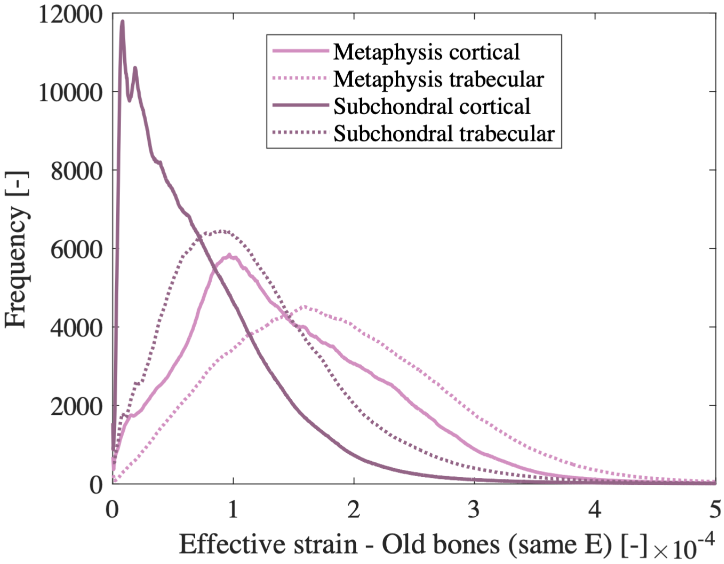

Figure 3.12: Illustration of the probability density function of the effective strain for old bone with the same Young's modulus as young bones, i.e. 25.5325 GPa, in the four different delimited areas.

Figure 3.13(a) displays that the part of the bone which exhibits the least deformation is the subchondral bone, and more particularly the cortical part in both the subchondral and metaphyseal part. Conversely, the trabecular part demonstrates higher deformation than the cortical part. Each part of the bone has a significantly different mean compared to the three other parts. The difference rate between the cortical and trabecular bone in the metaphyseal part is 28.31 % while in the subchondral part, this difference is estimated to be 62.60 %, indicating a much higher difference between the type of bone in the subchondral region. Nevertheless, the standard deviations are much more pronounced in the metaphyseal part compared to the subchondral area.

Figure 3.13(b) depicts the dispersity of the studied distributions. Specifically, the metaphyseal region exhibits a greater dispersity compared to the subchondral bone, indicating more diverse effective strain values in this part of the bone. This parameter mirrors the behaviors related to the mean values where the trabecular metaphyseal part shows both the highest dispersity and the highest mean effective strain. Conversely, the cortical subchondral part demonstrates the lowest dispersity and the lowest mean effective strain. The difference rates follow as well the mean behavior, indicated by a difference between the two types of bones, named trabecular and cortical, of 23.30 % and 51.45 % in the metaphyseal and subchondral bone, respectively.

Young bone - Microstructural influence analysis

Figure 3.14 illustrates the probability density function of young bones. The shape of these curves differs markedly from those of old bones. Specifically, the values obtained seem to be higher, indicating that young bones tend to deform more than old ones.

The x axis of all curves has been truncated to eliminate outliers and to enhance the visualization of the effective strain distribution in young bones. Those outliers are values which are not physical, thus not corresponding to the real bone behavior. The appearance of outliers is significantly more pronounced in the younger samples, which can partially distort the results.

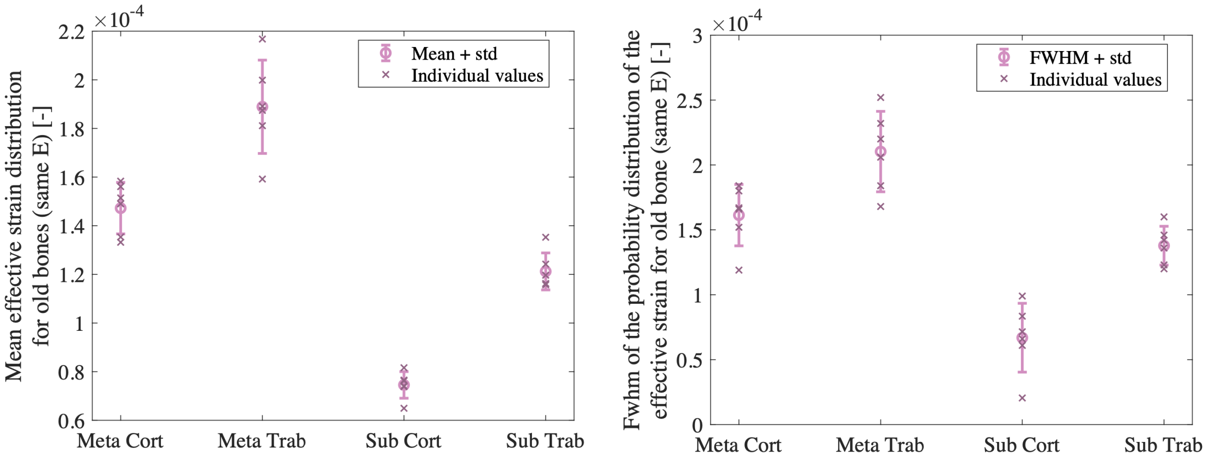

(a) (b)

Figure 3.13: Plot of the (a) mean values and (b) Full Width at Half-Maximum of the density probability distribution of the effective strain for old bones in the four delimited areas. The data are represented as the mean value ± the standard deviation. Individual values are also depicted.

To facilitate a more in-depth analysis, the fundamental parameters of these curves, i.e. the mean and the FWHM, were computed.

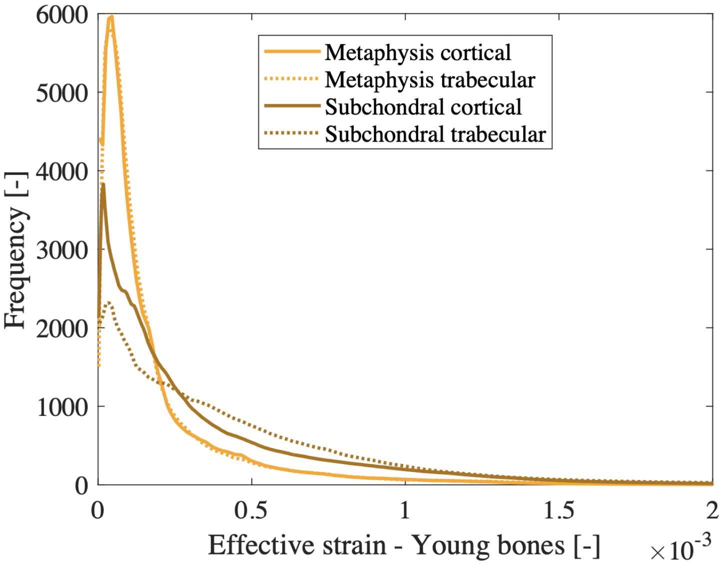

Figure 3.14: Illustration of the probability density function of the effective strain for young bone in the four different delimited areas.

Figure 3.15(a) presents the mean values of the effective strain distributions in young bone samples. Unlike to previous studies, the behavior of the delineated areas in young bones is notably different. Indeed, in young bones, the metaphyseal part deforms less than the subchondral part, contrary to the observations in old bones. Additionally, the distinction between trabecular and cortical bone deformations is no longer as straightforward as it once was. In young bone samples, trabecular bone in the metaphyseal part deforms a bit less than cortical bone, with a difference rate of 2.33 %, whereas the opposite behavior is observed in the subchondral region, with cortical bone deforming less than trabecular bone, indicated by a difference rate of 34.47 %. The standard deviation is much higher in the subchondral parts compared to the metaphyseal ones, which are not statistically significant.

Figure 3.15(b) depicts the dispersity of the distribution, highlighting that it is significantly greater in the subchondral part of the bone compared to the metaphyseal part. With regard to dispersity as a function of bone type, in the metaphyseal region, cortical bone exhibits a bit more dispersed distribution compared to trabecular bone, with a difference rate of 3.33 %. Conversely, in the subchondral region, the opposite phenomenon is observed, with trabecular bone demonstrating considerably greater variability than cortical bone, with a difference rate of 57.28 %. This trend mirrors the pattern observed in the mean values.

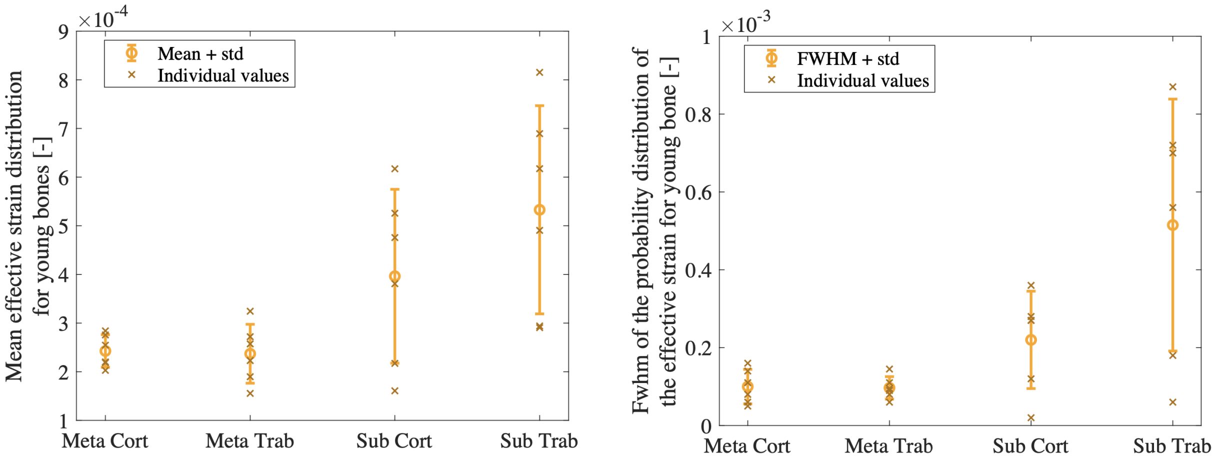

(a) (b)

Figure 3.15: Plot of the (a) mean values and (b) Full Width at Half-Maximum of the density probability distribution of the effective strain for the young bones in the four delimited areas. The data are represented as the mean value ± the standard deviation. Individual values are also depicted.

Young vs old bones - Age-related influence analysis

To understand the influence of age on the distribution of effective strain in the tested samples, comparative bar plots displaying the mean and FWHM values for both old and young bones were generated, along with their associated standard deviations. Moreover, to determine whether the perceived difference between old and young bones is statistically significant, a student-t test was conducted.

Figure 3.16 illustrates the mean of the probability density function (PDF) distribution of effective strain in old and young bones, accompanied by their standard deviations. Generally, a tendency towards greater deformation is observed in young bones. This trend is notably more pronounced in the subchondral area compared to the metaphyseal region. Only the trabecular metaphyseal area does not appear to be overly affected by sample age, as a Student's t-test determined that the difference in mean effective strain between young and old samples was not statistically significant, indicated by a difference rate of 20.28 %. However, in the other three delimited areas, this difference between old and young samples was found to be significant. The difference rate in the metaphyseal cortical, subchondral cortical and trabecular areas are respectively 39.32 %, 81.19 %, and 77.25 %, which are much higher than the one found in the metaphyseal trabecular region.

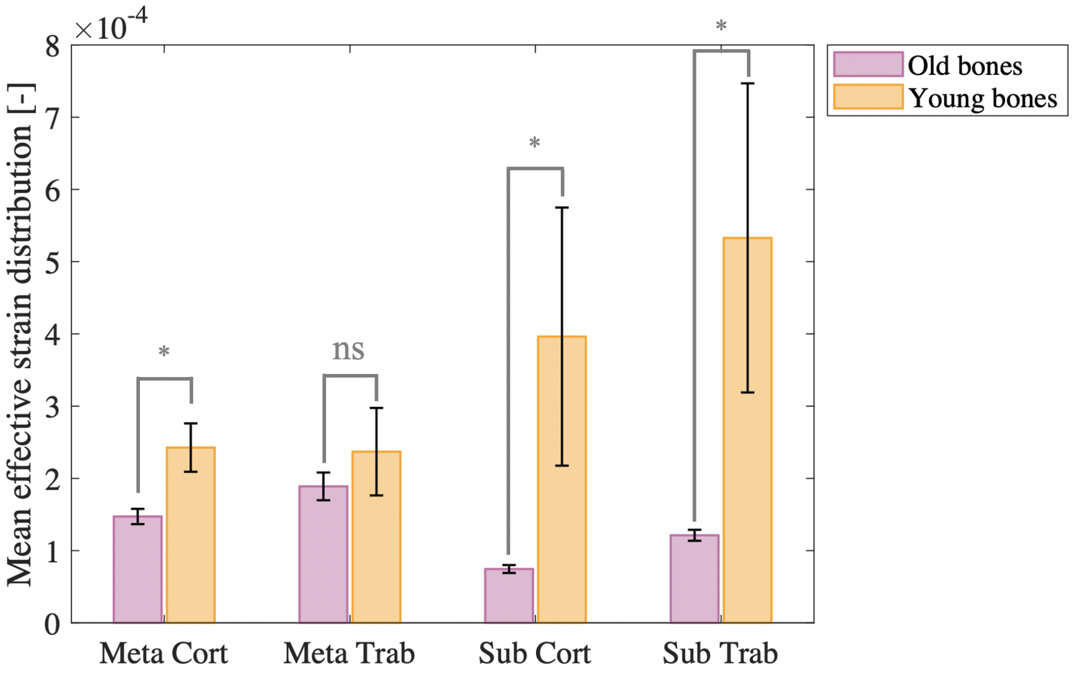

Figure 3.16: Bar plot illustrating the mean of the effective strain distribution for the old bones vs young bones, in the four different delimited areas with their error bars. Meta Cort stands for the metaphyseal cortical area, Meta Trab stands for the metaphyseal trabecular area, Sub Cort stands for the subchondral cortical area, and Sub Trab stands for the subchondral trabecular area.
'*' means $p < 0.05$ and 'ns' stands for not significant.

To achieve a comprehensive analysis of the effective strain's behavior, it is essential to examine the full width at half-maximum (FWHM). Figure 3.17 depicts the FWHM of each distribution in the four defined areas comparing adult and old samples. A difference in behavior between the metaphyseal and subchondral areas can be highlighted. In the metaphyseal area, the dispersity of distributions in young bones is lower compared to old bones, especially in the cortical part where a non-significant difference was found. The difference rates in the metaphyseal cortical and trabecular areas are respectively $38.02\ \%$ and $54.04\ \%$. On the other hand, in the subchondral part, the dispersity is much greater in young bones than in old bones, with more pronounced differences. The differences in the subchondral cortical and trabecular regions are respectively $69.58\ \%$ and $73.24\ \%$. The presence of more outliers at high values in the subchondral part influences the final results and thus induces bias in the observed outcomes.

Struts analysis

As illustrated above, young and old bones exhibit significantly different microstructures, which greatly influence their mechanics. This deformation behavior is strongly influenced by the presence or absence of bridges between the subchondral and metaphyseal parts. In old bones, these types of struts are abundant, allowing deformation to be distributed more evenly throughout the entire bone. Conversely, in young bones, such bridges are present in minimal quantities. To determine the real impact of these struts on the mechanical behavior of bone, an in-depth analysis was carried out comparing bone slices with and without struts. The bone was cut in the xz plane for this purpose. For young bones, identifying a strut-free slice was straightforward; however, for old samples, the task was more challenging. Since all slices in old bones con-

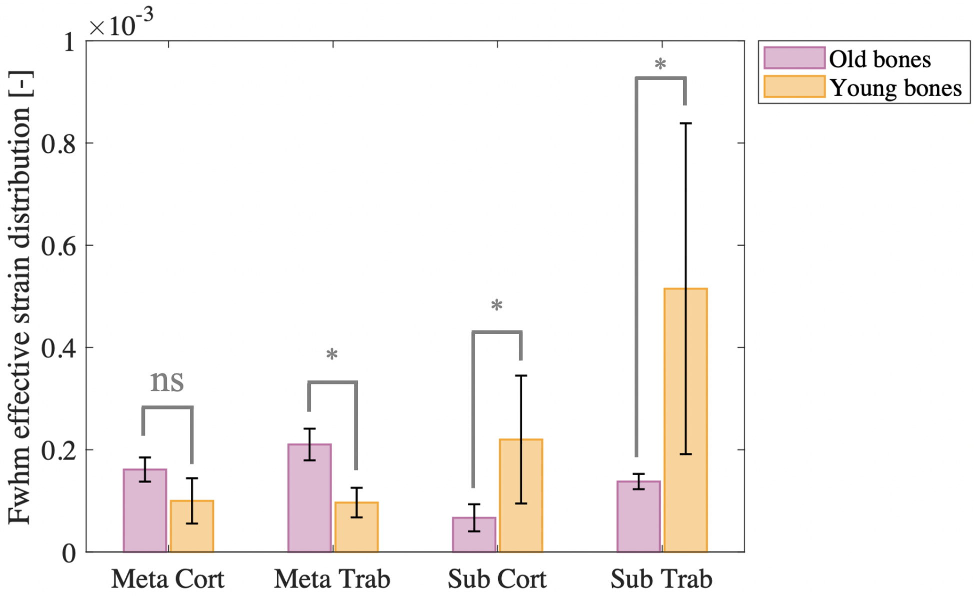

Figure 3.17: Bar plot illustrating the Full Width at Half-Maximum of the effective strain distribution for the old vs young bones, in the four different delimited areas with their error bars. Meta Cort stands for the metaphyseal cortical area, Meta Trab stands for the metaphyseal trabecular area, Sub Cort stands for the subchondral cortical area, and Sub Trab stands for the subchondral trabecular area.
'*' means $p < 0.05$ and 'ns' stands for not significant.

tained more than one strut, the slice with the fewest struts was selected (see Appendix D.1.1). In young bones, given the rarity of struts, a slice with a single strut was chosen for slices with struts, as no other slice contained multiple struts (see Appendix D.2.1 and D.3.1). Nevertheless, a precaution has been taken not to take slices too far apart, reducing the impact of slice position on the obtained results. As in the previous sections, the distribution of effective strain within these slices will be studied.

Due to the high inter-sample variability observed in young bones, an in-depth study of samples 11D and 14D was conducted to capture differences within distributions that exhibit distinct characteristics. For old bones, in contrast, only one sample was analyzed, as the effective strain distributions in old bones are very similar across samples (see Appendix C.2).

To enhance the visualization of bone mechanical behavior in the presence or absence of struts within the selected slice, standard deviations have been depicted solely positively.

OLD BONE - 1VD

Figure 3.18 shows the mean effective strain distribution in the four delimited regions for two types of slice, i.e. those with and without strut, in the old bone 1VD. In this instance, the 'no strut' case indicates that the studied slice has significantly fewer struts than the other slices. All four areas undergo greater deformation when a large number of struts are present. Although the difference is less pronounced in the metaphyseal cortical area, it remains significant.

YOUNG BONE - 11D

Figure 3.19 represents the mean effective strain distribution for two types of slices, i.e. with and without strut, in the young bone sample, labeled as 11D. The trend observed is consistent with previous observations. Indeed, the mean effective strain in the four areas within the

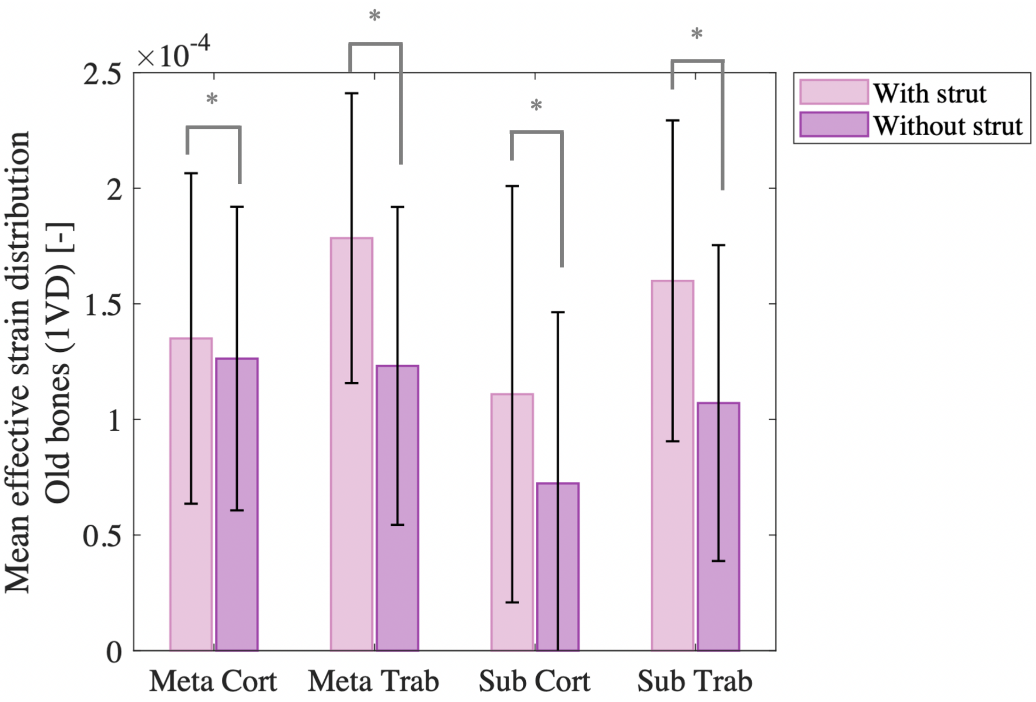

Figure 3.18: Bar plot illustrating the mean of the effective strain distribution, of slices with or without strut, for the old bones named as 1VD in the four different delimited areas with their error bars. Meta Cort stands for the metaphyseal cortical area, Meta Trab stands for the metaphyseal trabecular area, Sub Cort stands for the subchondral cortical area, and Sub Trab stands for the subchondral trabecular area.
'*' means $p < 0.05$.

slice without struts is lower than in the slice with struts. Additionally, the standard deviations are lower in the strut-free slice. The presence of struts therefore increases the variability and the deformation within the bone. The difference in the mean in the four studied areas is significant, indicating that the presence of struts substantially affects the distribution of effective strain. Detailed distributions of the effective strain within these slices are provided in Appendix D.2.2.

YOUNG BONE - 14D

Figure 3.20 illustrates the mean effective strain distribution for two types of slice, i.e. those with and without strut, in young bone sample 14D. The effective strain distribution is consistent with the observations previously made in the other young bone 11D. Specifically, the slice with no strut deforms less than the slice with struts across all four studied zones. This difference is significant in all areas. The standard deviation in the slice with strut is more important, indicating a large variation in effective strain within this slice. The absence of struts reduces this variability, resulting in a more homogeneous distribution within the four areas. For more detailed information, the distributions of these slices can be observed in Appendix D.3.2.

This analysis showed that the presence or absence of struts significantly influences the behavior of an isolated bone slice. Indeed, the general behavior observed across the three bones studied is consistent.

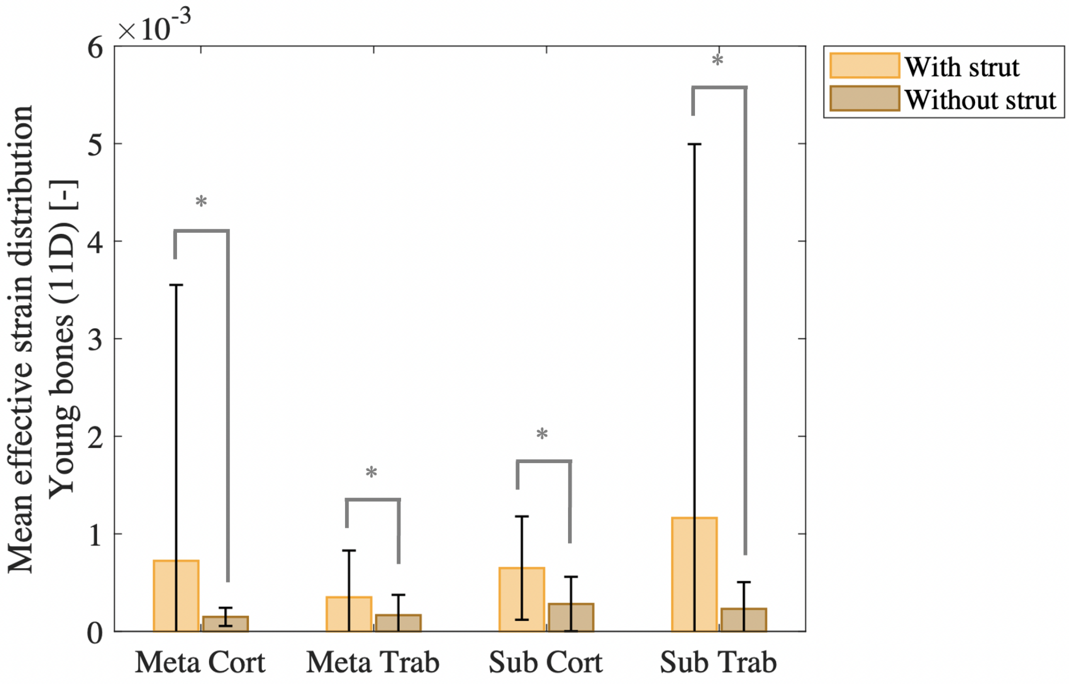

Figure 3.19: Bar plot illustrating the mean of the effective strain distribution, of slices with or without strut, for the young bones named as 11D in the four different delimited areas with their error bars. Meta Cort stands for the metaphyseal cortical area, Meta Trab stands for the metaphyseal trabecular area, Sub Cort stands for the subchondral cortical area, and Sub Trab stands for the subchondral trabecular area.
'*' means $p < 0.05$.

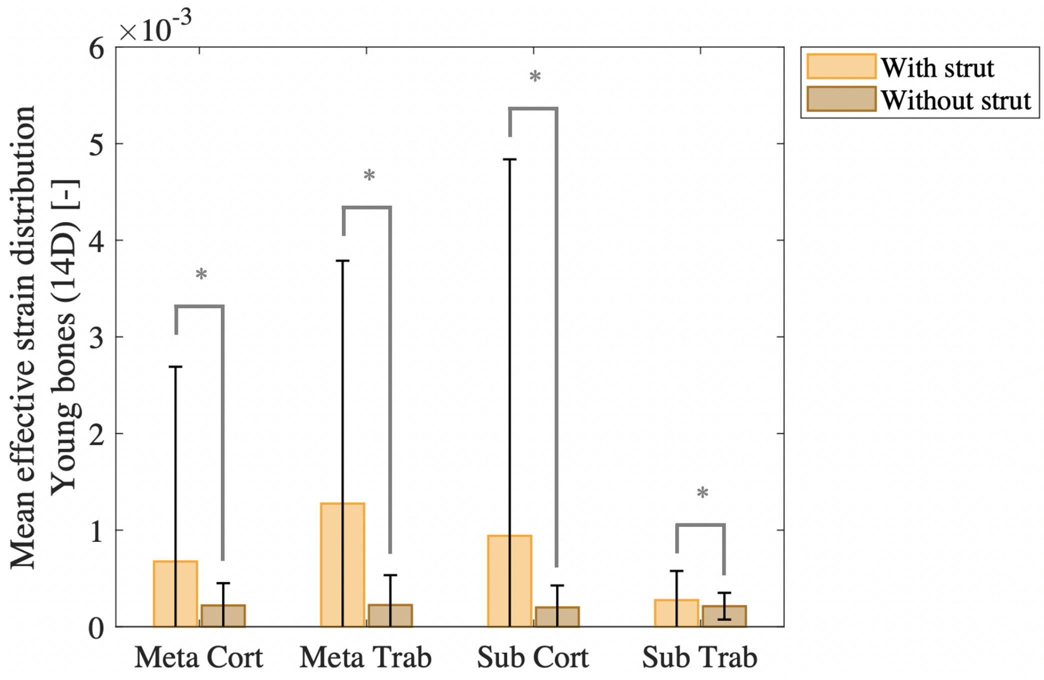

Figure 3.20: Bar plot illustrating the mean of the effective strain distribution for the young bones named as 14D of slices with or without strut, in the four different delimited areas with their error bars. Meta Cort stands for the metaphyseal cortical area, Meta Trab stands for the metaphyseal trabecular area, Sub Cort stands for the subchondral cortical area, and Sub Trab stands for the subchondral trabecular area.
'*' means $p < 0.05$.

3.1.3 Maximum and minimum principal element strain

Another important property to examine is the mean of the maximum and minimum principal element strain within the four compartments, which indicates whether the bone is under tension or compression. A negative strain value signifies that the element is in compression, while a positive value indicates tension. To facilitate a direct comparison between tension and compression, these two variables have been represented on the same graph, as shown in Figure 3.21. This analysis focused exclusively on the subchondral region of the bone, as this region is directly subjected to applied forces and, therefore, is the first to experience deformations. For ease of reading, significant and non-significant differences have been displayed only for the tensile region, as the same statistical results were observed in the compressive region.

Older bones exhibit lower tension and compression values compared to younger bones, along with a reduced standard deviation. This indicates a significant difference between young and old bones in both tension and compression. These differences in tension in the subchondral trabecular and cortical regions are respectively 79.09 % and 83.13 %, while those differences in compression are 71.46 % and 78.48 %. Additionally, older bones seem to deform more in compression than in tension, as reflected by a smaller mean value of positive principal strains compared to negative ones, observed in both the cortical and trabecular regions. In contrast, young bones show less disparity between tension and compression, with more consistent values across both types of strain. This difference in the mean principal strain distribution can be seen individually for bones 1VD and 14D in Appendices E.1 and E.2.

In older bones, higher values in both tension and compression are observed in the trabecular subchondral bone compared to the cortical region. These differences in tension and compression are respectively 22.19 % and 48.09 % and are shown as statistically significant. In contrast, in young bones, the tension values between the subchondral and trabecular regions do not show a significant difference, as indicated by difference rates of 1.38 % and 10.45 % in tension and compression each. However, compression values in young bones appear to differ more notably, although this difference is not statistically significant. Overall, the distinction between trabecular and cortical bone has a more pronounced impact on the tension and compression values in older bones, whereas in younger bones, no significant difference is observed.

3.1.4 Growth plate Analysis

As previously discussed, the presence or absence of struts within the bone significantly influences its mechanics. Nevertheless, until now, an important part has been overlooked in the simulations: the growth plate, a cartilage layer which is located between the metaphyseal and subchondral parts. The impact of this type of tissue on bone mechanics will be examined in the following sections.

3.1.4.1 Qualitative visualization

As before, for each bone, the color scale was restricted to display only the effective strain ranging from 0 to $5 * 10^{-4}$ [-]. This limitation was applied to accurately visualize bone behavior while preserving essential information. This method enables a consistent comparison between bones. All images depict the bone in its undistorted configuration.

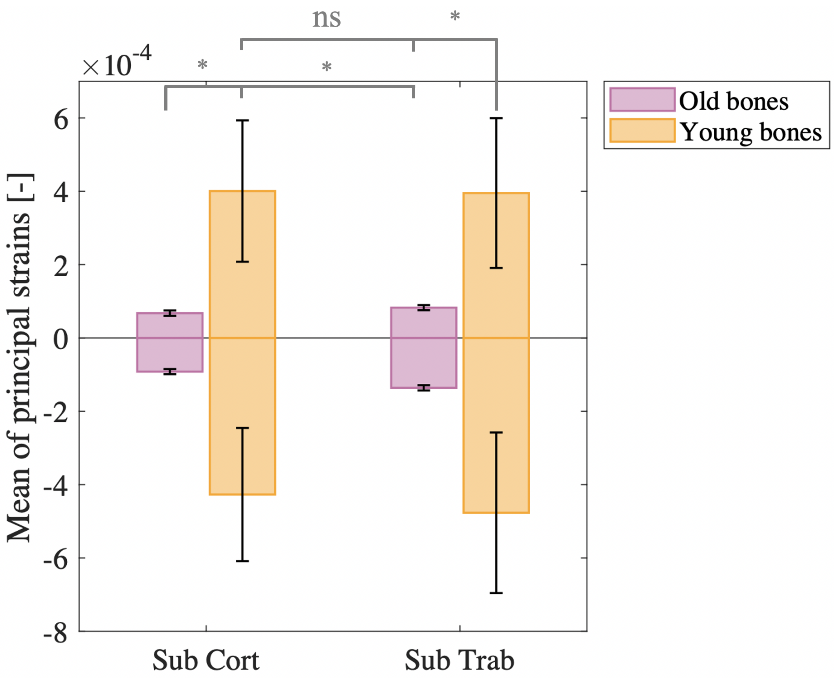

Figure 3.21: Bar plot illustrating the mean of the minimum and maximum principal element strain for young and old bones, with their error bars. Negative values are the minimum principal element strain and positive values are the maximum element strain. Sub Cort stands for the subchondral cortical area, and Sub Trab stands for the subchondral trabecular area. ‘*’ means $p < 0.05$ and ‘ns’ stands for not significant.

Old bone - 1VD

Figure 3.22 illustrates the 1VD bone with an added layer of growth plate between the metaphyseal and subchondral parts. To determine the impact of the addition of the growth plate on the bone mechanics, and to assess the influence of material properties, three Young’s modulus values were carefully selected.

Figure 3.22(a) represents the distribution of effective strain within the bone with the addition of a growth plate layer having a Young’s modulus of 5 MPa, corresponding to the value observed in reality. The growth plate layer appears as the most deformed part of the tissue since it is shown in red. The presence of this growth plate layer leads to a slight increase in deformation in the metaphyseal part compared to when no growth plate is present. Consequently, the addition of the growth plate seems to facilitate a more uniform distribution of deformations in the metaphyseal part of the bone, thereby slightly homogenizing the overall distribution of deformations within the bone.

To investigate the impact of changes in the growth plate’s mechanical properties on the bone’s behavior, the Young’s modulus of the growth plate was modified. Figures 3.22(b) and 3.22(c) depict the distribution of effective strain within the bone following the addition of a layer of growth plate when the Young’s modulus of the growth plate layer is set to 50 MPa and 500 MPa, respectively. At first glance, this change does not alter the distribution of effective strain within the bone itself. However, there is a slight decrease in the effective strain values within the growth plate layer as its Young’s modulus increases. Given that no further insights can be collected through visual inspection alone, a more detailed quantitative analysis is required to uncover any subtle effects.

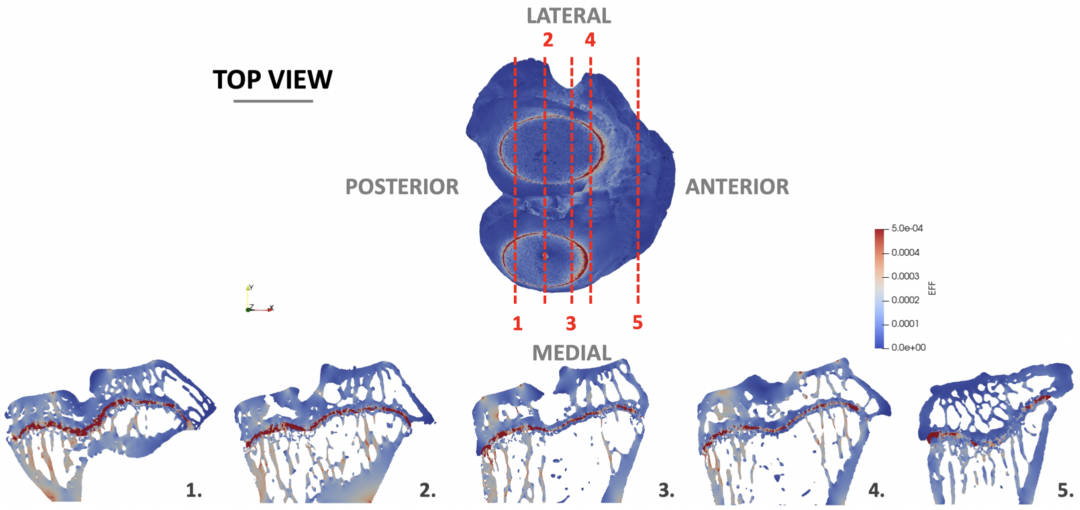

(a) With growth plate (E = 5 MPa)

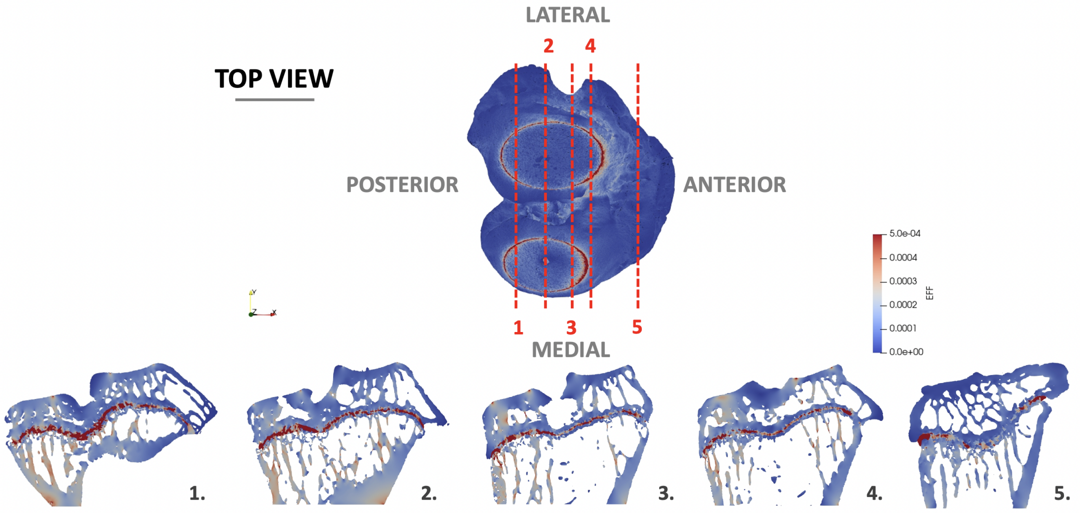

(b) With growth plate (E = 50 MPa)

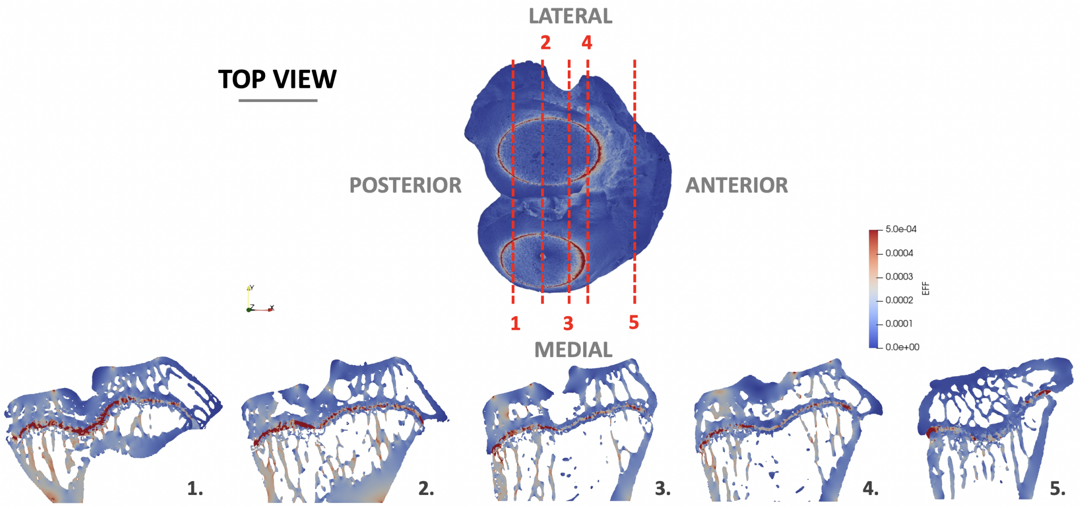

(c) With growth plate (E = 500 MPa)

Figure 3.22: Illustration of the distribution of the effective strain throughout the entire old bone 1VD, with the Young's modulus of the young bone, i.e. 25.5325 GPa, along with five cross-sectional slices, while adding growth plate with a Young's modulus of (a) 5, (b) 50, and (c) 500 MPa. Each slice is numbered for reference from 1 to 5.

Young bone - 11D

Figure 3.23 illustrates the bone sample labeled 11D with an added layer of growth plate between the subchondral and metaphyseal parts.

Figure 3.23(a) represents the distribution of effective strain in the 11D bone when a layer of growth plate with a Young's modulus of 5 MPa is added. Due to the significantly lower Young's modulus of the growth plate compared to the one of bone, it undergoes much greater deformation, as indicated by the dark-red coloring. Furthermore, when viewing the bone from above, a reduction in strain concentration at the front of the bone is observed compared to the bone without a growth plate. However, some deformation remains at the front of the bone and between the two tibial plateaus.

Figures 3.23(b) and 3.23(c) depict the effective strain distribution in 11D bone with the addition of a growth plate layer possessing Young's moduli of 50 and 500 MPa, respectively. Changing the Young's modulus of the growth plate significantly alters the bone's deformation behavior in the four studied areas, indicating a greater sensitivity to mechanical properties of the growth plate in young bones compared to old bones.

Young bone - 14D

To obtain a more in-depth analysis of the two particular cases that were spotted in the young bones, the 11D young bone was also analyzed when a layer of growth plate was added.

Figure 3.24(a) depicts the distribution of effective strain within 14D bone when a growth plate layer possessing a Young's modulus of 5 MPa has been added. The growth plate layer undergoes significant deformations due to its Young's modulus being $5,000$ times lower than that of the bone. Nevertheless, other parts of the bone also exhibit considerable deformations in these simulations. Specifically, the depression between the two tibial plateaus is subject to considerable deformation. Additionally, the metaphyseal part of the bone seems to deform more than when the growth plate was absent.

Figures 3.24(b) and 3.24(c) illustrate the effective strain distribution within the 14D bone sample with growth plate layers having Young's moduli of 50 and 500 MPa, respectively. Changing the Young's modulus of the growth plate significantly alters the bone's deformation behavior, indicating a greater sensitivity to mechanical properties of the growth plate in young bones compared to old bones. Quantitative analysis is therefore required to extract critical insights from these distributions and understand the effects of the mechanical properties of the growth plate on bone behavior. The top-down view of the bone reveals a decrease in effective strain values in the cortical subchondral region as the Young's modulus of the growth plate is increased, as well as in the three other regions studied. The Young's modulus of the growth plate has an impact on young bone's deformations, as this phenomenon was also observed in the other 11D young bone.

Looking at Figure 3.24 as a whole, there is a noticeable heterogeneity in the distribution of effective strain. Specifically, when the Young's modulus of the growth plate is imposed at 5 MPa while looking in the slices view, a concentration of effective strain in the metaphyseal lower left part appears, a phenomenon not observed in the other young bone labeled as 11D. Conversely, when the Young's modulus of the growth plate is imposed at 500 MPa, this localized concentration extends to the right side as well. However, when the Young's modulus of the growth plate is 50 MPa, this kind of strain concentration in the metaphyseal part is not observed.

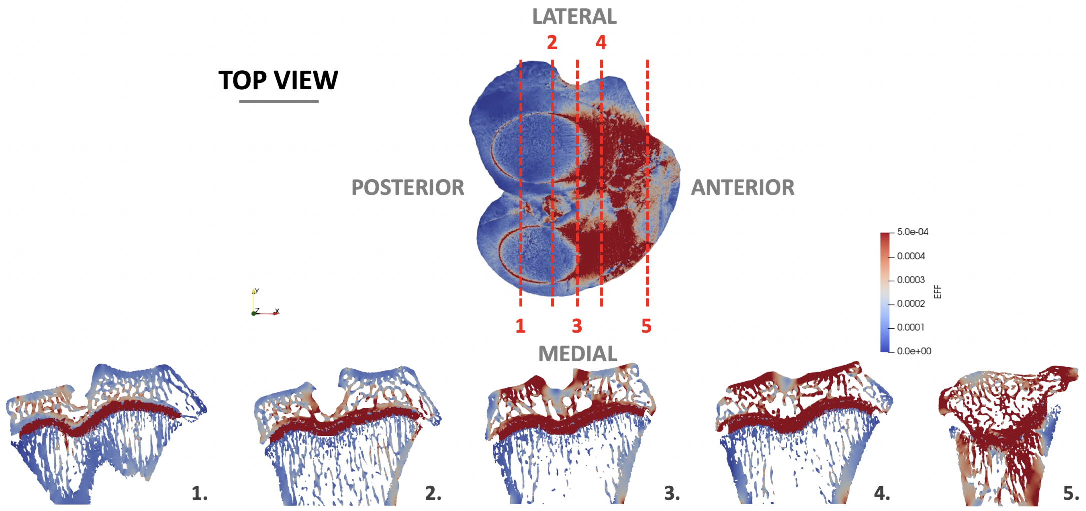

(a) With growth plate (E = 5 MPa)

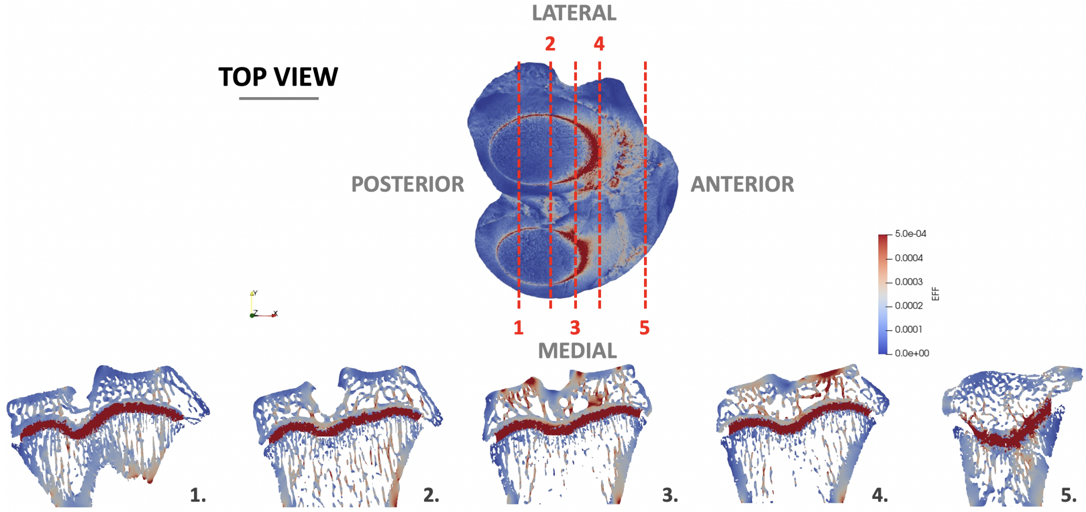

(b) With growth plate (E = 50 MPa)

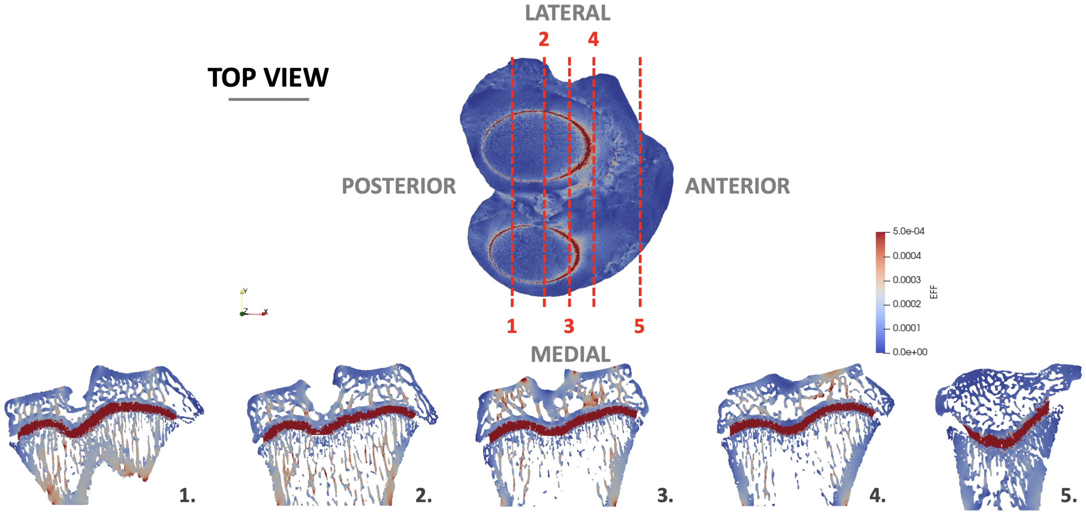

(c) With growth plate (E = 500 MPa)

Figure 3.23: Illustration of the distribution of the effective strain throughout the entire young bone 11D, along with five cross-sectional slices, while adding growth plate with a Young's modulus of (a) 5, (b) 50, and (c) 500 MPa. Each slice is numbered for reference from 1 to 5.

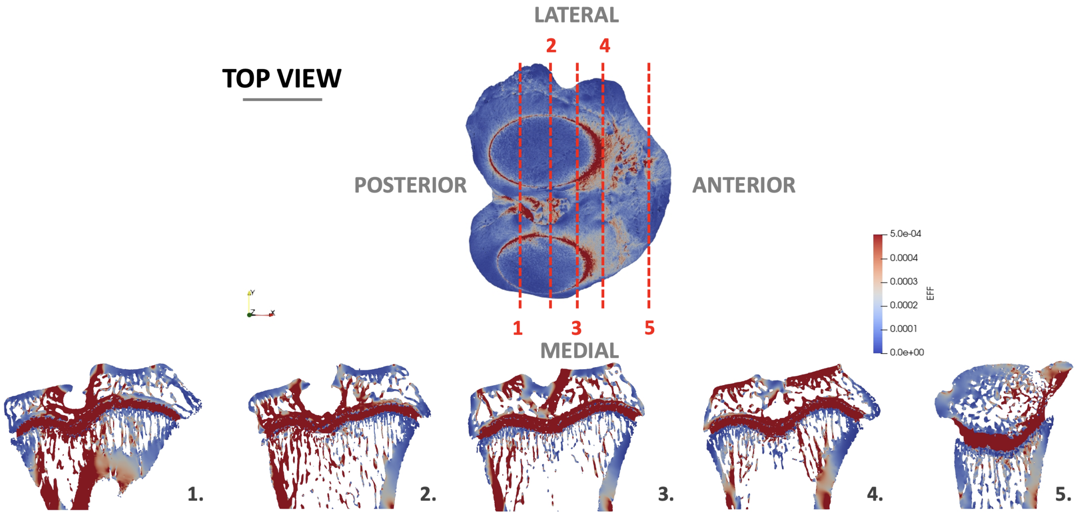

(a) With growth plate (E = 5 MPa)

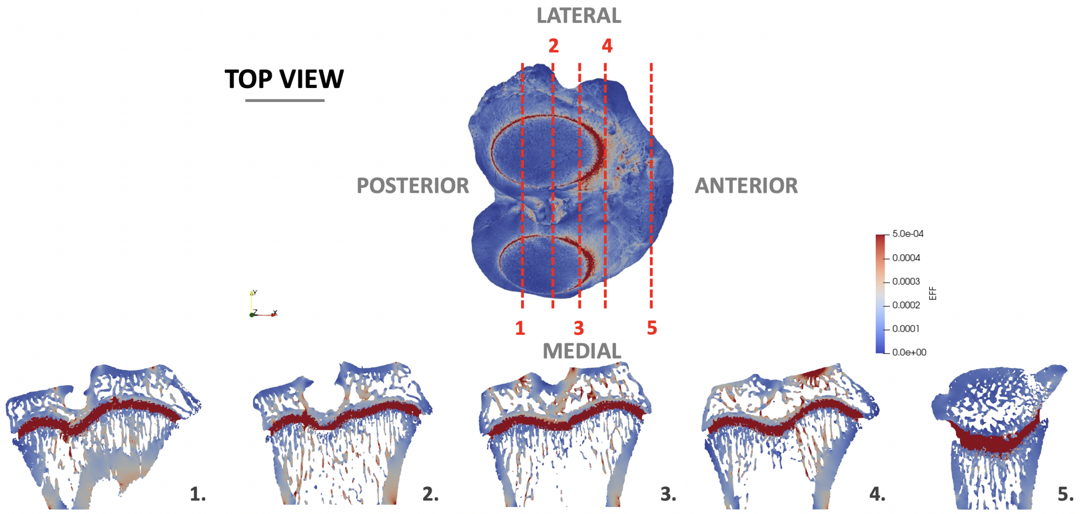

(b) With growth plate (E = 50 MPa)

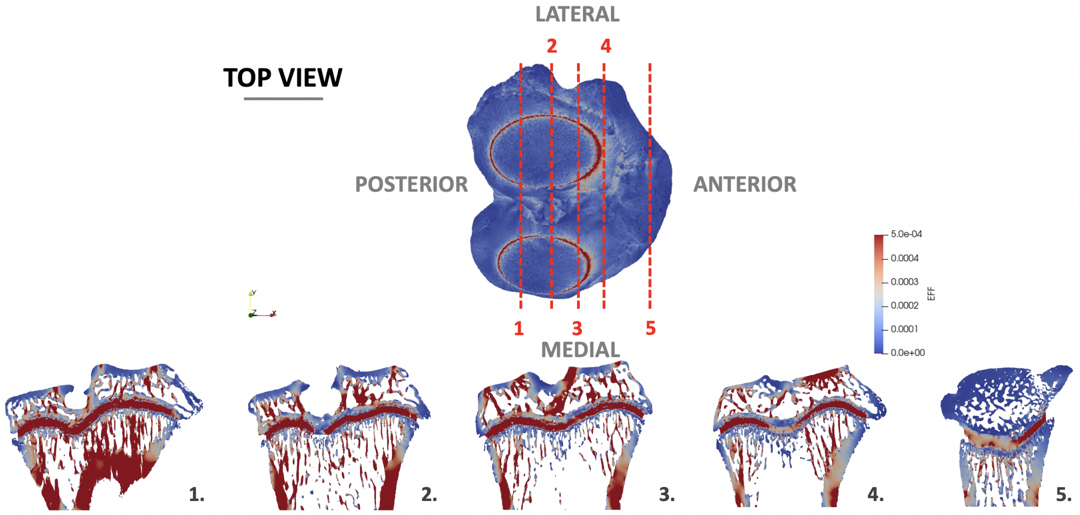

(c) With growth plate (E = 500 MPa)

Figure 3.24: Illustration of the distribution of the effective strain throughout the entire young bone 14D, along with five cross-sectional slices, while adding growth plate with a Young's modulus of (a) 5, (b) 50, and (c) 500 MPa. Each slice is numbered for reference from 1 to 5.

3.1.4.2 Quantitative visualization

Since the full characteristics of the effective strain distribution within the bone cannot be captured by qualitative analysis alone, a quantitative analysis is necessary to quantify changes due to the addition of the growth plate. For this purpose, the mean and Full Width at Half-Maximum (FWHM) will be studied for each effective strain (EFF) distribution in the four areas. Moreover, the significance of the results will be tested with a one-way ANOVA test instead of a t-test as previously since more than two categories need to be compared. This approach will allow a comprehensive understanding of how the different Young's modulus values of the growth plate influence the mechanics and the deformation behavior of the bones, according to their ages.

Old bone - 1VD

Figure 3.25 illustrates the average effective strain of the old bone sample, labeled as 1VD, both without and with the addition of the growth plate, with different values of Young's modulus. Generally, the bone without the growth plate exhibits less deformation compared to when the growth plate is added to bind the subchondral to the metaphyseal part. The difference in the mean effective strain with and without the growth plate is significant across all four studied regions.

Regarding the influence of the material properties of growth plate on the mechanics of bone, it is observed that bone with growth plate having the lowest Young's modulus deforms the most, with an exception in the subchondral trabecular region where a not significant difference was found between the Young's modulus of 50 and of 500 MPa. At first glance, this difference in deformation may not seem substantial. Nevertheless, a one-way ANOVA test performed on these mean effective strains for different values of Young's modulus for growth plate shows that all the differences are statistically significant, with the exception of the difference between 50 and 500 MPa Young's modulus for growth plate in the trabecular subchondral part.

Although there is a noticeable difference between all simulations, this deviation is particularly marked when a growth plate is added. Indeed, less deformation is observed in all regions. The differences induced when Young's modulus is modified are less significant, although still significant, with these deformations decreasing as Young's modulus increases.

Figure 3.26 shows the Full Width at Half-Maximum (FWHM) of the effective strain distribution of old bone 1VD with and without growth plate. In general, the FWHM of the effective strain distribution without a growth plate is lower than when a growth plate is added, indicating better uniformity of the strain distribution within each studied region. This difference is greater in the trabecular regions of the bone, indicating a higher influence of growth plate addition on dispersity in these bone regions.

With regard to the differences induced by a change in the Young's modulus of the growth plate, all the areas do not follow the same trend concerning the influence of a change in the Young's modulus of the growth plate on the evolution of the FWHM of the effective strain distribution. Indeed, for the cortical metaphyseal, trabecular metaphyseal and trabecular subchondral parts, increasing the Young's modulus of the growth plate reduces the dispersity of the effective strain distribution in these three regions. In the subchondral cortical region, on the other hand, an increase in the Young's modulus of the growth plate tends to increase the FWHM of the effective strain distribution, although a decrease is observed when moving from 5 to 50 MPa. This part

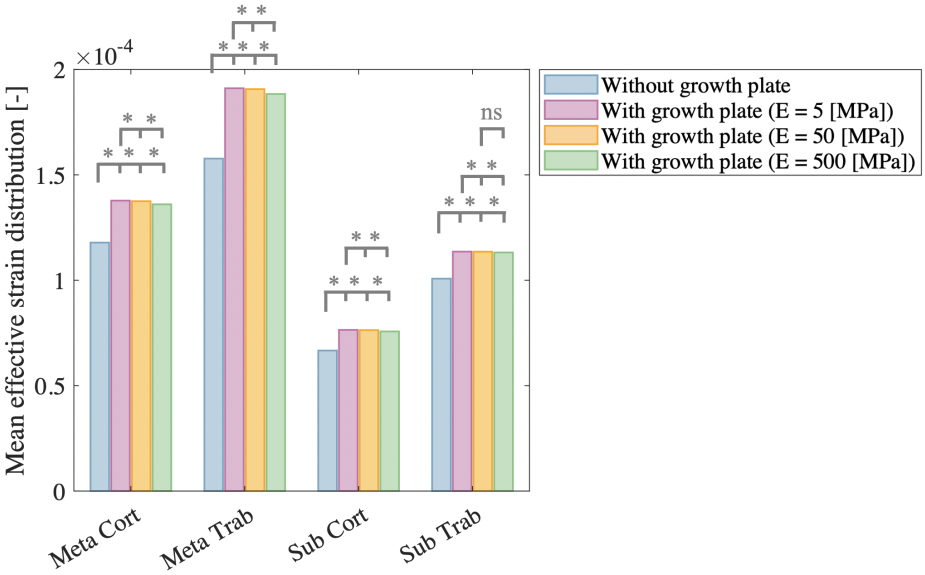

Figure 3.25: Bar plot illustrating the mean of the effective strain distribution for the old bones named as 1VD with different values of Young's moduli for the layer of the growth plate, i.e. 5, 50, and 500 MPa, in the four different delimited areas with their error bars. The Young's modulus of bone is the same as young bone, i.e. 25.5325 GPa. Meta Cort stands for the metaphyseal cortical area, Meta Trab stands for the metaphyseal trabecular area, Sub Cort stands for the subchondral cortical area, and Sub Trab stands for the subchondral trabecular area. '*' means $p < 0.05$ and 'ns' stands for not significant.

of the bone therefore seems more subject to variability when changing the material properties of the growth plate.

Young bone - 11D

Figure 3.27 depicts the mean effective strain distribution in the bone sample labeled as 11D, both with and without the addition of a growth plate. The mean values of the effective strain distribution are presented for the three different values imposed for the Young's modulus of growth plate in the four areas.

When a layer of growth plate is added, the overall trend remains consistent across most regions of the bone, except for the metaphyseal trabecular part. In this specific region, the addition of a growth plate results in an increase in the mean effective strain. In contrast, in the other three parts of the bone, the addition of a growth plate induces a decrease in the mean effective strain. This decrease is particularly pronounced in the subchondral part of the bone, with a significant reduction compared to that observed in the metaphyseal cortical part.

Regarding the influence of material properties on the mechanics of bone, an increase in Young's modulus generally induces a decrease in the mean effective strain, with the exception of the trabecular metaphyseal region. This reduction is particularly pronounced in the subchondral part of the bone compared to the metaphyseal cortical part, despite being statistically significant in the three regions. Conversely, the opposite phenomenon is observed in the trabecular metaphyseal part, with an increase in the value of the mean effective strain distribution while increasing the Young's modulus value. However, this increase is not significant when Young's modulus is increased from 50 to 500 MPa in this region of the bone.

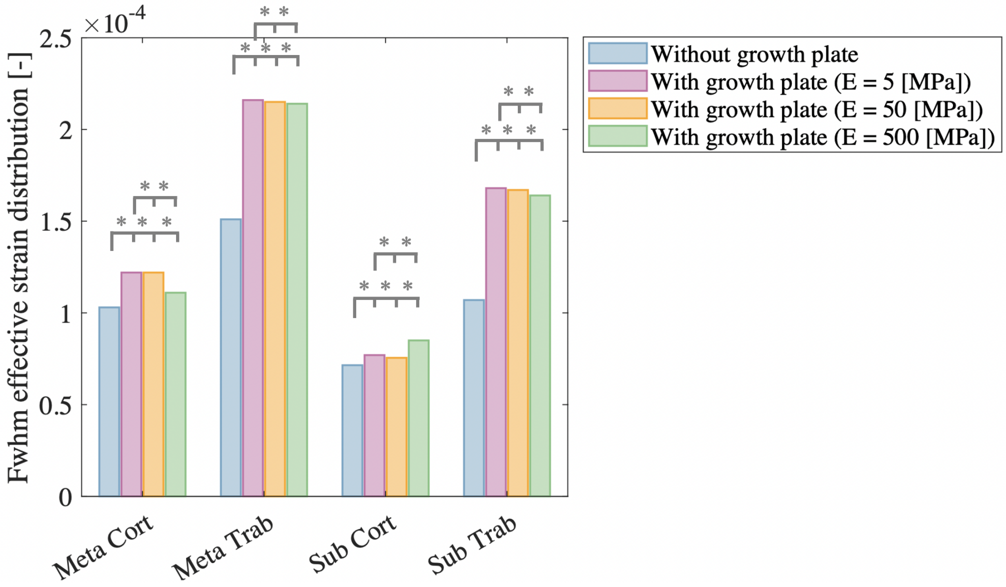

Figure 3.26: Bar plot illustrating the Full Width at Half-Maximum (FWHM) of the effective strain distribution for the old bones named as 1VD with different values of Young's moduli for the layer of the growth plate, i.e. 5, 50, and 500 MPa, in the four different delimited areas with their error bars. The Young's modulus of bone is the same as young bone, i.e. 25.5325 GPa. Meta Cort stands for the metaphyseal cortical area, Meta Trab stands for the metaphyseal trabecular area, Sub Cort stands for the subchondral cortical area, and Sub Trab stands for the subchondral trabecular area. '*' means $p < 0.05$ and 'ns' stands for not significant.

Figure 3.28 illustrates the Full Width at Half-Maximum (FWHM) of the effective strain distribution present in bone labeled as 11D, both with and without the presence of growth plate. Two distinct trends emerge from this figure.

Firstly, in the subchondral region of the bone, the addition of a growth plate induces a noticeable decrease in the FWHM of the effective strain distribution, indicating a lower strain dispersity. This effect aligns with previous observations of reduced concentrations of high effective strain in this region when a growth plate is present. Secondly, in the metaphyseal part, the addition of a growth plate results in a higher heterogeneity of the effective strain distribution. While the impact of the added growth plate on the FWHM is less pronounced in the metaphyseal region compared to the subchondral region, it still remains significant.

Regarding the impact of growth plate material properties on the mechanics of bone, two distinct trends can be observed. On the one hand, in the subchondral part, the increase in the Young's modulus of the growth plate induces a decrease in the FWHM value of the effective strain distribution, indicating reduced dispersity. This reflects a lower presence of high concentrations of effective strain in the subchondral region. Although this effect is less pronounced when the Young's modulus of the growth plate is increased from 50 to 500 MPa in the trabecular subchondral part, it remains statistically significant. On the other hand, in the metaphyseal part, the opposite phenomenon is observed. Indeed, the FWHM value increases with rising Young's modulus of the growth plate, indicating greater dispersity of effective strain. The exception to this trend is observed between 50 and 500 MPa in the cortical metaphyseal part, where the change in FWHM is not significant.

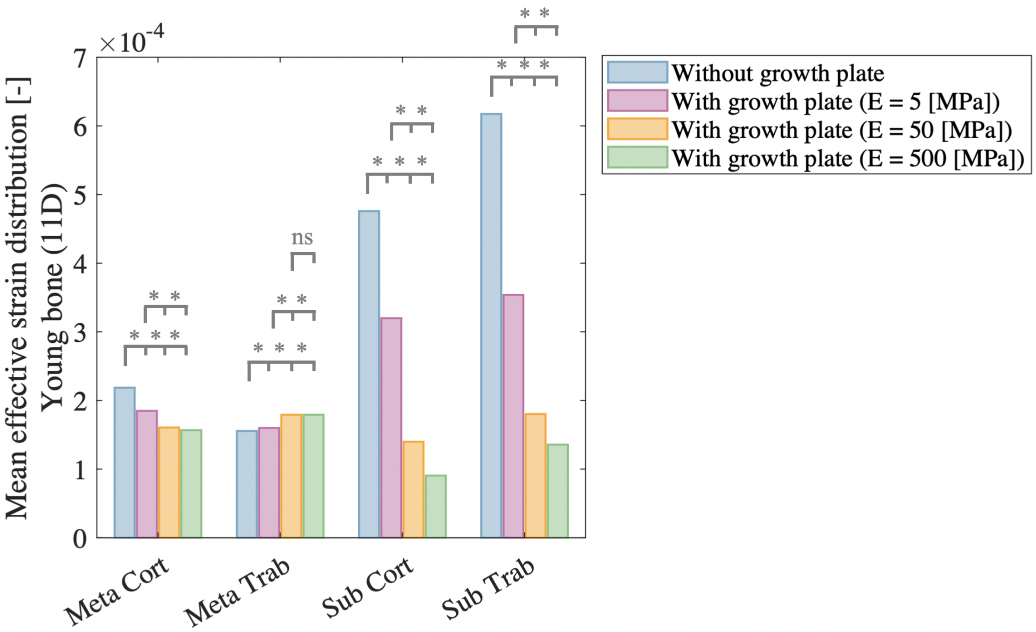

Figure 3.27: Bar plot illustrating the mean of the effective strain distribution for the old bones named as 11D with different values of Young's moduli for the growth plate layer, i.e. 5, 50, and 500 MPa, in the four different delimited areas with their error bars. Meta Cort stands for the metaphyseal cortical area, Meta Trab stands for the metaphyseal trabecular area, Sub Cort stands for the subchondral cortical area, and Sub Trab stands for the subchondral trabecular area. '*' means p < 0.05 and 'ns' stands for not significant.

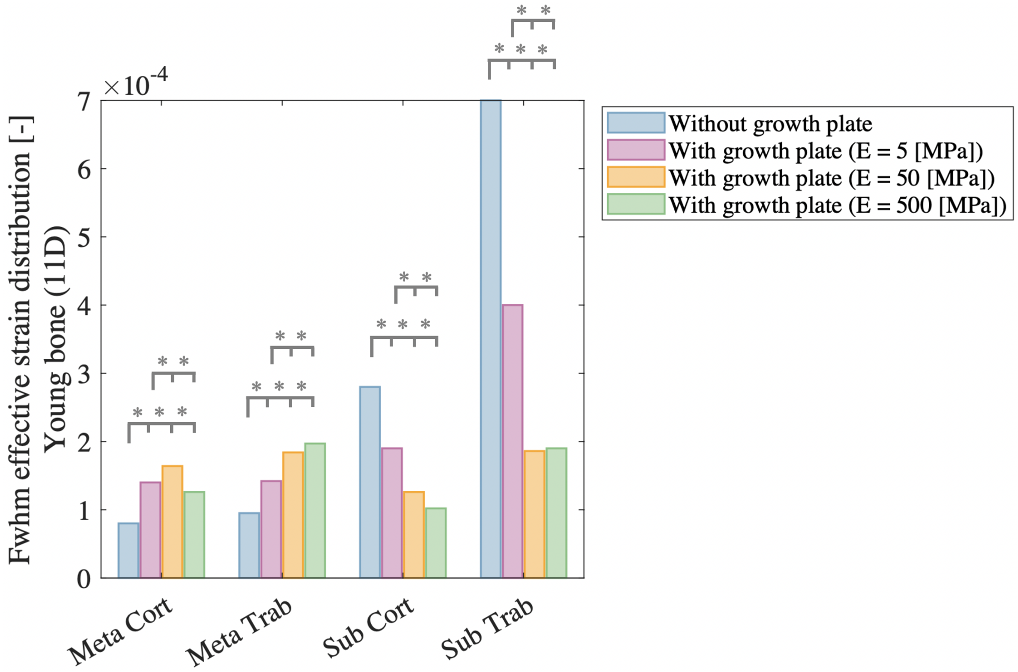

Figure 3.28: Bar plot illustrating the Full Width at Half-Maximum (FWHM) of the effective strain distribution for the young bones named as 11D with different values of Young's moduli for the layer of the growth plate, i.e. 5, 50, and 500 MPa, in the four different delimited areas with their error bars. Meta Cort stands for the metaphyseal cortical area, Meta Trab stands for the metaphyseal trabecular area, Sub Cort stands for the subchondral cortical area, and Sub Trab stands for the subchondral trabecular area.
'*' means p < 0.05.

Young bone - 14D

Figure 3.29 presents the mean effective strain distribution of the young bone sample, designated as 14D with and without growth plate. The averages of the effective strain distribution are displayed for various values of Young's modulus applied to the growth plate.

As qualitatively stated, the resulting comportment is very distinctive from those obtained with the other young bone labeled as 11D. Firstly, in the cortical parts, the addition of a growth plate generally reduces the mean effective strain distribution, indicating less deformation in these regions. However, this reduction is observed up to a specific Young's modulus value for the growth plate in the metaphyseal cortical region. Specifically, the deformation induced by the addition of a growth plate with a Young's modulus imposed at 5 MPa is less than without a growth plate. However, when the Young's modulus of the growth plate exceeds 50 MPa, the deformation induced in the cortical metaphyseal region surpasses that observed without the growth plate. This trend is not present in the subchondral cortical region, where an increase in the Young's modulus of the growth plate consistently results in decreased deformations.

Regarding the influence of the material properties of the growth plate on the mechanical behavior of bone, a clear trend is not consistently observed. As the Young's modulus of the growth plate increases, deformation in the metaphyseal cortical part of the bone also increases. This is logical, as the addition of a growth plate allows deformation occurring in the subchondral part to propagate into the metaphyseal part.

Secondly, in the trabecular parts, the addition of a growth plate generally induces an increase in bone deformation in these areas. However, this increase does not hold when the growth plate has a Young's modulus of 500 MPa in the trabecular subchondral part, where deformation is less than that observed without the growth plate.

In the trabecular metaphyseal part, increasing the Young's modulus initially increases the mean effective strain distribution, but only up to a certain Young's modulus value. Beyond a Young's modulus value of 50 MPa, the induced strain decreases. In the cortical subchondral and trabecular subchondral parts, the induced strain decreases as Young's modulus increases.

Figure 3.30 illustrates the Full Width at Half-Maximum of the effective strain distribution in the young bone sample, labeled 14D, with and without a growth plate. Generally, the FWHM of the effective strain distribution of bone without the addition of a growth plate is lower than when a growth plate is added, indicating a more concentrated strain distribution. However, this difference is less pronounced in the cortical parts, which appear to be less influenced by the presence or absence of a growth plate. Nevertheless, a significant difference is always found when comparing each bone part when a growth plate is added.

Regarding the influence of material properties on the FWHM of the effective strain distribution, it was observed that bone with a growth plate having a Young's modulus of 50 MPa exhibited the highest dispersity. In the cortical areas, bone with a growth plate characterized by a Young's modulus of 500 MPa showed the lowest dispersity, compared to bone with a growth plate having a Young's modulus of 5 MPa. The opposite trend is observed in the trabecular parts of the bone, where the lowest dispersity was found in the bone with a growth plate possessing a Young's modulus of 5 MPa. Therefore, no clear relationship can be established between an increase in Young's modulus and the FWHM value of the effective strain distribution.

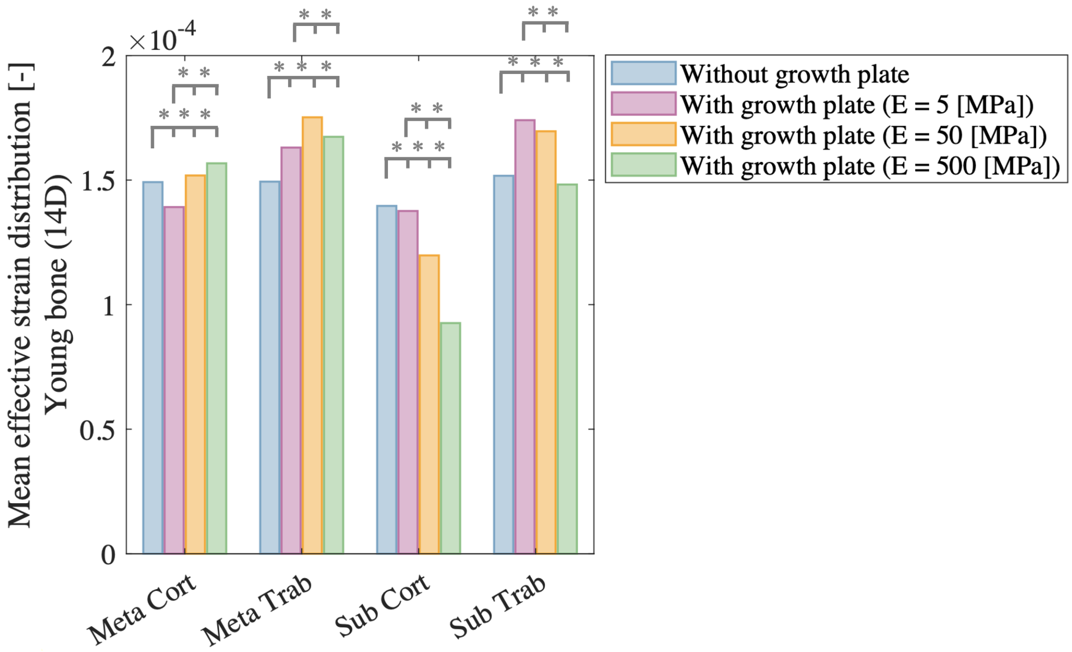

Figure 3.29: Bar plot illustrating the mean of the effective strain distribution for the old bones named as 14D with different values of Young's moduli for the layer of the growth plate, i.e. 5, 50, and 500 MPa, in the four different delimited areas with their error bars. Meta Cort stands for the metaphyseal cortical area, Meta Trab stands for the metaphyseal trabecular area, Sub Cort stands for the subchondral cortical area, and Sub Trab stands for the subchondral trabecular area.
'*' means $p < 0.05$.

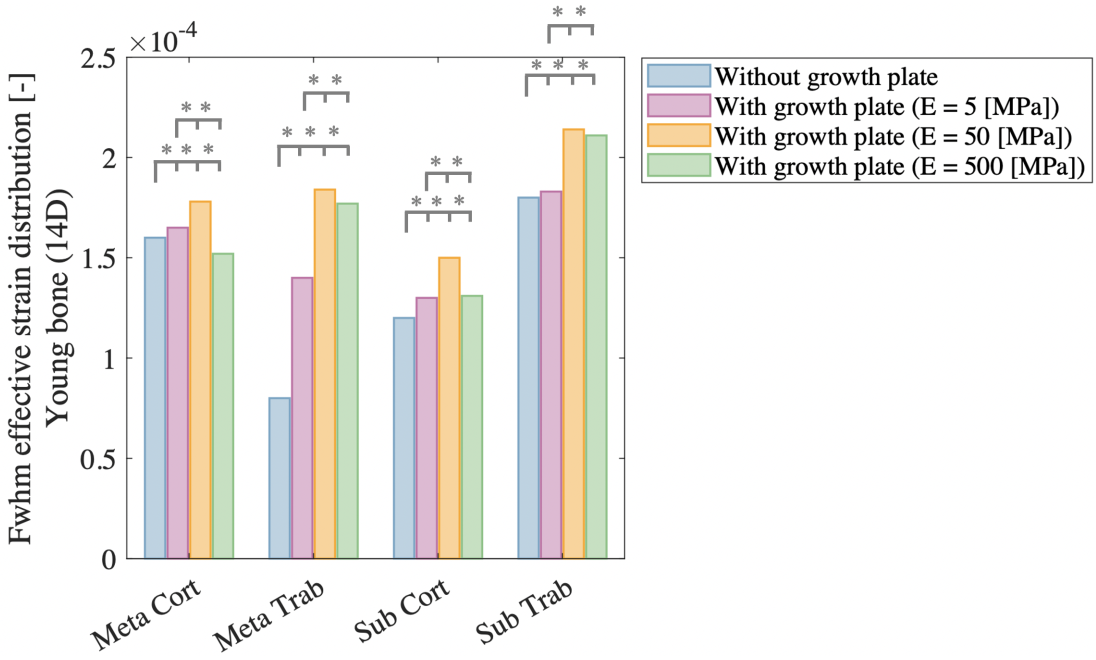

Figure 3.30: Bar plot illustrating the Full Width at Half-Maximum (FWHM) of the effective strain distribution for the young bones named as 14D with different values of Young's moduli for the layer of the growth plate, i.e. 5, 50, and 500 MPa, in the four different delimited areas with their error bars. Meta Cort stands for the metaphyseal cortical area, Meta Trab stands for the metaphyseal trabecular area, Sub Cort stands for the subchondral cortical area, and Sub Trab stands for the subchondral trabecular area.

In conclusion, the addition of a growth plate layer leads to distinct behaviors between young and old bones. Although old bones exhibit relatively consistent mechanical behavior, the significant inter-sample variation in the effective strain distribution among young bones results in markedly different mechanical responses depending on the sample studied.

3.2 Experimental part

To conclude this chapter, an experimental analysis was conducted. Compression tests were performed at a strain rate of 1 mm/min on samples of whole legs, as well as on isolated tibia samples.

3.2.1 Entire lower limb compression

Figure 3.31 illustrates the average force-displacement curves for samples of entire lower limbs from both 3-month-old and 1-month-old specimens. The two curves exhibit a 'J-shape', indicating initially a significant deformation, for a small force application, followed by a sharp increase in force over a small displacement. This 'J-shape' curve is characteristic of soft tissue compression curves, which typically consist of four distinct phases. At the beginning, there is the toe region, characterized by high deformation at low stress. Then, the heel region appears where displacement increases non-linearly with applied force. Next, the linear region emerges, marked by a linear relationship between induced displacement and applied force. Finally, the breaking phase appears [95, 96].

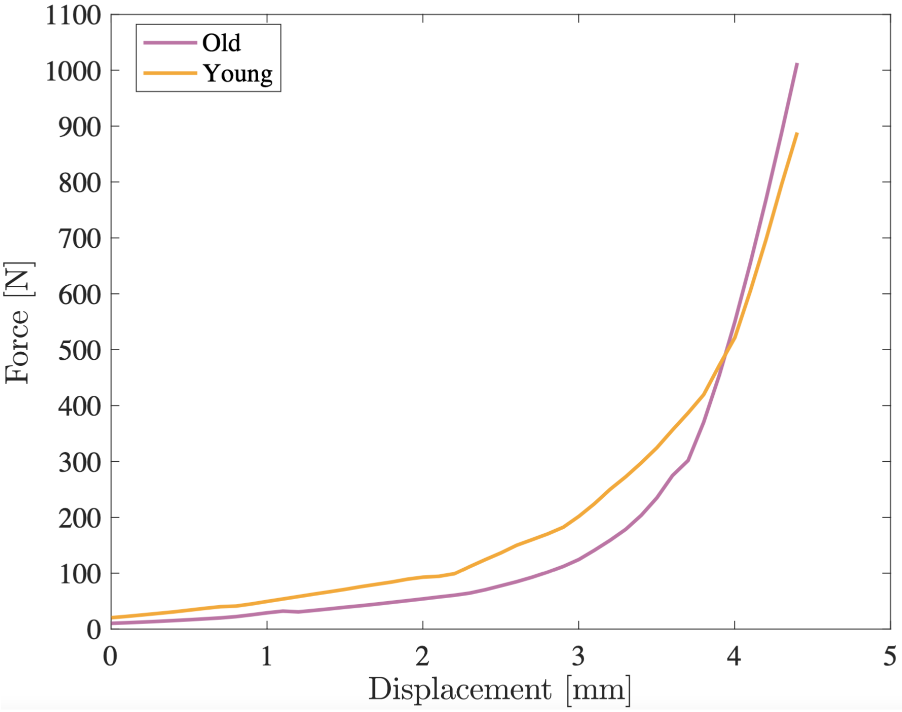

Figure 3.31: Mean of load-displacement curves for 3-month-old and 1-month-old bone samples under compression.

Compared to the force previously applied in simulations of 40 N, this corresponds to the toe phase of the curve, where there is a significant increase in displacement at low applied loads.

3.2.2 Tibial compression

Since the simulations did not account for the soft tissue surrounding the tibia, compression tests in which the tibia is completely exposed are essential.

Figure 3.32 illustrates the mean load-displacement curves for four tibia bone samples from 2-month-old rats, along with ± standard deviation illustrated by a shaded area. When the tibia is isolated without soft tissues surrounding it, the force-displacement curves exhibit a distinct behavior compared to when the entire lower limb was tested. Specifically, the force values in this case are significantly lower than before, and the shape of the curve undergoes a complete change.

Initially, a first elastic linear phase appears, where force increases linearly with displacement. Following this, a plateau region occurs where displacement increases without a corresponding increase in force. In the final part of the curve, a densification region is observed where deformation increases non-linearly with the applied force, ultimately leading to bone fracture.

The force applied in the simulations, 40 N, corresponds to the linear elastic phase observed in the compression tests of the tibia bone.

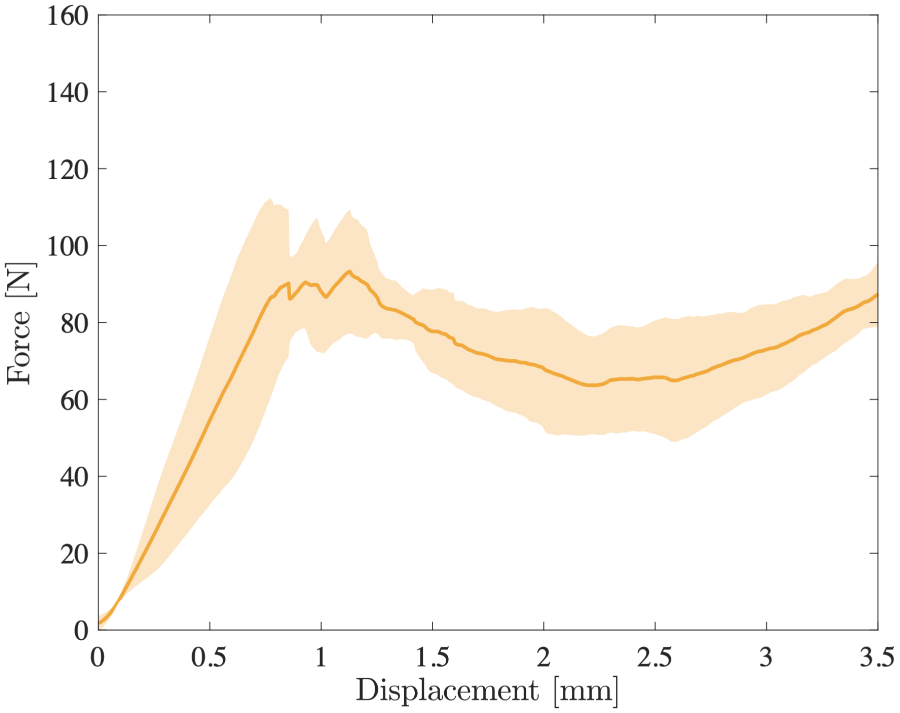

Figure 3.32: Mean of load-displacement curves for young (2-month-old) bone samples under compression. The shaded area corresponds to ± the standard deviation of the curves.

Chapter 4

Discussions

In the present chapter, the results obtained from the previous section will be discussed and interpreted thanks to a clear comparison with existing literature.

The discussion will begin with a detailed examination of the apparent stiffness results obtained for both lateral and medial plates. This will be followed by a discussion about the influence of material properties on the mechanical behavior of bone. Subsequently, the impact of microstructure on bone mechanics will be assessed, with a focus on the role of struts in influencing mechanics. The discussion will then address the results related to maximum and minimum principal element strain, providing insights into the anisotropic behavior of bone. To conclude the simulation's discussion, an in-depth analysis of the impact of the growth plate on bone mechanics will be carried out. The final discussion concerns the results obtained experimentally, with a comparison of the experimental results to those obtained from simulations, identifying and explaining any discrepancies between the two sets of findings.

4.1 Tibial apparent stiffness

The reported higher apparent stiffness values for old bones compared to young bone in the medial and lateral plateaus are consistent with findings from previous studies, such as those reported by *Patton et Al.* [97]. This specific study has shown that older bones tend to deform less than younger bones, which aligns with the differences in apparent stiffness between young and old samples. Specifically, the apparent stiffness for older bones was found to be greater than the one in young bones, indicating a greater resistance to deformations.

Several factors can contribute to this increase in apparent stiffness with age. Firstly, as bones age, bone tends to accumulate a greater amount of mineral content, leading to denser and stiffer tissue. Secondly, the amount of collagen present in bone begins to decrease, leading to a reduction in bone flexibility. These two factors are simulated in μ-finite elements processes with different Young's moduli. Another significant factor is the change in bone microstructure with aging. Younger bone typically has fewer cross-links between the subchondral and metaphyseal parts, leading to a reduction in apparent stiffness. In the absence of these struts, the subchondral part of the bone can more easily approach the metaphyseal part when a force is applied, as there is less resistance to deformations. Finally, the presence of larger, more widely spaced struts also has an impact on the bone's ability to deform.

Furthermore, the observations made by *L. Müller et Al.* that older bones have a significantly greater plateau thickness compared to the one of young bones [98] further support this adaptive mechanism. The thickening of the plateaus contributes to their increased apparent stiffness since a thicker plateau can resist deformation more effectively. Those types of adaptive responses are the way nature compensates for the reduced flexibility and increased brittleness which appears while aging.

Nevertheless, this increase in apparent stiffness in old bone makes it more brittle and, therefore, more susceptible to fractures [99]. This brittleness underscores the importance of adequate calcium and vitamin D intake in older adults in reducing the risk of fractures [100].

On the other hand, the difference in apparent stiffness between the medial and lateral plateaus in old bones is significantly pronounced, while in young bones, this difference is not significant. This observation suggests that in younger bones, the apparent stiffness distribution between the two plateaus is more homogeneous compared to old bones. Age therefore has a significant impact on the apparent stiffness properties of the two plateaus. This phenomenon can be explained by a structural degradation with age, which is driven by cellular events. This degradation leads to an apparent stiffness discrepancy between the two plateaus, depending on the loading conditions experienced by each plateau. The medial plateau is the most affected by osteoarthritis according to the literature [101, 102], which may be directly induced by the difference in apparent stiffness between the two plateaus.

Generally, the lateral plateau exhibits greater apparent stiffness compared to the medial plateau. This difference in apparent stiffness can be attributed to several factors related to the bone's structure and density. Particularly, in the medial region, higher trabecular bone density is typically observed, along with more aligned trabeculae. moreover, the medial plateau tends to have a greater thickness in both young and old bones, as studied by *L. Müller* previously [98]. These observations underscore the complex interplay between bone density, bone structure alignment, and thickness in the determination of the bone's properties.

4.2 Material properties analysis

Young's modulus was shown to have an impact on bone mechanics. The findings consistently show that higher Young's modulus values correlate with smaller effective strains within the bone. This is intuitive, since by imposing a higher value of Young's modulus, the bone becomes stiffer and therefore has inherently less tendency to deform compared to a material with a lower Young's modulus.

Although these differences in deformation might not be immediately apparent on the strain maps, introducing the mean of the effective strain distribution reveals significant differences between simulations with varying Young's modulus values. This suggests that the mechanical properties of bone will therefore significantly influence the mean effective strain within the tissue.

Although this impact of Young's modulus is significant in all the regions studied, it is less pronounced in the cortical parts than in the trabecular parts. This can be attributed to the density differences between these bone types. Cortical bone is denser and thicker, making it less affected by variations in material properties, whereas trabecular bone is more porous and therefore more easily sensitive to variations in material properties. These results align well with previous researches [103, 104, 105].

Concerning the Full Width at Half-Maximum (FWHM) analysis, a significant difference was revealed in the metaphyseal cortical and subchondral trabecular regions when the material stiffness changes. This different sensitivity can be attributed to the structural and compositional differences in these regions.

This analysis highlights the importance of considering regional variations within the bone, and not the bone as a whole when studying the impact of material properties on bone mechanics.

4.3 Microstructural analysis

Imposing a constant Young's modulus across both young and old samples enabled us to isolate and evaluate the impact of microstructure on bone mechanics.

In older bones, the trabecular region demonstrates greater deformation compared to the cortical region. This can be easily explained by its higher porosity and lower density. This structural difference underscores its reduced ability to withstand mechanical stresses and strains. The pronounced deformations observed within the metaphyseal bone further highlight the critical influence of microstructural variations. It is this microstructure that enables the subchondral bone to undergo less deformation than the metaphyseal bone. The higher deformation of the trabecular bone in the metaphyseal part compared to the subchondral part can be explained by a lower BT/TV in the metaphyseal part (trabecular bone volume per amount of tissue volume), accompanied by thinner, more widely spaced trabeculae [98]. These findings emphasize the critical role of bone microstructure in influencing the distribution of effective strain following external force application.

Looking at slices with and without struts in old bones highlights that all four areas undergo greater deformation when a large number of struts are present. This is logical, as these struts facilitate the transmission of deformation to the metaphyseal zone. Nevertheless, the results obtained should be treated with caution, however, as it is not only the presence or absence of strut that influences the results obtained between the selected slices. The microstructure in the subchondral and metaphyseal areas also varies. Additionally, considering the large standard deviation, there is significant variability within the same region (see Appendix D.1.2), indicating considerable intra-regional variability.

In young bones, a greater degree of deformation was observed compared to old bones, especially in the subchondral region. This notable increase in deformation can be attributed to the significantly different displacements applied to young and old bones. Indeed, the displacements required to obtain a force of 40 N in young bones are considerably larger than those in old bones (refer to Figure 2.9). Since the solid displacement is exclusively imposed on the subchondral part, the induced deformation struggles to propagate to other parts of the bone, given the decreased amount of bridges in young bones compared to old bones.

A change in behavior was observed in the young bones, with two main patterns emerging. This variability is likely attributed to the high sample-dependent variability in young bones (refer to Appendix C.3), due to variations in density and position of struts within the structure. The majority of young bones (n = 4) exhibited a broad effective strain distribution in the subchondral region, skewed towards higher values, indicating a significant concentration of deformation in this part of the bone. Conversely, a minority of young bones (n = 2) displayed an effective strain distribution close to that observed in older bones. The variability in young bones is a well-known and previously studied characteristic, as noted in previous studies [106, 107, 108]. These changes in the distribution of effective strain could be attributed to differences in the rearing conditions of the rats, the disparity in the number and position of struts, as well as variations in growth rates. Specifically, the two bones with strain distributions similar to those of aged bones may correspond to rats experiencing accelerated growth compared to the others. This change in behavior in relation to other bones needs to be investigated to determine whether this deviation in strain distribution correlates with increased susceptibility to pathology such as osteoarthritis in adulthood.

The fact that this behavioral change is only visualized in the subchondral region of young bones can be attributed to the absence of struts. Without these structural bridges, deformations are confined to the subchondral part without being transmitted to the metaphyseal region. In contrast, this transmission of deformation is permissible in old bones, since the presence of struts in the structure facilitates transmission of deformation throughout the bone structure. This impact of the presence or absence of struts to connect the two studied regions can also be visualized qualitatively. In old bone, numerous bridges are present to connect these regions, facilitating an optimal force transmission, and consequently deformations, from the subchondral to the metaphyseal part. In contrast, young bones have fewer struts connecting these areas. With fewer or no struts, deformation imposed in the subchondral region does not extend to the metaphyseal part, as no structural bridges are present to facilitate this transmission. Nevertheless, when struts are present, as seen at the front of the bone labeled 11D, deformation propagation is permitted.

As demonstrated by the study conducted by *Staines et Al.* [55], the presence of these bridges in old bone has a direct impact on the localization of high local Von Mises stresses. Although rats do not exhibit growth plate closure, this phenomenon occurs in humans and is accompanied by a marked increase in the number and density of struts. This increase in number and density is also remarkable in rat bones. As the bone ages, these bridges in the growth plate will either fracture and/or redistribute strains in the vicinity of the growth plate. During growth, certain stresses can be induced, generating tension in these struts, which could contribute to the termination of growth near the growth plate [55]. This increase in struts with aging has been shown to induce smaller deformations, as higher stresses near the growth plate have been identified. This phenomenon was also observed in this study.

Looking at slices with and without struts in young bones highlights that the presence or absence of struts significantly influences the behavior of an isolated bone slice. Indeed, the general trend observed across the three bones studied (one old bone and two young bones) is consistent, leaving no significant differences between old and young samples. However, these observations should be considered with caution, as variations in bone microstructure across different slices can also significantly impact the distribution of effective strains.

A comparison of young and old bones revealed a tendency towards greater deformation in young bones, suggesting that their microstructure is more prone to deformation compared to older bones. This increased deformability in young bones can also be explained by the fact that older bones are subjected to heavier loads over time. In response to these heavier loads, bones adapt their microstructure to minimize deformation, thereby reducing the risk of fracture and maintaining their functional integrity [109, 81, 110, 111]. This increase in the number of struts in the structure highlights the aging process's ability to adapt to the application of greater forces while maintaining bone's primary functions.

As shown by *L. Müller* [98], the metaphyseal part, while less dense, exhibits more aligned bone structures, to optimally sustain the compressive forces applied to it in the same direction as its alignment. Although this region is less dense, the alignment of bone structures effectively limits deformations, with the trabecular area sustaining more deformation compared to the subchondral region. As bones age, their density decreases and the bone network becomes coarser, particularly in the metaphyseal region. Conversely, in the subchondral region, bone structures tend to orient themselves, and the degree of anisotropy increases in the metaphyseal part as the bone ages. These microstructural changes with aging likely explain the tendency of older bone to be less deformed than younger bone.

To conclude, this deformation behavior is strongly influenced by the presence or absence of structural bridges between the subchondral and metaphyseal regions. In older bones, these types of struts are abundant, allowing deformation to be distributed more evenly throughout the entire bone. Conversely, in young bones, such bridges are present in minimal quantities. The aging process present in bone enables its microstructure to adapt to the applied loads, to best meet the bone's primary functions.

4.4 Maximum and minimum principal element strain

The analysis of the principal maximum and minimum element strain provided insight into the deformation behavior of bone. In older bones, a pronounced tendency towards greater deformation under compression was observed, particularly in the trabecular region. This tendency is exacerbated by the lower density of trabecular bone, making it more susceptible to compressive forces. Trabecular bone, being easier to deform in compression than in tension, exhibits a clear anisotropy, which is also present, though to a lesser extent, in the cortical part of the subchondral bone. In contrast, this anisotropy is less pronounced in young bone, which tends to deform similarly in tension and compression. This difference can be attributed to the findings of *L. Müller*'s study [98], which indicates that bone structures in older bone tend to orient more along the bone axis in the subchondral region, giving a more pronounced anisotropy with age. This age-related anisotropy was also identified in the study made by *A. Ural and D. Vashishth* [112].

Nevertheless, the observed tendency for greater deformation under compression contradicts previous studies, which suggest that bone is generally stronger in compression than in tension [105, 113, 114]. This contradiction is also observed in young bone, where a slight tendency for greater deformation under compression than tension was also noted.

4.5 Growth plate impact

Given the significant influence of the struts present between the subchondral and metaphyseal regions, an in-depth analysis of the influence of the growth plate was undertaken to see its impact on effective strain propagation. This growth plate constitutes a cartilage layer, connecting the subchondral to the metaphyseal region. The Young's modulus values for the growth plate studied were set at 5, 50, and 500 MPa with the first two values corresponding to a healthy growth plate, while the last one represents a pathological condition, simulating abnormal stiffening of this region.

Firstly, in older bones, the growth plate layer appears as the most deformed part of the tissue, indicated by its appearance in red on the strain distribution maps. This observation aligns with expectations, as its Young's modulus is $5,000$ times smaller than that of the surrounding bone, allowing for much greater deformation due to its markedly lower rigidity. Notably, as the Young's modulus of the growth plate increases, there is a corresponding decrease in the effective strain values within the growth plate layer. This behavior is consistent with the mechanical principles, as by increasing the value of Young's modulus, the growth plate is imposed as being more rigid and therefore less susceptible to deformations.

Quantitatively, old bones without growth plate addition exhibit less deformation compared to those where the growth plate is present, binding the subchondral and metaphyseal parts. The difference in the mean effective strain with and without a growth plate is statistically significant across all four studied regions, with the most pronounced difference occurring in the metaphyseal region. This increased deformation in the metaphyseal part with the addition of a growth plate is an unexpected result given the growth plate's ability to capture deformation, suggesting a reduction in deformation in the bone.

In older bones, the influence of the growth plate is less marked compared to its effect on younger bones due to the presence of numerous struts already present thanks to the aging process. The growth plate acts as a bridge between the subchondral and metaphyseal regions, facilitating the even distribution of deformations across the bone.

Among young bones, the overall behavior is more versatile compared to older bones, with behaviors varying from one sample to the other. This change in behavior from one bone to another is mainly explained by the density and position of the struts connecting the subchondral to the metaphyseal part.

In the bone labeled as 11D, which exhibited a high concentration of deformations in the subchondral region, the addition of a growth plate allowed strain to propagate towards the metaphyseal part of the bone, thereby reducing the strain concentration present in the subchondral area. As the Young's modulus of the growth plate increased, the strain concentration in the subchondral part appeared to disappear, leading to higher effective strain in the metaphyseal trabecular region. The higher deformation within the trabecular metaphyseal region indicates a higher tendency to deformation in the trabecular region compared to the cortical one. This phenomenon can be attributed to the general lack of struts connecting the subchondral to the metaphyseal parts in young bones. In the absence of a growth plate, strain cannot effectively propagate between these regions. Indeed, the addition of a growth plate facilitates this strain transmission, particularly as the Young's modulus increases, thereby enhancing the homogenization of effective strains within the bone and reducing strain concentrations. When the Young's modulus of the latter is increased to 500 MPa, mimicking pathological condition, the bone's behavior begins to resemble that of aged bone. This observation suggests that a growth plate with a higher Young's modulus can induce deformation characteristics similar to those found in older bones.

Furthermore, in the metaphyseal part, the addition of a growth plate results in a broader strain distribution, indicating a greater strain dispersity. This can be attributed to the fact that the presence of a growth plate allows for the propagation of effective strain into the metaphyseal part of the bone, which previously experienced limited deformation due to restricted connectivity between the subchondral and metaphyseal regions. Without the presence of a growth plate, deformations induced by the application of force were only concentrated where struts were present, whereas the addition of the growth plate resulted in uniform deformation propagation along the width of the bone, reducing deformation concentrations.

In the bone labeled as 14D, the metaphyseal region seems to deform less than when the growth plate was absent. This decrease in deformation can be attributed to the lack of natural bridges connecting these two parts of the bone, which previously hindered optimal strain propagation. The addition of the growth plate layer acts as a connecting bridge between these two regions, facilitating greater deformation in the metaphyseal area.

However, a top-down view of the bone reveals a decrease in effective strain values in the cortical subchondral region as the Young's modulus of the growth plate increases. This suggests that as the growth plate becomes stiffer, the upper part of the tibia experiences less deformation compared to when the growth plate is softer, i.e. when the Young's modulus of the growth plate is reduced. Interestingly, when the Young's modulus of the cartilage is set to 50 MPa, this kind of strain concentration in the metaphyseal region is not observed, indicating that the growth plate's stiffness significantly affects the strain distribution within the bone. This difference in behavior when changing the material properties of the growth plate can also be explained by the fact that not all the values chosen are physiological.

In the cortical subchondral and trabecular subchondral regions, induced strain decreases as the Young's modulus increases. This behavior aligns with expectations, as a higher Young's modulus in the growth plate allows for more effective propagation of deformations from the subchondral to the metaphyseal region, thereby reducing strain in the subchondral area.

However, it is important to note that in rat bones, complete closure of the growth plate is never observed [59, 115, 116]. This incomplete closure affects the observed mechanical behaviors and deformation patterns, highlighting the need to consider the growth plate when interpreting the results.

4.6 Experimental analysis

To correlate the computational results with real-world observations, an experimental analysis was conducted.

During the compression of the entire leg, a characteristic "J-shape" curve was observed. This 'J-shape' curve is characteristic of soft tissue compression curves, which is expected as the soft tissue surrounding the knee is still present, overshadowing the response of the bone itself. To isolate the bone's mechanical response and avoid the confounding effects of soft tissue, a compression test was subsequently performed on the tibia alone while compromising the alignment with boundary conditions applied in computational simulations. By maintaining the knee intact, the boundary conditions would have been more consistent with those imposed in the μ-finite element simulations, as the actual contact between the bones would have been preserved.

To effectively compare experimental results with those obtained through finite element simulations, compression tests were conducted exclusively on the tibia. The resulting compression curve is characteristic of bone under compression [117, 15, 14]. Notably, the force of 40 N applied in the simulations aligns with the linear elastic phase observed in the experimental tibia compression tests. This alignment not only affirms the validity of the initial assumptions but also underscores their consistency with the experimental observations.

To relate the results obtained experimentally to those obtained through simulations, the displacement required to obtain a force of 40 N can be analyzed. Experimental measurements indicate that a displacement of 0.3809 mm is required to obtain a total force of 40 N. In contrast, simulations reveal that the average displacement required to achieve the same force is 0.0484 mm, with a maximum value of 0.1063 mm. This significant discrepancy between experimental and simulation results can be attributed to several factors. Firstly, numerically, numerous assumptions and simplifications were made, which may have introduced biases in the results. Additionally, the experimental samples were taken from 2-month-old bones, while the computational models used 3-month-old bones. Younger bones require greater displacement to achieve the same force, explaining the larger displacements observed experimentally. These age-related differences, along with the inherent assumptions in the simulation models, further explain the variance in displacement values between the experimental and simulation outcomes.

Chapter 5

Limitations and future work

This final chapter will discuss the limitations of this current study and propose potential future researches to enhance the results obtained. While this work has provided valuable insights, certain material and time constraints, as well as assumptions were made. Understanding the impact of those limitations on the outcomes is essential to refine the methodologies used in this study.

5.1 Limitations

This work, although providing valuable insights into the behavior of a rat tibia when subjected to a force exerted on its two platforms, has certain limitations.

Firstly, the assumption of linear elastic behavior for bone is not entirely accurate. Although the applied displacement falls within the elastic linear part of the stress-strain curve, the actual elastic part of the mechanical behavior of bone is not perfectly linear.

Secondly, a second significant simplification concerning the isotropic behavior of bone was formulated during the simulations. In reality, bones do not behave isotropically but exhibit transverse isotropy, due to their hierarchical architecture at different scales. Indeed, its mechanics vary significantly depending on its orientation. Nevertheless, this hypothesis of isotropy has been frequently formulated in numerous articles for the sake of simplicity [118, 107, 119].

Thirdly, uniform Young's modulus and Poisson's ratio were applied to the whole bone, whereas the known differences between trabecular and cortical bone mechanical properties. Indeed, bone properties are extremely heterogeneous, with the presence of bone patches, due to bone remodeling, and applying identical material properties to the whole bone does not account for these variations.

Fourthly, this study does not incorporate time-dependent processes such as healing or adaptation of bone to the applied forces. The analysis was conducted in a "static" manner, which may lead to biased results. Indeed, bone mechanics are highly dependent on the rate at which force is applied to it. Slower application of force typically results in lower measured values, which are closer to the actual properties of the bone [120, 121].

Fifthly, the use of rat leg samples instead of human samples limits the direct applicability of the results to human bone behavior. Although rat and human bones have characteristics in common, there are significant differences between them. The biomechanics of motion and the forces applied to the tibia in rats differ greatly from those in humans, making it difficult to extrapolate the findings directly to human tibial behavior.

Finally, regarding the experimental procedures, the bone samples were consistently oriented so that the compressor would only compress the two tibial plateaus. Nevertheless, due to manual placement, some potential errors may occur in the bone's orientation. This could result in the compressor contacting regions other than the intended tibial plateaus, which may also have induced a bias in the results.

5.2 Future works

Broadening the study's scope, additional rat lower limb samples should be tested both experimentally and numerically. All old and young samples could be tested with the inclusion of a layer of growth plate to determine the variability between samples. For the experimental part, young and old bones should be tested to facilitate a more comprehensive comparison between experimental and computational results. In addition, the inclusion of female samples should be conducted to compare the behavioral difference between male and female. Finally, analyzing left legs in the computational study could provide insights into the differences between the two legs within the same sample.

In the experimental part, enhancing the precision of bone placement could be developed to significantly reduce variability in the results obtained and guarantee their reliability.

To get rid of the effects of soft tissues during compression of the entire lower limb, a preconditioning process could be implemented with rapid compression and decompression cycles.

Introducing specific pathologies, such as osteoporosis, into the studied rats could further enrich this work. While comparisons were made between young and old rats, the presence of certain diseases in the older samples was not verified. The introduction of certain pathologies could, therefore, provide valuable insights into the impact of disease on bone mechanics. Additionally, studying the progression of these diseases would allow for the identification of critical stages at which bone mechanics begin to deteriorate significantly.

Next, in the computational part, distinct Young's modulus values could be assigned to the trabecular and cortical bone to obtain results that more accurately reflect reality. In this way, the variability in material properties within the bone can be taken into account. Ideally, the Young's modulus of the tibia should be measured immediately after it has been photographed by micro-CT.

The impact of the material properties of the bone could also be investigated on young bones to determine how these properties differ between young and old bones. By imposing different Young's modulus values on young bones, it would be possible to explore the range of mechanical behaviors exhibited by these bones.

Additionally, incorporating a non-static analysis of the model would be beneficial to include the bone's response over time in the results obtained.

The direction and intensity of the applied force should also be reviewed. Furthermore, to accurately mimic the gait pattern of the species studied, both the intensity and orientation of this force could be varied, with a higher force at the center of the ellipse, which decreases with distance from the center.

A comprehensive computational analysis on the whole leg could be carried out to provide a holistic view of the mechanics of the bone, rather than limiting the study to its upper part.

A comparison could also be conducted between the left and right plateaus, to assess their respective impacts on the mechanics of the bone. Additionally, applying differential forces to the two plateaus, informed by existing data, could be considered to more accurately simulate real-life conditions.

Finally, the use of human samples could be considered to capture the essential mechanics under force applications to its tibial plateaus, similar to the approach taken for rats in this study. Analyzing old, healthy and diseased, and young human bone samples would allow for the assessment of age-related influences on bone mechanics. Thanks to this analysis, factors contributing to bone diseases could be identified, providing insights that could help in combating or preventing the progression of these diseases in the future.

Conclusion

The main objective of the present work was to conduct a comprehensive analysis of the mechanical behavior of rat tibia across two different age groups when subjected to a vertical force applied to both tibial plateaus. Firstly, the influence of the mechanical properties of the bone itself was investigated. Next, an in-depth examination of the relationship between bone's microstructure and its subsequent mechanical behavior with aging was carried out. Subsequently, the introduction of a growth plate between the subchondral and metaphyseal regions enabled the study of its influence on the resulting bone's mechanics, including the effects of variations in its Young's modulus. Lastly, a comparison with experimental results was undertaken to correlate the computational findings with those obtained experimentally.

Firstly, the investigation of the change in Young's modulus in aged bone revealed a significant influence on the bone's mechanical behavior. This difference, although significant in the four regions studied, named as metaphyseal cortical, metaphyseal trabecular, subchondral cortical, and subchondral trabecular areas, was less pronounced in the subchondral region of the bone. The denser composition of this region rendered it less susceptible to alterations induced by Young's modulus variations. This chapter underscores the importance of considering specific sub-regions of the bone, rather than treating the bone as a homogeneous entity, to accurately capture the nuanced mechanical behaviors.

Secondly, the examination of bone microstructure provided insights into the apparent stiffness of the tibial plateaus, effective strain, and the maximum and minimum principal element strain.

The analysis of the tibial plateau's apparent stiffness highlighted that microstructural differences, especially strut presence and trabecular bone architecture, significantly increase deformation in young bones compared to older bones. Additionally, the disparity in apparent stiffness between the two plateaus becomes apparent as the bone ages, with a stiffer lateral plateau. In young bones, the apparent stiffness difference between the lateral and medial plateaus is negligible, while in older bones, this difference is much more pronounced. This variation can be attributed to the alignment and thickness of the bone structure under each plate.

The distribution of effective strain showed a significant impact on the presence or absence of structural struts. In older bones, when struts are widely present, strain concentration in the subchondral region is minimized, as these struts facilitate the transmission of deformation to the metaphyseal region. Conversely, in young bones, the near absence of struts connecting the two bone regions leads to a significant concentration of deformation in the subchondral part, as the deformation cannot be transmitted efficiently to the metaphyseal area. Moreover, high inter-sample variability was observed in young samples, a phenomenon not observed in older samples.

The analysis of maximum and minimum principal element strain further highlighted a more pronounced anisotropy in older bone, particularly in the trabecular bone. This more pronounced anisotropic behavior in older samples can be partially explained by the greater alignment of bone structures in aged bones compared to younger ones.

Thirdly, the study examined the impact of introducing a growth plate and its mechanical properties on bone behavior. The findings revealed that the introduction of the growth plate had a significantly greater impact on young bones compared to old bones. Older bones, which already possess numerous bone struts connecting the subchondral to the metaphyseal part, were only slightly affected by the addition of the growth plate, although it did play a role in the distribution of deformations within the bone. In contrast, young bones, which lack extensive struts, exhibited a clear improvement in the transmission of deformations between the subchondral and metaphyseal regions with the addition of the growth plate. Simulation of a pathological growth plate in young samples, characterized by a Young's modulus of 500 MPa, yielded results closely resembling those obtained in older bones, indicating that such a growth plate combined with microstructure adaptation can induce deformation patterns similar to those found in aged bone, potentially mimicking age-related changes in bone mechanics.

Last but not least, experiments designed to mimic the simulations confirmed that the applied force of 40 N corresponded to the linear elastic phase during bone compression. However, a significant discrepancy was observed between experimental and simulated results concerning the displacement required to achieve a force of 40 N. Such a difference enabled us to establish a range of factors biasing the results obtained in both approaches.

In conclusion, this work has established strong relationships between the mechanical behavior of bone during aging and its underlying microstructure, with a focus on different bone regions and types. This study has provided valuable insights into how age-related alterations affect bone mechanics. This work opens new doors to research opportunities, including dynamic analyses of bone mechanics under forces that mimic gait patterns, investigations into the behavior of the entire leg, and the introduction of certain pathologies to assess their impact on bone mechanics.

Appendix A

Nanoindentation Grids

A.1 Young Bone Grid

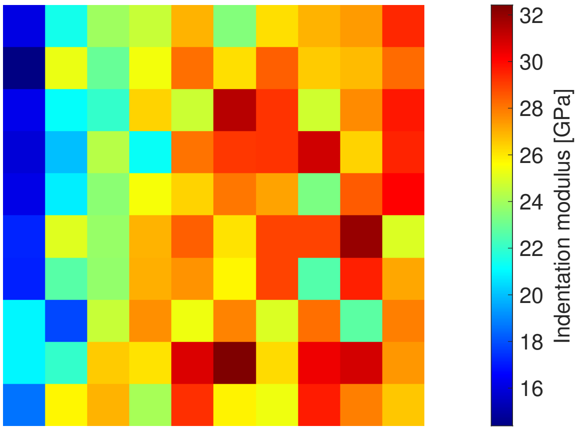

Figure A.1: Nanoindentation grid performed on a 3-month-old rat bone.

A.2 Old Bone Grid

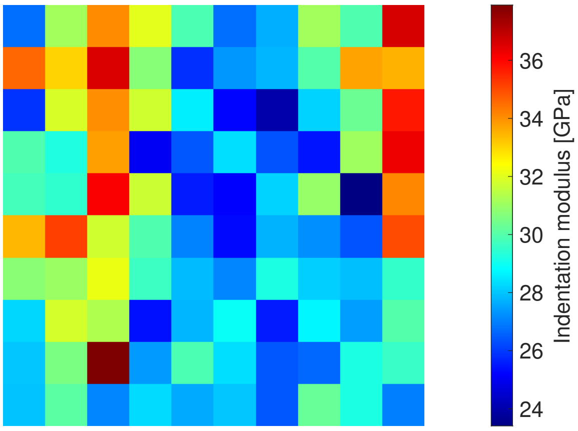

Figure A.2: Nanoindentation grid performed on a 13-month-old rat bone.

Appendix B

Applied displacement

B.1 Without growth plate

	Applied displacement [mm]	
	E = 25.5325 [GPa]	E = 29.5559 [GPa]
1VD	0.001148356	0.001
2VD	0.001370051	0.001183547
4VD	0.001248385	0.001078444
7VD	0.001720616	0.001012512
8VD	0.001431209	0.001241611
11VD	0.001025578	0.000885968
1D	0.031138097	-
2D	0.049575458	-
11D	0.033373381	-
12D	0.020043796	-
14D	0.050197443	-
15D	0.106302657	-

Table B.1: Values of the displacement imposed to ensure a constant 40 N total force. 'D' stands for the right leg and 'V' denotes the old samples.

B.2 With growth plate

		Applied displacement [mm]
1VD	Without growth plate	0.001
	Growth plate (E = 5 [MPa])	0.001153322723
	Growth plate (E = 50 [MPa])	0.00114965654
	Growth plate (E = 500 [MPa])	0.001125552576
11VD	Without growth plate	0.033373381
	Growth plate (E = 5 [MPa])	0.006170554116
	Growth plate (E = 50 [MPa])	0.001928249824
	Growth plate (E = 500 [MPa])	0.00142567362
14VD	Without growth plate	0.050197443
	Growth plate (E = 5 [MPa])	0.02588326647
	Growth plate (E = 50 [MPa])	0.006193005001
	Growth plate (E = 500 [MPa])	0.001887896694

Table B.2: Values of the displacement imposed to ensure a constant 40 N total force, while adding a layer of growth plate. ’D’ stands for the right leg and ’V’ denotes the old samples.

Appendix C

Individual distributions

C.1 Old bones

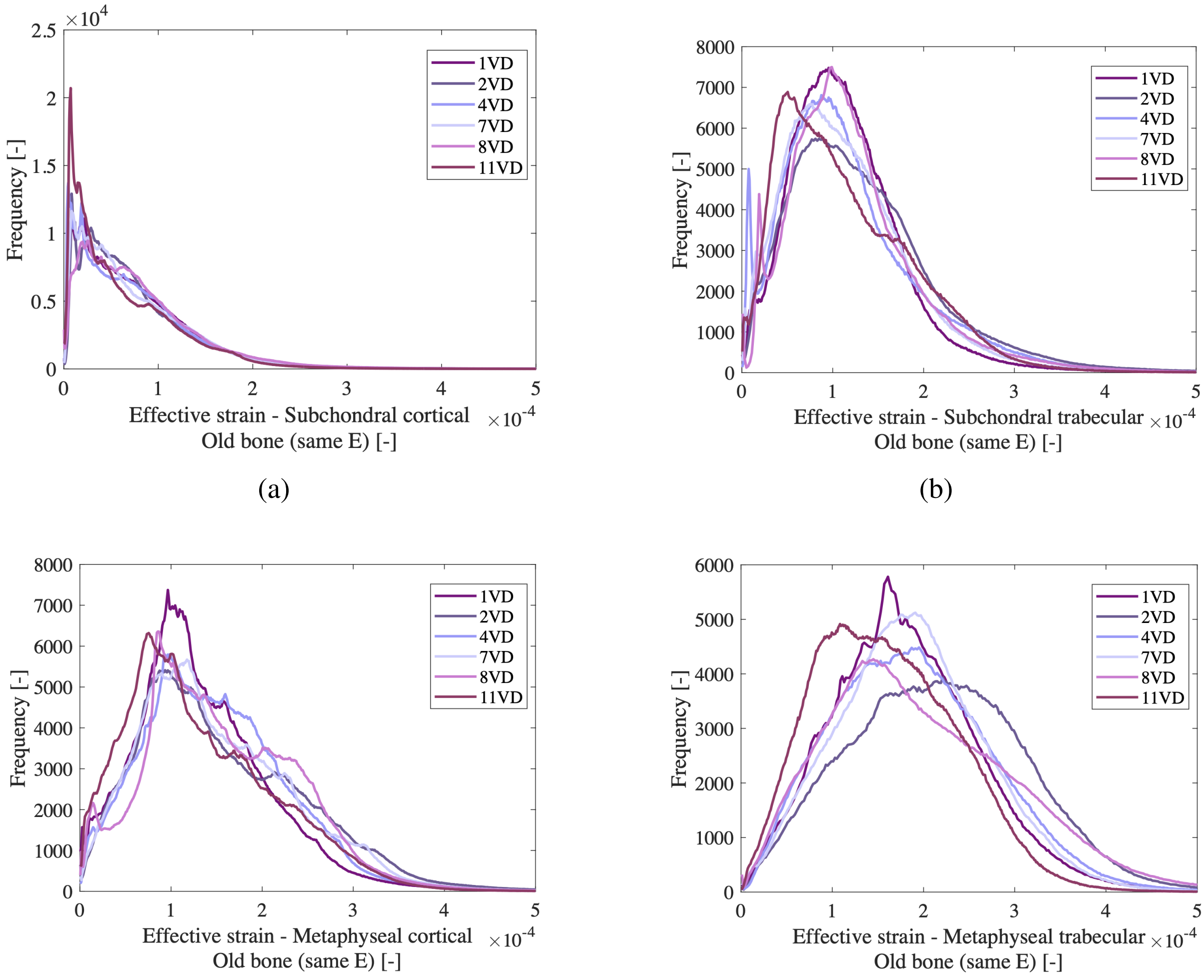

(a) (b)

(c) (d)

Figure C.1: Illustration of the probability density function of the effective strain of the old bone with the same Young's modulus as the young bones, i.e. 25.5325 GPa, in the (a) subchondral cortical area, (b) subchondral trabecular area, (c) metaphyseal cortical area, and (d) metaphyseal trabecular area.

C.2 Old bones - visualization

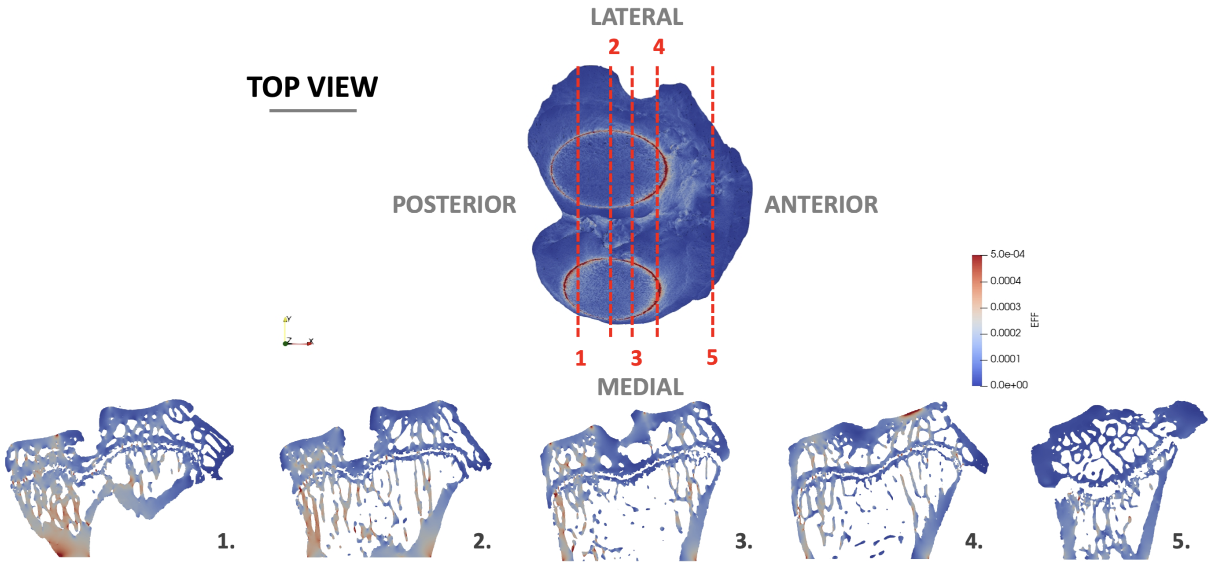

Figure C.2: Illustration of the distribution of the effective strain throughout the entire old bone 7VD with the Young’s modulus of the old bone, i.e. 29.5559 GPa, along with five cross-sectional frontal slices. Each slice is numbered for reference from 1 to 5.

C.3 Young bones

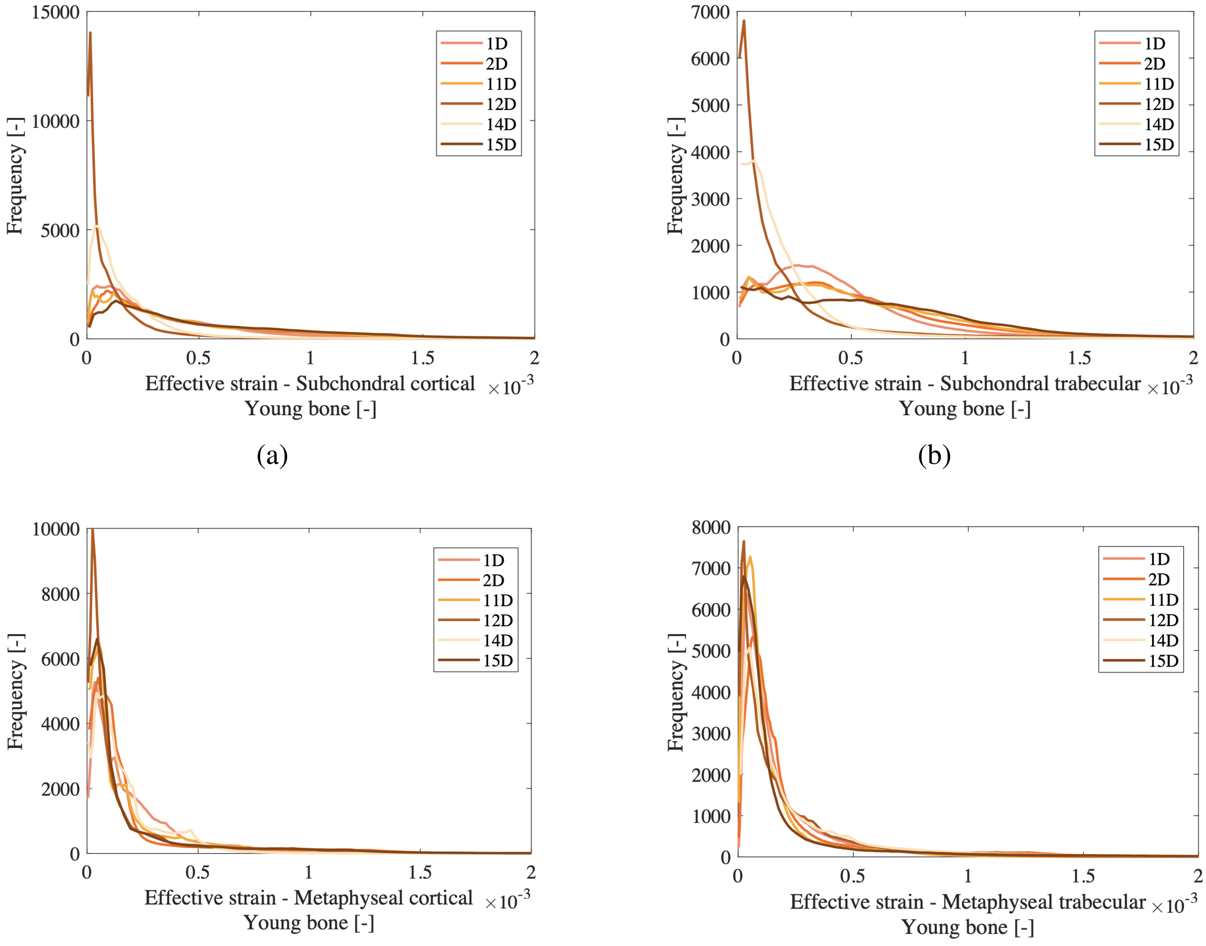

(a) (b) (c) (d)

Figure C.3: Illustration of the probability density function of the effective strain of the young bone, in the (a) subchondral cortical area, (b) subchondral trabecular area, (c) metaphyseal cortical area, and (d) metaphyseal trabecular area.

Appendix D

Struts Analysis

D.1 Old bone - 1VD

D.1.1 Slices illustration

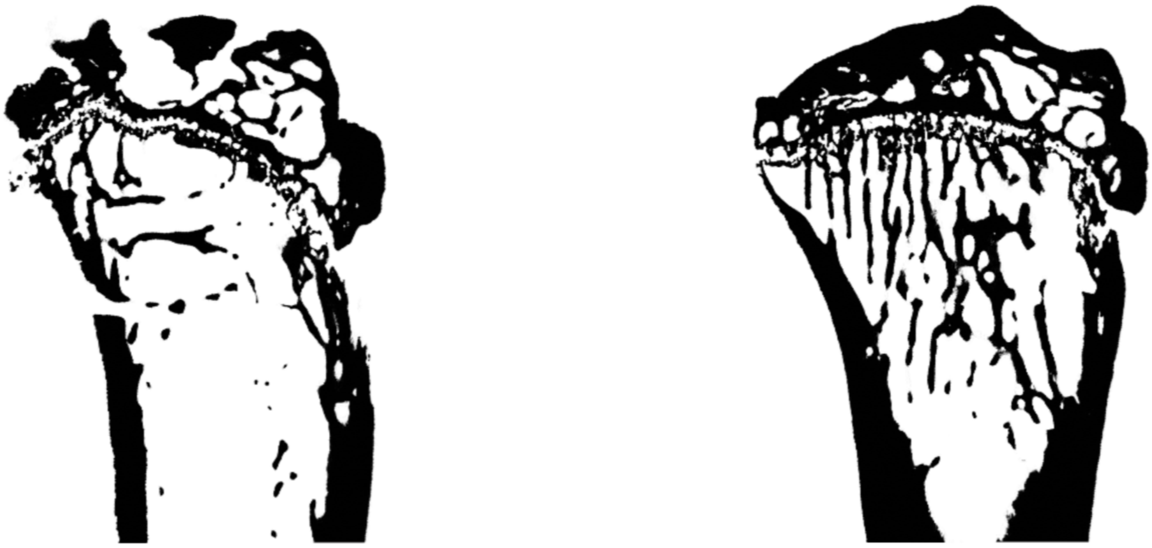

(a) No strut

(b) Struts

Figure D.1: Illustration of the old bone 1VD (a) without strut, meaning with fewer struts than other slices and (b) with struts.

D.1.2 Effective strain distribution of slices

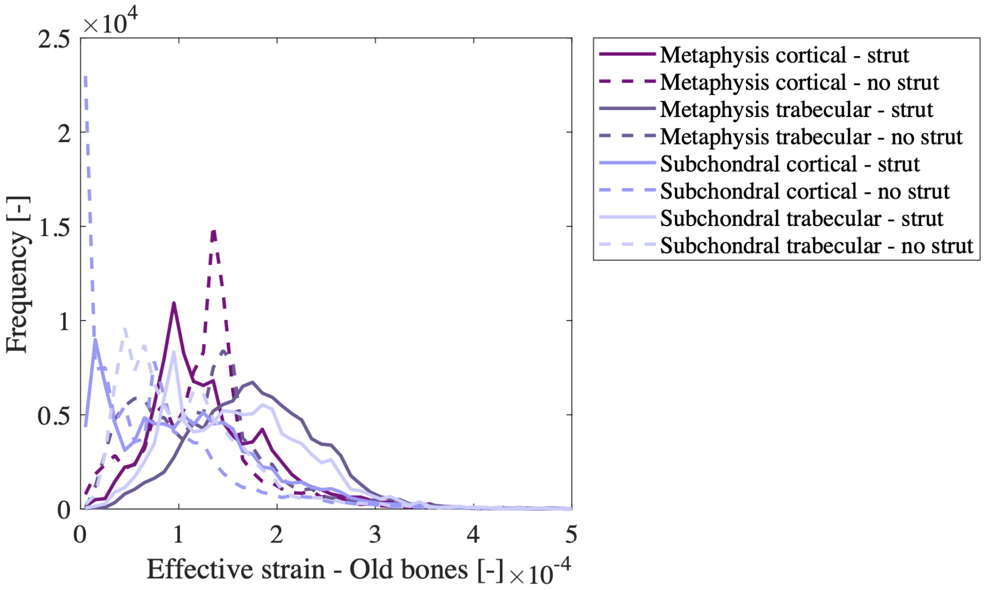

Figure D.2: Illustration of the probability density function of the effective strain for old bone (1VD) in slices with and without strut, in the four different delimited areas.

D.2 Young bone - 11D

D.2.1 Slices illustration

(a) No strut

(b) Struts

Figure D.3: Illustration of the young bone 11D (a) without strut, meaning with fewer struts than other slices and (b) with struts.

D.2.2 Effective strain distribution of slices

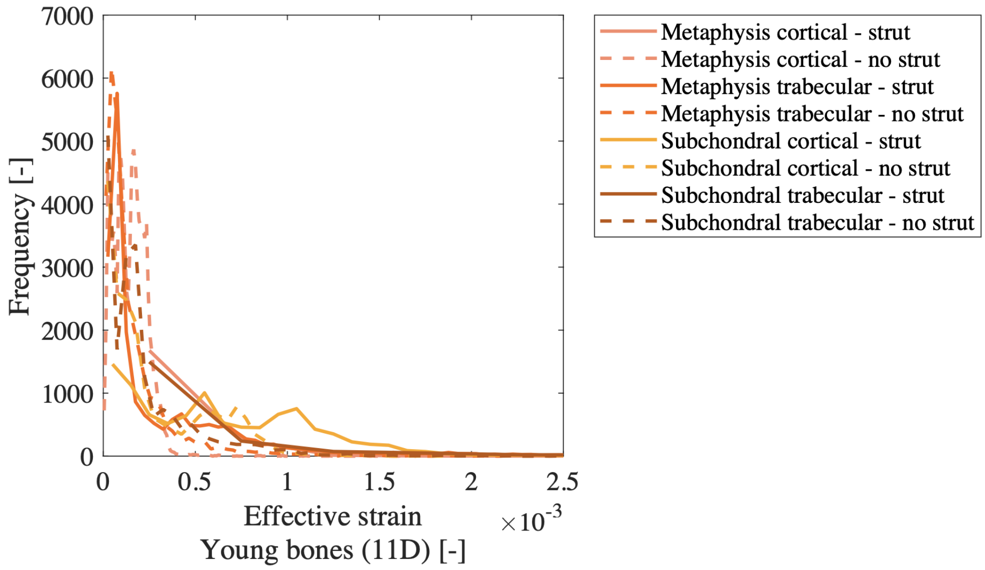

Figure D.4: Illustration of the probability density function of the effective strain for young bone (11D) in slices with and without strut, in the four different delimited areas.

D.3 Young bone - 14D

D.3.1 Slices illustration


(a) No strut

(b) Struts

Figure D.5: Illustration of the young bone 14D (a) without strut, meaning with fewer struts than other slices and (b) with struts.

D.3.2 Effective strain distribution of slices

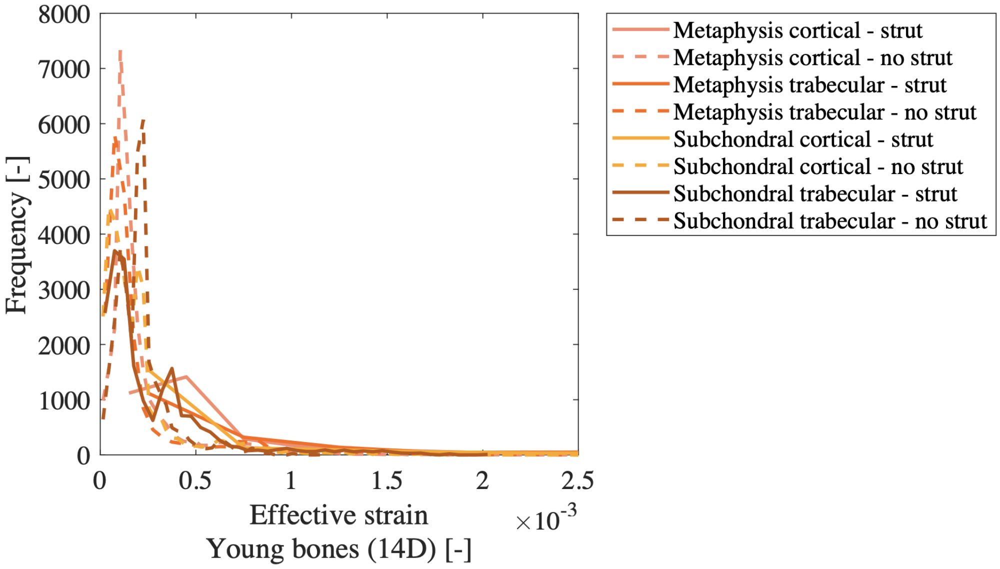

Figure D.6: Illustration of the probability density function of the effective strain for young bone (14D) in slices with and without strut, in the four different delimited areas.

Appendix E

Maximum and minimum element strain distributions

E.1 Old bone - 1VD

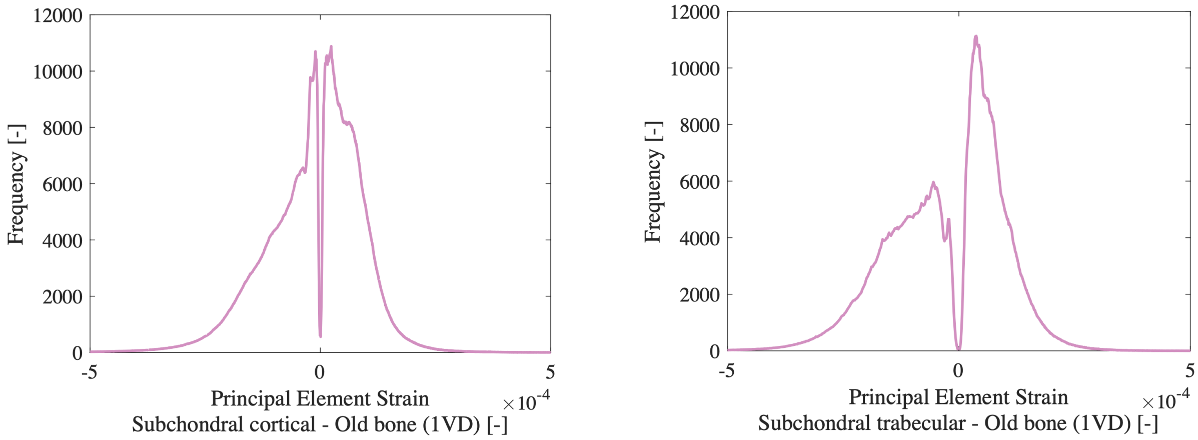

(a) Subchondral cortical

(b) Subchondral trabecular

Figure E.1: Illustration of the distribution of the principal element strain in tension (positive) and compression (negative) in the (a) subchondral cortical region and the (b) subchondral trabecular region for the old bone labeled as 1VD.

E.2 Young bone - 14D

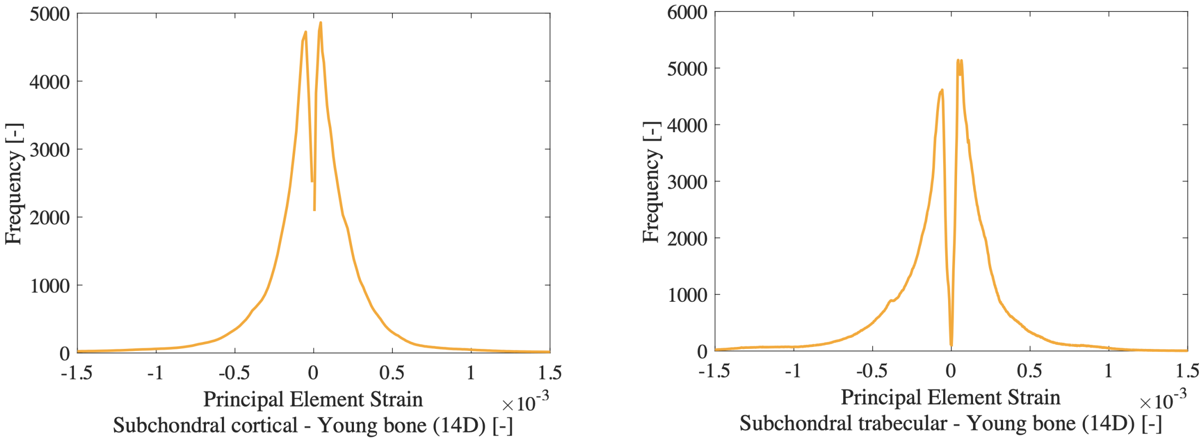

(a) Subchondral cortical

(b) Subchondral trabecular

Figure E.2: Illustration of the distribution of the principal element strain in tension (positive) and compression (negative) in the (a) subchondral cortical region and the (b) subchondral trabecular region for the old bone labeled as 14D.

Bibliography

[1] K. Boros and T. Freemont. Physiology of ageing of the musculoskeletal system. *Best Practice Research Clinical Rheumatology*, 31:203–217, 2017. [CrossRef].

[2] D. D'Lima et Al. Knee joint forces: prediction, measurement, and significance. *Proc Inst Mech Eng H.*, 226(2):95–102, 2012. [CrossRef].

[3] J. Rho et Al. Mechanical properties and the hierarchical structure of bone. *Medical Engineering Physics*, 20:92–102, 1998. [CrossRef].

[4] S. James et Al. Global, regional, and national incidence, prevalence, and years lived with disability for 354 diseases and injuries for 195 countries and territories , 1990-2017: a systematic analysis for the global burden of disease study 2017. *Lancet*, 392:1789–1858, 2018. [CrossRef].

[5] X. Fan et Al. Macro, micro, and molecular. changes of the osteochondral interface in osteoarthritis development. *Frontiers in Cell and Developmental Biology*, 9, 2021. [CrossRef].

[6] S. Coaccioli et Al. Osteoarthritis: New insight on its pathophysiology. *Journal of clinical medicine*, 11(6013), 2022. [CrossRef].

[7] L. Tong et Al. Current understanding of osteoarthritis pathogenesis and relevant new approaches. *Bone Research*, 10(60), 2022. [CrossRef].

[8] B. Clarke. Normal bone anatomy and physiology. *Clin J Am Soc Nephrol.*, 3:131–139, 2008. [CrossRef].

[9] M. Blumer. Bone tissue and histological and molecular events during development of the long bones. *Annals of Anatomy - Anatomischer Anzeiger*, 235, 2021. [CrossRef].

[10] OpenStaxCollege. Bone structure. `https://pressbooks-dev.oer.hawaii.edu/anatomyandphysiology/chapter/bone-structure/` (Last access on 25/02/2024).

[11] Smart Servier Medical Art. Medical images. `https://smart.servier.com` (Last access on 25/02/2024).

[12] M. Bolger. Advancements in composition and structural characterization of bone to inform mechanical outcomes and modeling. *Current Opinion in Biomedical Engineering*, 11:76–84, 2019. [CrossRef].

[13] B. Winkelstein. Orthopaedic biomechanics (1st ed.). *CRC Press.*, pages 71–120, 2013. [CrossRef].

[14] R. Martin. Skeletal tissue mechanics (2nd ed.). *Springer Science*, 2015. [CrossRef].

[15] C. Ethier and C. Simmons. Introductory biomechanics: From cells to organisms. *Cambridge University Press*, pages 379–435, 2007. [CrossRef].

[16] A. Siddiqui. Physiological bone remodeling: Systemic regulation and growth factor involvement. *Physiology (Bethesda)*, 31:233–245, 2016. [CrossRef].

[17] D. Hadjidakis and I. Androulakis. Bone remodeling. *New York Academy of Sciences*, 1092:385–396, 2006. [CrossRef].

[18] D. Buck and G. Dumanian. Bone biology and physiology: Part i. the fundamentals. *Division of Plastic and Reconstructive Surgery*, 129:1314–1320, 2011. [CrossRef].

[19] G. Boivin et Al. Influence of remodeling on the mineralization of bone tissue. *Osteoporos Int.*, 20:1023–1026, 2009. [CrossRef].

[20] S. Ralston. Bone structure and metabolism. *Medicine*, 45:560–564, 2017. [CrossRef].

[21] M. Schorr et Al. Differences in trabecular plate and rod structure in premenopausal women across the weight spectrum. *J Clin Endocrinol Metab*, 104:4501–4510, 2019. [CrossRef].

[22] T. Yamamoto et Al. Alternating lamellar structure in human cellular cementum and rat compact bone: Its structure and formation. *Journal of Oral Biosciences*, 61:105–114, 2019. [CrossRef].

[23] N. Reznikov et Al. Bone hierarchical structure in three dimensions. *Acta Biomaterialia*, 10:3815–3826, 2014. [CrossRef].

[24] M. Georgiadis et Al. Techniques to assess bone ultrastructure organization: orientation and arrangement of mineralized collagen fibrils. *J. R. Soc. Interface*, 13, 2016. [CrossRef].

[25] I. Jäger and P. Fratzl. Mineralized collagen fibrils: A mechanical model with a staggered arrangement of mineral particles. *Biophysical Journal*, 79:1737–1746, 2000. [CrossRef].

[26] V. Ottani et Al. Hierarchical structures in fibrillar collagens. *Micron*, 33:587–596, 2002. [CrossRef].

[27] M. Buehler. Nature designs tough collagen: Explaining the nanostructure of collagen fibrils. *PNAS*, 103:12285–12290, 2006. [CrossRef].

[28] A. Fox et Al. The basic science of articular cartilage: Structure, composition, and function. *Orthopaedics*, 1:461–468, 2009. [CrossRef].

[29] EB. Hunziker et Al. Quantitative structural organization of normal adult human articular cartilage. *Osteoarthritis Cartilage*, 10:564–572, 2002. [CrossRef].

[30] J. Eschweiler et Al. The biomechanics of cartilage-an overview. *Life (Basel)*, 11(4), 2021. [CrossRef].

[31] X. Lu. Biomechanics of articular cartilage and determination of material properties. *Med. Sci. Sports Exerc.*, 40:193–199, 2008. [CrossRef].

[32] T. Lyons et Al. The normal human chondro-osseous junctional region: evidence for contact of uncalcified cartilage with subchondral bone and marrow spaces. *MBMC Musculoskeletal Disorders*, 7:52:1–8, 2006. [CrossRef].

[33] M. Kazemi and J. Williams. Properties of cartilage–subchondral bone junctions: A narrative review with specific focus on the growth plate. *Sage Cartilage*, 2020. [CrossRef].

[34] S. Suri and D. Walsh. Osteochondral alterations in osteoarthritis. *Bone*, 51:204–211, 2012. [CrossRef].

[35] F. Wang et Al. Histomorphometric analysis of adult articular calcified cartilage zone. *Journal of Structural Biology*, 168:3:359–365, 2009. [CrossRef].

[36] RF. Shah et Al. Variation in the thickness of knee cartilage. the use of a novel machine learning algorithm for cartilage segmentation of magnetic resonance images. *J Arthroplasty*, 34:10:2210–2215, 2019. [CrossRef].

[37] E. Giner et Al. Calculation of the critical energy release rate gc of the cement line in cortical bone combining experimental tests and finite element models. *Engineering Fracture Mechanics*, 184:168–182, 2017. [CrossRef].

[38] G. Jacob et Al. Osteochondral injury, management and tissue engineering approaches. *Frontiers in Cell and Developmental Biology*, 8, 2020. [CrossRef].

[39] G. Meachim et Al. Horizontal splitting in patellar articular cartilage. *Arthritis Rheum.*, 21:6:669–674, 1978. [CrossRef].

[40] P. Eggli et Al. Matrix compartments in the growth plate of the proximal tibia of rats. *Anat Rec.*, 211(3):246–257, 1985. [CrossRef].

[41] X. Wang et Al. Enlightenment of growth plate regeneration based on cartilage repair theory: A review. *Frontiers in Bioengineering and Biotechnology*, 9, 2021. [CrossRef].

[42] S. Jang et Al. Recent updates of diagnosis, pathophysiology, and treatment on osteoarthritis of the knee. *Int J Mol Sci.*, 22(2619), 2021. [CrossRef].

[43] P. Kulkarni et Al. Pathophysiological landscape of osteoarthritis. *Adv Clin Chem.*, 100:37–90, 2021. [CrossRef].

[44] S. Grässel and D. Muschter. Recent advances in the treatment of osteoarthritis. *F1000Research*, 9(325), 2020. [CrossRef].

[45] TW. O'Neill et Al. Update on the epidemiology, risk factors and disease outcomes of osteoarthritis. *Best Pract Res Clin Rheumatol.*, 32(2):312–326, 2018. [CrossRef].

[46] MM. Grumbach and RJ Auchus. Estrogen: consequences and implications of human mutations in synthesis and action. *J. Clin. Endocrinol. Metab.*, 84(12):4677–4694, 1999. [CrossRef].

[47] EP. Smith et Al. Estrogen resistance caused by a mutation in the estrogen-receptor gene in a man. *N Engl J Med.*, 331(16):1056–1061, 1994. [CrossRef].

[48] A. Morishima et Al. Aromatase deficiency in male and female siblings caused by a novel mutation and the physiological role of estrogens. *J Clin Endocrinol Metab.*, 80(12):3689–3698, 1995. [CrossRef].

[49] F. De Luca. Impaired growth plate chondrogenesis in children with chronic illnesses. *International Pediatric Research Foundation, Inc.*, 59(5):625–629, 2006. [CrossRef].

[50] K. Naaktgeboren et Al. Growth plate injuries in children in sports: A review of sever's disease. *Strength and Conditioning Journal*, 39(2):59–68, 2017. [CrossRef].

[51] K. Cassas and A. Cassettari-Wayhs. Childhood and adolescent sports-related overuse injuries. *American Family Physician*, 73(6):1014–1022, 2006. [CrossRef].

[52] A. Frisch et Al. Injuries, risk factors and prevention initiatives in youth sport. *Br Med Bull.*, 92:95–121, 2009. [CrossRef].

[53] J. Johnson. Overuse injuries in young athletes: Cause and prevention. *Strength and Conditioning Journal*, 30(2):27–31, 2008. [CrossRef].

[54] RW. Scharfbillig et Al. Sever's disease: what does the literature really tell us? *J Am Podiatr Med Assoc.*, 98(3):212–23, 2008. [CrossRef].

[55] K. Staines et Al. a computed microtomography method for understanding epiphyseal growth plate fusion. *Frontiers in Materials*, 4(48):1–8, 2018. [CrossRef].

[56] A. Domínguez-Oliva et Al. The importance of animal models in biomedical research: Current insights and applications. *Animals*, 13(1223), 2023. [CrossRef].

[57] N. Robinson et Al. The current state of animal models in research: A review. *International Journal of Surgery*, 72:9–13, 2019. [CrossRef].

[58] P. Mukherjee et Al. Role of animal models in biomedical research: a review. *Laboratory Animal Research*, 38(18), 2022. [CrossRef].

[59] AM. McCoy. Animal models of osteoarthritis: Comparisons and key considerations. *Veterinary Pathology*, 52(5):803–818, 2015. [CrossRef].

[60] C. Szpirer. Rat models of human diseases and related phenotypes: a systematic inventory of the causative genes. *Journal of Biomedical Science*, 27(84), 2020. [CrossRef].

[61] J. Maroquin. Relationship between microstructure and mechanical properties of proximal tibia in rats during ageing. *Master Thesis*, 2022-2023. [CrossRef].

[62] L. Mary et Al. Guidelines for assessment of bone microstructure in rodents using micro-computed tomography. *Journal of bone and mineral research*, 25(7):1468–1486, 2010. [CrossRef].

[63] X. Yang et Al. An improved median-based otsu image thresholding algorithm. *AASRI Procedia*, 3:468–473, 2012. [CrossRef].

[64] Materialise. Mimics student edition course book. *Mimics SE*. [CrossRef].

[65] H. Wang et Al. Efficacy of chinese herbal formulation combined with bone mesenchymal stem cells in repairing rat cartilage tissues. *Research Square*, 2020. [CrossRef].

[66] D. Shepherd and B. Seedhom. A technique for measuring the compressive modulus of articular cartilage under physiological loading rates with preliminary results. *Proc Instn Mech Engrs.*, 211:155–165, 1997. [CrossRef].

[67] W. Kabir et Al. Assessment of native human articular cartilage: A biomechanical protocol. *Cartilage*, 13(2):427–437, 2020. [CrossRef].

[68] D. Shepherd and B. Seedhom. The 'instantaneous' compressive modulus of human articular cartilage in joints of the lower limb. *British Society for Rheumatology*, 38:124–132, 1999. [CrossRef].

[69] D. Shepherd and B. Seedhom. The relationship of the compressive modulus of articular cartilage with its deformation response to cyclic loading: does cartilage optimize its modulus so as to minimize the strains arising in it due to the prevalent loading regime? *Rheumatology*, 40:274–284, 2001. [CrossRef].

[70] S. Park et Al. Mechanical response of bovine articular cartilage under dynamic unconfined compression loading at physiological stress levels. *OsteoArthritis and Cartilage*, 12:2004, 65–73. [CrossRef].

[71] T. Keaveny et Al. Biomechanics of trabecular bone. *Annu. Rev. Biomed. Eng.*, 3:307–333, 2001. [CrossRef].

[72] A. Ladd and J. Kinney. Numerical errors and uncertainties in finite-element modeling of trabecular bone. *Journal of Biomechanics*, 31:941—945, 1998. [CrossRef].

[73] B. Roberts et Al. Joint loading and proximal tibia subchondral trabecular bone microarchitecture differ with walking gait patterns in end-stage knee osteoarthritis. *Osteoarthritis and Cartilage.*, 25, 2017. [CrossRef].

[74] J. Gao et Al. Strain distribution evaluation of rat tibia under axial compressive load by combining strain gauge measurement and finite element analysis. *Applied Bionics and Biomechanics*, 2019. [CrossRef].

[75] CC. Lin et Al. Reconstruction of three-dimensional tibiofemoral kinematics using single-plane fluoroscopy and a personalized kinematic model. *Applied Sciences*, 11(9415), 2021. [CrossRef].

[76] JY. Wang et Al. The effects of different repair methods for a posterior root tear of the lateral meniscus on the biomechanics of the knee: a finite element analysis. *Journal of Orthopaedic Surgery and Research*, 16(296), 2021. [CrossRef].

[77] M. Sohail et Al. Modified whiteside's line-based transepicondylar axis for imageless total knee arthroplasty. *Mathematics*, 10(3670), 2022. [CrossRef].

[78] S. Bersini et Al. A dynamic multibody model of the physiological knee to predict internal loads during movement in gravitational field. *Computer Methods in Biomechanics and Biomedical Engineering*, 19(5):571–579, 2016. [CrossRef].

[79] S. Huzni et Al. The use of frictional and bonded contact models in finite element analysis for internal fixation of tibia fracture. *Frattura ed Integrità Strutturale*, 61:130–139, 2022. [CrossRef].

[80] S. Oliviero et Al. Non-invasive prediction of the mouse tibia mechanical properties from microct images: comparison between different finite element models. *Biomechanics and Modeling in Mechanobiology*, 20:941–955, 2021. [CrossRef].

[81] Z. Liu et Al. The adaptive response of rat tibia to different levels of peak strain and durations of experiment. *Medical Engineering and Physics*, 102(103785), 2022. [CrossRef].

[82] Z-C. Li et Al. Small-animal pet/ct assessment of bone microdamage in ovariectomized rats. *Journal of Nuclear Medicine*, 52(5):769–775, 2011. [CrossRef].

[83] D. Ruffoni and GH. van Lenthe. Finite element analysis in bone research: A computational method relating structure to mechanical function. *Comprehensive Biomaterials II*, 3:169–196, 2017. [CrossRef].

[84] C. Flaig and P. Arbenz. A scalable memory efficient multigrid solver for micro-finite element analyses based on ct images. *Parallel Computing*, 37:846–854, 2011. [CrossRef].

[85] P. Arbenz et Al. Bone structure analysis on multiple gpgpus. *J. Parallel Distrib. Comput.*, 74:2941–2950, 2014. [CrossRef].

[86] N. Knowlesa et Al. High performance multi-platform computing for large-scale image-based finite element modeling of bone. *Computer Methods and Programs in Biomedicine*, 225(107051), 2022. [CrossRef].

[87] E. Zurich. Thesis: A highly scalable memory efficient multigrid solver for -finite element analyses. 2012. [CrossRef].

[88] W. Pistoia et Al. Estimation of distal radius failure load with micro-finite element analysis models based on three-dimensional peripheral quantitative computed tomography images. *Bone*, 30(6):842–848, 2002. [CrossRef].

[89] W. Lai et Al. Chapter 3 - kinematics of a continuum. *Introduction to Continuum Mechanics (Fourth Edition) Butterworth-Heinemann*, pages 69–153, 2010. [CrossRef].

[90] M. Sadd et Al. Chapter 2 - deformation: Displacements and strains. *Elasticity (Fourth Edition)*, Academic Press:31–55, 2021. [CrossRef].

[91] B. Yang. 15 - static analysis of linearly elastic bodies. *Stress, Strain, and Structural Dynamics*, Academic Press:739–805, 2005. [CrossRef].

[92] D. Hauser et Al. Anatomic variation of structural properties of periacetabular bone as a function of age. *The Journal of Arthroplasty*, 12(7):804–811, 1997. [CrossRef].

[93] C. Collins. Rat skeletal system. `https://quizlet.com/244308157/rat-skeletal-system-diagram/` Last access on 17th june 2024.

[94] P. Mishra et Al. Application of student's t-test, analysis of variance, and covariance. *Annals of Cardiac Anaesthesia*, 22(4), 2019. [CrossRef].

[95] M. Ferrara et Al. Biomechanical properties of retina and choroid: a comprehensive review of techniques and translational relevance. *Springer Nature*, 2021. [CrossRef].

[96] G. Bertocci et Al. Femur fracture biomechanics and morphology associated withtorsional and bending loading conditions in an in vitro immatureporcine model. *Journal of Forensic and Legal Medicine*, 52:5–11, 2017. [CrossRef].

[97] DM. Patton et Al. The relationship between whole bone stiffness and strength is age and sex dependent. *J Biomech.*, 23(83):125–133, 2019. [CrossRef].

[98] L. Müller et Al. Changes in subchondral bone microstructure and shape with age in tibial knee. *Musculoskeletal/joint biomechanics III: Bone and tendon*, ESB, 2023. [CrossRef].

[99] H. Leng et Al. Effect of age on mechanical properties of the collagen phase in different orientations of human cortical bone. *Bone*, 55(2):288–91, 2013. [CrossRef].

[100] G. Voulgaridou et Al. Vitamin d and calcium in osteoporosis, and the role of bone turnover markers: A narrative review of recent data from rcts. *Diseases*, 11(1):2023. [CrossRef].

[101] J. Immonen et Al. Osteoarthritis of the anterior cruciate ligament and medial tibial plateau: A cadaveric study. *Cartilage*, 10(1):11–18, 2019. [CrossRef].

[102] K. Vincent et Al. The pathophysiology of osteoarthritis: a mechanical perspective on the knee joint. *PM R.*, 4(5):S3–9, 2012. [CrossRef].

[103] MB. Schaffler et Al. Stiffness of compact bone: effects of porosity and density. *J Biomech.*, 21(1):13–16, 1988. [CrossRef].

[104] H. Bayraktar et Al. Comparison of the elastic and yield properties of human femoral trabecular and cortical bone tissue. *J Biomech.*, 37(1):27–35, 2004. [CrossRef].

[105] E. Morgan et Al. Bone mechanical properties in healthy and diseased states. *Annu Rev Biomed Eng.*, 20:119–143, 2018. [CrossRef].

[106] D. George et Al. Prediction of cortical bone thickness variations in the tibial diaphysis of running rats. *Life (Basel)*, 12(2), 2022. [CrossRef].

[107] T. Mustafy et Al. Experimental and finite element analyses of bone strains in the growing rat t tibia induced by in vivo axial compression. *Journal of the Mechanical Behavior of Biomedical Materials*, 94:176–185, 2019. [CrossRef].

[108] Mustafy et Al. Isolated cyclic loading during adolescence improves tibial bone microstructure and strength at adulthood. *JBMR Plus (WOA)*, 4(4):1–16, 2020. [CrossRef].

[109] S. McBride and M. Silva. Adaptive and injury response of bone to mechanical loading. *Bonekey Osteovision*, 10:1:8, 2012. [CrossRef].

[110] M. Forwood and C. Turner. Skeletal adaptations to mechanical usage: results from tibial loading studies in rats. *Bone*, 17(4):S197–S205, 1995. [CrossRef].

[111] D. Raab-Cullen et Al. Bone response to alternate-day mechanical loading of the rat tibia. *Journal of Bone and Mineral Research*, 9(2):203–211, 1994. [CrossRef].

[112] A. Ural and D. Vashishth. Anisotropy of age-related toughness loss in human cortical bone: A finite element study. *Journal of Biomechanics*, 40(7):1606–1614, 2007. [CrossRef].

[113] N. Hart et Al. Mechanical basis of bone strength: influence of bone material, bone structure and muscle action. *J Musculoskelet Neuronal Interact.*, 17(3):114–139, 2017. [CrossRef].

[114] S. Li et Al. Variability and anisotropy of mechanical behavior of cortical bone in tension and compression. *Journal of the Mechanical Behavior of Biomedical Materials*, 21:109–120, 2013. [CrossRef].

[115] S. Kilborn et Al. Review of growth plate closure compared with age at sexual maturity and lifespan in laboratory animals. *Contemp Top Lab Anim Sci.*, 41(5):21–26, 2002. [CrossRef].

[116] H. Roach et Al. Temporal analysis of rat growth plates: Cessation of growth with age despite presence of a physis. *Journal of Histochemistry Cytochemistry*, 51(3):373–383, 2003. [CrossRef].

[117] S. Bailey and D. Vashishth. Mechanical characterization of bone: State of the art in experimental approaches—what types of experiments do people do and how does one interpret the results? *Curr Osteoporos Rep.*, 16:423–433, 2018. [CrossRef].

[118] R. Oftadeh et Al. Hierarchical analysis and multi-scale modelling of rat cortical and trabecular bone. *Journal of the Royal Society Interface*, 2015. [CrossRef].

[119] C. Liu et Al. Effects of mechanical loading on cortical defect repair using a novel mechanobiological model of bone healing. *Bone*, 108:145–155, 2018. [CrossRef].

[120] U. Hansen et Al. The effect of strain rate on the mechanical properties of human cortical bone. *J Biomech Eng.*, 130(1), 2008. [CrossRef].

[121] J. Currey et Al. The effects of strain rate, reconstruction and mineral content on some mechanical properties of bovine bone. *Journal of Biomechanics*, 8(1):81–86, 1975. [CrossRef].